19951218 009

DISCLAIMER NOTICE

UNCLASSIFIED

Technical Report
distributed by

DEFENSE
TECHNICAL
INFORMATION
CENTER

DTIC Acquiring Information-
Imparting Knowledge

Cameron Station
Alexandria, Virginia 22304-6145
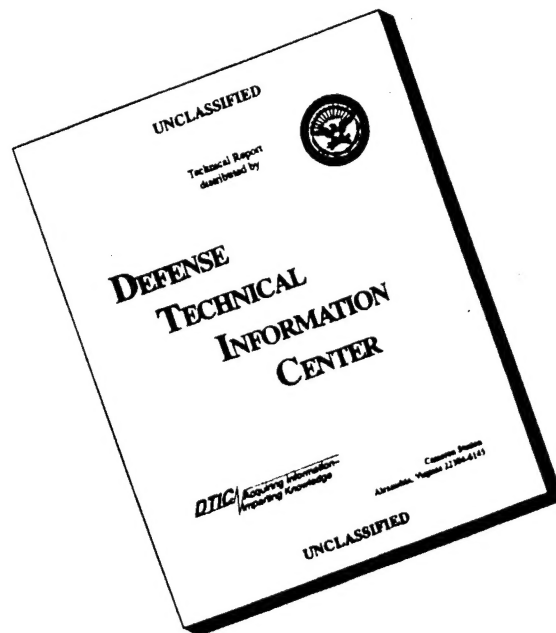
UNCLASSIFIED

THIS DOCUMENT IS BEST QUALITY AVAILABLE. THE COPY FURNISHED TO DTIC CONTAINED A SIGNIFICANT NUMBER OF PAGES WHICH DO NOT REPRODUCE LEGIBLY.

1. Report No.	2. Government Accession No.	3. Recipient's Catalog No.
NASA CR-159571		

4. Title and Subtitle	5. Report Date
Diffusion Bonded Boron/Aluminum Spar-Shell Fan Blade	June 1980
	6. Performing Organization Code

7. Author(s) Work Performed By: C. E. K. Carlson, J. L. Cutler and W. J. Fisher Report Prepared By: J. V. W. Memmott	8. Performing Organization Report No.
	HSER 7698
	10. Work Unit No.

9. Performing Organization Name and Address	11. Contract or Grant No.
United Technologies Corporation Hamilton Standard Division Windsor Locks, Connecticut 06095	NAS 3-20407
	13. Type of Report and Period Covered

12. Sponsoring Agency Name and Address	Final Report 6/77-5/78
NASA-Lewis Research Center 21000 Brookpark Road Cleveland, Ohio 44135	14. Sponsoring Agency Code

15. Supplementary Notes

NASA Project Manager, David L. McDanels, Metal Matrix Composites Section, Materials and Structures Division, NASA-Lewis Research Center, Cleveland, Ohio

16. Abstract

The Diffusion Bonded Boron/Aluminum Spar-Shell Fan Blade Program consisted of a design and a process development tasks intended to demonstrate composite blade application in large high-bypass ratio turbofan engines. The design task included selection of a representative airfoil model; a preliminary design effort, which included parametric studies of component materials and geometries, leading to the selection of two candidate designs, subject to NASA Project Manager approval, for detail designing; and a detail design effort on two designs which would lead to pertinent structural property definition and a detailed blade specification drawing. The process development task consisted of a process optimization effort leading to specification with the NASA Project Manager's approval of process parameters to be used in the follow-on effort of fabricating two simulated airfoils, non-destructive evaluation (NDE) measurements including primary frequency testing of same and delivery of subject airfoil pressings to NASA-Lewis.

17. Key Words (Suggested by Author(s))		18. Distribution Statement
NDE		
Boron	Rotor Stage Weight	Unclassified
Aluminum	Diffusion Bonded	Unlimited
Composite Materials	Honeycomb	Star Category
Fan Blades	High-Bypass Ratio	
Metal Matrix Composite	Turbofan	

19. Security Classif. (of this report)	20. Security Classif. (of this page)	21. No. of Pages	22. Price*
Unclassified	Unclassified	107	

DTIC QUALITY INSPECTED 1

TABLE OF CONTENTS

TABLE OF CONTENTS (Continued)

LIST OF ILLUSTRATIONS

LIST OF ILLUSTRATIONS (Continued)

LIST OF ILLUSTRATIONS (Continued)

LIST OF TABLES

FORWARD

This final report prepared by Mr. J. V. W. Memmott of the Advanced Composites Application Group of the Hamilton Standard Division of the United Technologies Corporation covers the program conducted by Hamilton Standard under NASA Lewis Contract NAS3-20407. The program period was June 10, 1977 to May 31, 1978. The project manager for NASA Lewis Research Center was Mr. D. McDanels. Project manager for Hamilton Standard was Mr. W. J. Fisher. Design was under the direction of Mr. C. E. K. Carlson. Fabrication was under the direction of Mr. J. L. Cutler. Materials and Process Engineering support was under the direction of Mr. E. Delgrosso. All Analysis & Measurements were made in English units and are converted to SI units for publication purposes.

1.0 SUMMARY

The objective of this program was to apply the spar and shell blade design concept to a first stage fan blade in a high bypass ratio advanced turbofan engine application and to perform process development efforts on key manufacturing considerations so as to demonstrate the readiness of the application of both the design system and the process system to a future blade requirement. The design incorporates all current FOD resistant approaches which are considered necessary in order to produce a successful product. The scope of the work in this report includes two basic tasks: Task I -- Design and Task II -- Process Development.

Task I -- The preliminary blade design effort selected an existing 3.0 aspect ratio spar and shell blade envelope, for the Pratt & Whitney JT9D engine, upon which to perform the design study. The study produced four candidate blade configurations; one which featured a hollow titanium spar resulted in a 39% rotor stage weight savings. Although of greatest technological interest, the judgment was made to detail design a lightweight/solid titanium spar blade which produced a 14% rotor stage weight savings. This judgment was based on the current technological shortfall of superplastic forming of titanium into satisfactory hollow flat tubular shapes and the long term effort required along with an inherent risk in achieving this feature. The selected blade with a choice of composite matrix material satisfactorily met the design criterias of static stress, FOD resistance and dynamic response thus demonstrating the design system and design concept readiness for a future blade requirement.

Task II -- The process development effort selected key manufacturing considerations based on the selected blade design to validate a confidence in the produceability of a successful product. The efforts expended on the material test elements were composite material evaluation, metal joining process development and titanium honeycomb material property evaluation. These results were then applied to two demonstration airfoil pressings, one of each composite matrix material, to demonstrate the design concept. This effort resulted in a measured success of the design concept with the selection of honeycomb compressive strength requirement still to be determined.

2.0 INTRODUCTION

The application of advanced composite materials for the construction of large high performance fan blades offers potentially attractive weight and cost benefits. The major inhibitor to the utilization of composite blades is the relatively low resistance of composite materials to foreign object damage (FOD). United Technologies first experienced this problem in 1969 in testing JT9D solid graphite/epoxy composite fan blade and the JT9D boron/epoxy spar-shell fan blade. Since then there have been many attempts to improve the FOD resistance of composite fan blades by modifying the composite materials and design concepts. Approaches have included use of different fibers, matrices, airfoil layups and root designs.

The most successful demonstration of satisfactory FOD resistance of a composite fan blade has been the spar/shell blade developed by Hamilton Standard in 1975 under contract NAS3-17837 (See Ref. 1). The QCSEE type blade design consisted of 5.7 mil BORSIC/6061 aluminum composite airfoils adhesively bonded to a titanium spar which incorporated a rocking retention. The program demonstrated the ability of the blades to sustain impacts of birds up to 1.36Kg (3 lbs.) in size with little damage. At a 22° blade section angle with the plane of rotation, the maximum weight loss was 1.4%; at 32°, the maximum weight loss was 4.7%. In all cases, unbonding did not exceed 1.1%. All blades in the post-test condition were judged capable of post impact engine shutdown and windmill operation in accordance with the FAA guidelines for large bird impacts. Recent materials characterization programs have indicated that further improvements might be realized by using larger diameter boron filaments, varying the aluminum matrix, and quick-vac metal bonding the protective leading edge sheath to the blade shell which leads to also metal bonding the shell to the spar.

The program was accomplished by dividing the work into two tasks and applying the necessary resources to each:

Task I -- Preliminary & Detail Blade Design Task which conducted preliminary weight and stress analysis of various configurations, selected a best candidate configuration and performed additional blade structural analysis so as to provide assurance that the design met basic aerostructural requirements for a flightworthy product.

Task II -- Process Development Task which selected key features from the selected blade design to perform process evaluation culminating in two simulated airfoil pressings representative of the selected design concept performed so as to demonstrate the manufacturability of the design.

3.0 DISCUSSION

3.1 TASK I - BLADE DESIGN

3.1.1 Recommended Engine Fan Configuration

The basis for this program and the ensuing preliminary design studies conducted was to examine the potential role of composite fan blades in meeting the requirements of advanced high by-pass ratio subsonic turbofan jet engines. Selected for a design model was the Pratt & Whitney JT9D engine which features a single stage fan rotor with a bypass ratio of 5:1. An existing preliminary design fan blade featuring a 3.0 aspect ratio was selected for design evaluation with the airfoil's external envelope maintained and the internal geometry and material selected so as to meet structural requirements. The selected 3.0 aspect ratio allows for compatibility with the existing fan nacelle and fan exit guide vane envelopes. Still lower aspect ratio, wider chord blade designs may permit more advantageous combinations of impact resistance, aeromechanical stability and lower fan stage weight. However, such wide chord blade designs were excluded from this present study in order to maintain compatibility with existing tooling and test hardware.

In order to demonstrate a technical basis upon which a composite fan blade design would offer a significant improvement over existing "state-of-the-art" titanium fan blades, it is necessary to meet equivalent uninstalled engine performance requirements while offering a distinct technological advantage. The potential of substantial weight savings which translates to increased aircraft payload and fuel efficiency is deemed the principal technological advantage composite fan blades offer in this application. Thus the design studies conducted sought to meet critical structural requirements and provide installed (flight) performance improvements based on lower engine weight.

3.1.2 Preliminary Blade Configuration Study

While focusing on the ultimate design goal of significant rotor stage weight reduction and satisfactorily meeting all rotor structural requirements, a parametric design study was pursued in order to optimize critical design features. The focus of the study was examination of such spar and shell blade construction variables as spar material, position and geometry; shell matrix material, fiber orientation and geometry; sheath material and geometry; and shell cavity fill material, wall thickness and density. Table I details the range of material and geometric properties examined in this study, each of which was examined as to its effect on torsional frequency response. The study's output presented in Table II established the material and geometric constraints upon which the preliminary blade design was to be based. Table III presents the basic structural and geometric properties of this blade, configuration 1, and compares it with the 46 bladed bill of material JT9D titanium rotor system. This initial spar and shell design consisting of thirty 3.0 aspect ratio

blades met the structural requirements of centrifugal disk loading, airfoil static stress and growth and untwist limits, and blade uncoupled natural frequency requirements over the engine operating range. In addition, an analytical examination of FOD impact stresses indicated an adequate spar stress margin. However, the principal design goal of rotor stage weight savings was not achieved with any shell fill candidate materials and naturally with either shell matrix alloy. The calculated total rotor weight of 393 Kg (866 lbs.) for the upper extreme of the projected individual blade weight range of 5.99 - 7.04 Kg (13.2 - 15.5 lbs) was 16% greater than the bill of material titanium blade rotor system weight of 399 Kg (747 lbs). Initially, it was judged that weight reductions to meet equivalency or better when compared with the bill of material stage weight could be accomplished in the detailed design phase. Subsequently to that, a rigorous re-examination of the preliminary design was deemed necessary to meet the principal design goal of substantive weight superiority. This iteration led to three refined candidate configurations (2A, 3 and 4) all of which meet the preliminary design structural goals and all achieved the stage weight savings when compared to the bill of material design. Table IV defines the modifications of blade configuration 1 which produced the substantial rotor system weight improvement and summarizes the rotor system weights for these three configurations in comparison with the baseline titanium rotor system. As is readily apparent the hollow titanium spar blade, configuration 3, produced the largest blade and rotor stage weight savings of 39%, 132 Kg (291 lbs), when compared with the bill of material rotor system. The modified solid titanium spar blade which featured substantial spar chordwise resizing (to be described in Section 3.1.3) reduced the rotor system weight 14%, 46 Kg (101 lbs). Although not as attractive as the hollow spar blade, its available technology was deemed the prudent selection over a conceptual design, which lacked demonstrated manufacturability, for the succeeding detailed design phase. Also effecting this selection was the prospect of a modest follow-on program which would take the detailed design through a manufacturing demonstration phase whose scope did not permit the effort related to superplasticity forming of hollow titanium spars. The hollow steel spar manufacturing technology had been previously shown in the Hamilton Standard's boron epoxy JT9D blade program which when combined with on-going industry efforts in development of superplasticity titanium formings makes hollow spars a viable future technological feature. The hollow AISI 4340 steel spar blades (Configuration 4) offered similar stage weight savings of 18%, 60 Kg (132 lbs) to the modified solid titanium spar blades and thus was considered a higher risk choice to achieve approximately the same weight savings. The Figure 1 Campbell diagram shows the resonant frequency response of three candidate designs, (configuration 2A to be discussed in Section 3.1.3.4). The requirement to have adequate margin of clearance with low order engine rotor frequency excitation within the engine operating range, (i.e., 1E and 2E/1st bending, 2E and 3E/2nd bending, and 3E and 4E/1st torsion) was achieved except for 2E/1st bending. This excitation source and frequency mode normally cannot be eliminated from the operating range for shroudless fan blades and thus is tuned outside of frequently encountered constant

6

rotating speed conditions. A frequency correction factor would normally be applied after design refinement which would drop the bending mode frequencies and raise the torsion mode frequencies all by approximately 15%.

The two variants selected to be pursued in the detail design phase thus consisted of configuration 2A with two alternate shell matrix materials, namely, AA1100 and AA6061 aluminum alloys. This variant is considered important owing to a tradeoff of impact resistance with transverse tensile properties between the alloys leading to potentially different FOD tolerance and static stress safety margins.

Table I. Spar And Shell Blade Component Parametric Design Study

Variables	Material	Range Of Material And Geometric Properties	
		SI Units	English Units
1. Spar			
a. Material	6-4 Titanium & Steel	Et 110 – 200 GPa	16 – 29 x 10^6 psi
b. Geometry	Solid & Hollow Titanium & Hollow Steel		
c. Position	₵ 34-54% of Blade Chord		
2. Shell			
a. Composite Matrix	AA6061 & AA1100		
b. Fiber Orientation	± 20° – ± 45°		
c. Wall Thickness		± 1.91 – 2.29 mm	0.059 – 0.075 inch
d. Cavity Fill Material	Titanium Honeycomb & Cast Aluminum	ρ1.63 – 2.77 gm/cc	0.059 – 0.100 lb/in^3
3. Sheath			
a. Material	6 – 4 Titanium & Inconel 625	Et 110–200GPa	16 – 29 x 10^6
b. Width	15 – 25% of chord		

Table II.   Recommended Blade Component Properties Based On Parametric Study

Variable	Selected Material Or Geometric Property
1. Spar	6AL-4V Titanium
a. Material	6AL-4V Titanium
b. Geometry	Solid
c. Location	₵ 46% of Blade Chord
2. Shell	
a. Matrix	Either AA6061 or AA1100
b. Fiber Orientation	$\pm 20°$
c. Wall Thickness	1.50 mm (0.59 in.)
d. Cavity Fill Material	Either Titanium Honeycomb or Cast Aluminum
3. Sheath	
a. Material	6AL-4V Titanium
b. Width	25% of Blade Chord

Table III. Preliminary Design Blade (Configuration 1) Compared With Bill Of Material

	Bill Of Material	Configuration 1
No. Blades/Stage	46	30
Blade Weight	3.86 Kg (8.5 lbs)	5.99 – 7.04 Kg (13.2 – 15.5 lbs)
Centrifugal Blade Induced Disk Load @ 3650 rpm	4.00×10^5 N (9.0×10^4 lbs)	$6.54 – 7.30 \times 10^5$ N ($1.47 – 1.64 \times 10^5$ lbs)
Centrifugal Growth		0.84 mm (0.033 in.)
Untwist		2.89 – 3.08 degrees
Maximum Static Stress		
Spar		219 MPa (31.8×10^3 psi)
Shell		290 MPa (42.0×10^3 psi)
Total Blade Stage Weight	177 Kg (389 lbs)	211 Kg (465 lbs)*
Estimated Disk Weight	163 Kg (358 lbs) Actual	182 Kg (401 lbs)*
Total Blade & Rotor Stage Weight	339 Kg (747 lbs)	393 Kg (866 lbs)*
% Total Stage Weight When Compared to Bill Of Material	100%	116%*

* Based On 7.04 Kg/(15.5 lb) Blade

Table IV. Revised Preliminary Blade Designs (Configurations 2A, 3 and 4) Compared With Bill Of Material

	Bill Of Material	2A	Configuration 3	4
Type of Spar	Titanium Blade	Solid Titanium	Hollow Titanium	Hollow Steel
Number Blades/Stage	46	30	30	30
Blade Weight	3.86 Kg (8.5 lbs)	5.08 Kg (11.2 lbs)	3.40 Kg (7.5 lbs)	5.08 Kg (11.2 lbs)
Centrifugal Blade Induced Disk Load @ 3650 rpm	4.00×10^5 N (9.0×10^4 lbs)	5.34×10^5 N (12.0×10^4 lbs)	3.56×10^5 N (8.0×10^4 lbs)	4.63×10^5 N (10.4×10^4 lbs)
Centrifugal Growth		0.94 mm (0.36 in.)	0.74 mm (0.029 in.)	0.66 mm (0.026 in.)
Total Blade Stage Weight	177 Kg (389 lbs)	152 Kg (336 lbs)	102 Kg (225 lbs)	152 Kg (336 lbs)
Estimated Disk Weight *	163 (358)	141 (310)	105 (232)	127 (279)
Total Blade & Rotor Stage Weight Including Blade Retention Ring	339 (747)	293 (646)	207 (457)	279 (615)
% Total Stage Weight When Compared To Bill Of Material	100%	86%	61%	82%

* Weight estimate based on equivalent bore tangential and blade lug bearing stresses to B/M disk. Disk stiffness requirements to eliminate coupling with 1st edgewise (2nd bending) blade resonance not deemed needed owing to blade static 2B frequencies above 130 Hz.

11
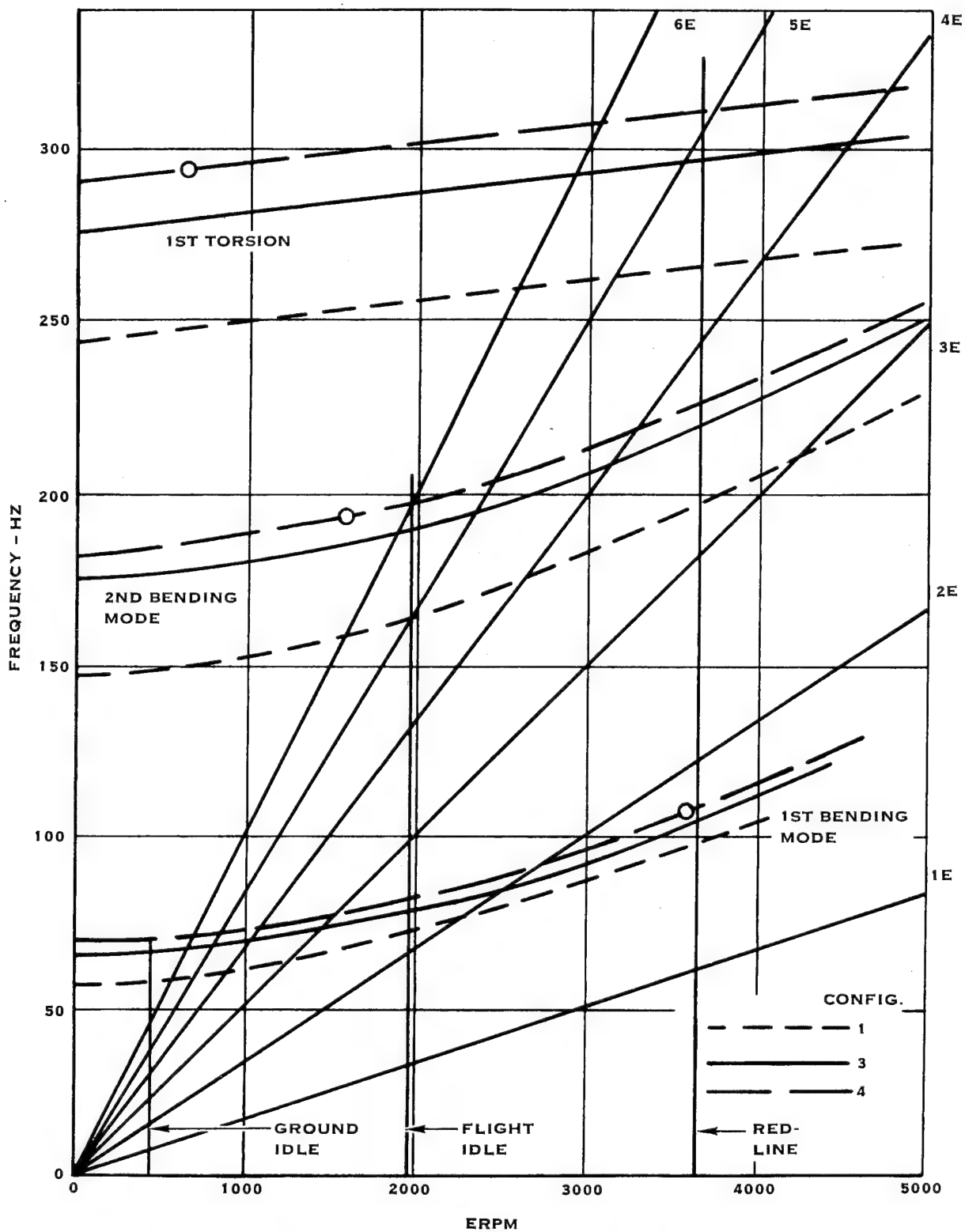
FIGURE 1. CALCULATED PRIMARY UNCOUPLED FREQUENCY MODES
PRELIMINARY DESIGN CONFIGURATIONS 1, 3 & 4

12

3.1.3 Detail Design

The configuration 2A preliminary design was selected for detail design analysis and layout drafting in two versions, one featuring AA1100 and one featuring AA6061 aluminum composite matrix materials. This effort addresses the following elements each of which is presented in separate sections:

- Layout Drafting and Configuration Definition
- Static Stress Analysis
- Dynamic Response
- FOD Assessment

Areas not addressed by this effort and not considered within the scope of the program include the following:

- Detailed Finite Element Stress Analysis
- Higher Order Plate Vibratory Response Analysis
- Blade/Disk Coupled Vibratory Response
- Aerodynamic Performance
- Detailed Component Drawings and Manufacturing Operating Sheets

3.1.3.1 Layout Drafting and Configuration Definition

The airfoil envelope and root attachment for the P&WA JT9D 3.0 aspect ratio fan blade is defined by Pratt & Whitney technical drawings TD 40152 and by Hamilton Standard drawing 739050. This existing design, which was an early generation hollow steel spar/boron aluminum shell JT9D blade, was modified only to compensate for centrifugal airfoil untwist at the design condition to meet the required airfoil dynamic position. This later effect is illustrated in Figure 2 which depicts the torsional motion and specifies the angular change in chord angle at the governing inspection stations. The maximum untwist naturally occurs at the blade tip with an angular displacement of 3.3° occurring at this location in a vacuum atmosphere. Adjustments to this value owing to gap loads previously had proven to be small.

In order to minimize flexural stress due to gas bending loads in the tangential (circumferential) direction, blades often are designed with defining airfoil sections offset in the direction of the gas load vector. This small displacement which is a function of radial position allows for a balance to be struck between a restoring moment and the gas load moment, thus minimizing stress in that plane with no aerodynamic penalty induced. Owing to modest tangential gas bending stresses computed in Section 3.1.3.2.2, this airfoil section offset stacking procedure was not employed.

13

The blade's construction which was in part defined by the preliminary design parametric study also reflects the design experience gained on the Hamilton Standard QCSEE FOD demonstration blade program. In addition, the more recent technological features such as metal bonding, spar geometric alterations for weight reduction and improved FOD resiliency, and sheath and shell geometric modifications for improved FOD resistance and lower bond stresses respectively, also are included in the blade's construction. Figure 3 illustrated typical construction of the blade at three airfoil radial stations spaced 30.48 cm (12 inches) apart. Figures 4 and 5 are copies of the design layout L-13688 which defines the extent of the blade construction defined by the effort expended. The blade consists of the following materials:

- Solid 6AL -4V titanium spar with a conventional dovetail blade root attachment.

- 3-piece 6AL -4V titanium sheath diffusion bonded assembly.

- Two 6-ply 0.2 mm (0.008 in.) boron reinforcement and AA1100 or 6061 aluminum matrix composite shells with ply orientations of the following:

    2 outer plies ± 45°

    4 inner plies ± 20°

- Two outer 6AL - 4V titanium skins of 0.2 mm thickness for erosion protection.

- Titanium honeycomb, with density yet to be defined, used to fill radial cavities between the shells fore and aft of the spar.

- AA1100 or AA6061 aluminum alloy for shell to spar and sheath to shell bonding.

In designing the blade, particular attention was paid to minimization of weight in an effort to demonstrate potential rotor stage weight savings. Table V gives the component and blade assembly weight summary for the configuration 2A blade. Also given in that table is the centrifugal load contribution that the various blade components make.

14
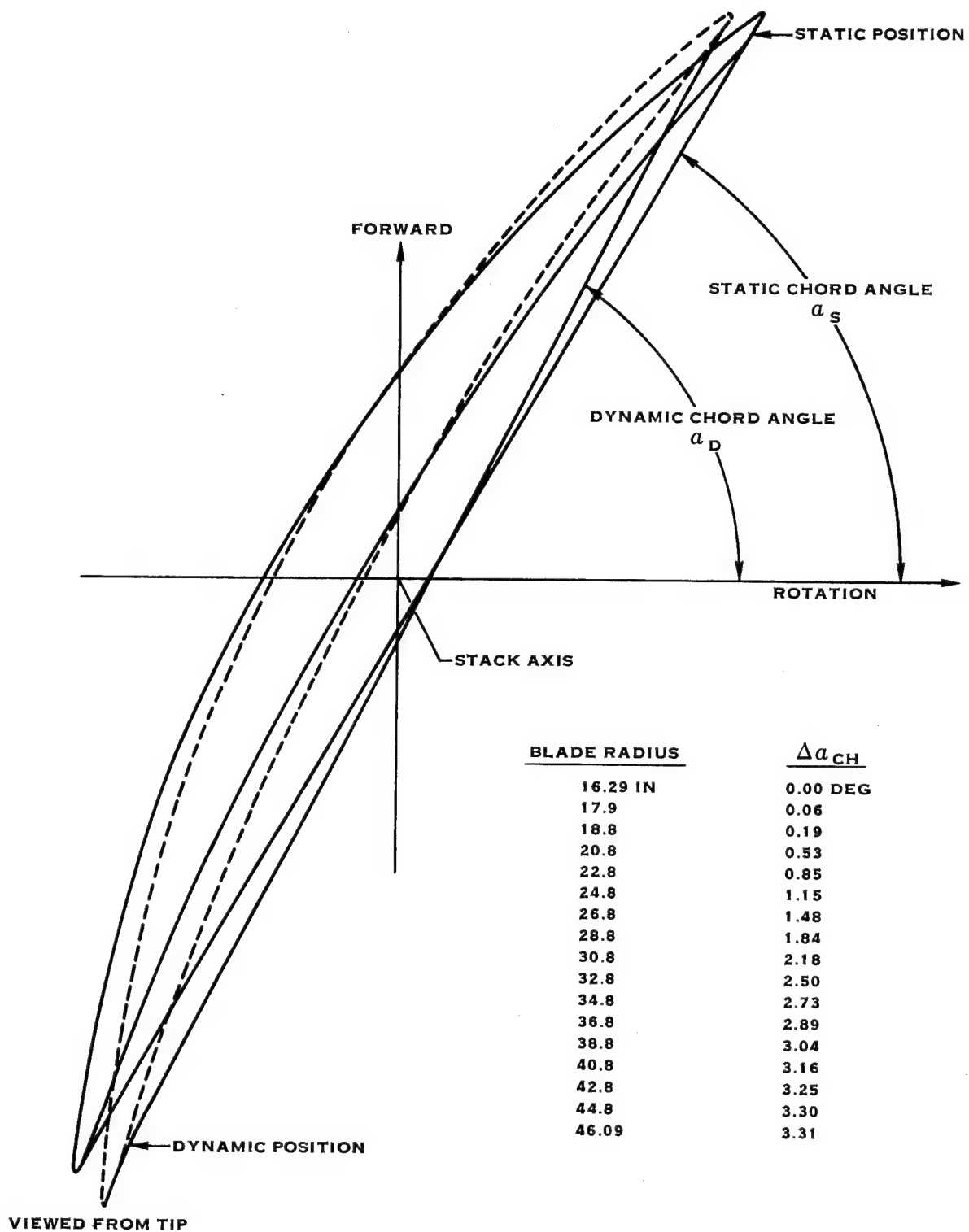
FIGURE 2. BLADE UNTWIST AT 3650 RPM REDLINE SPEED

BLADE RADIUS	Δa_{CH}
16.29 IN	0.00 DEG
17.9	0.06
18.8	0.19
20.8	0.53
22.8	0.85
24.8	1.15
26.8	1.48
28.8	1.84
30.8	2.18
32.8	2.50
34.8	2.73
36.8	2.89
38.8	3.04
40.8	3.16
42.8	3.25
44.8	3.30
46.09	3.31

15
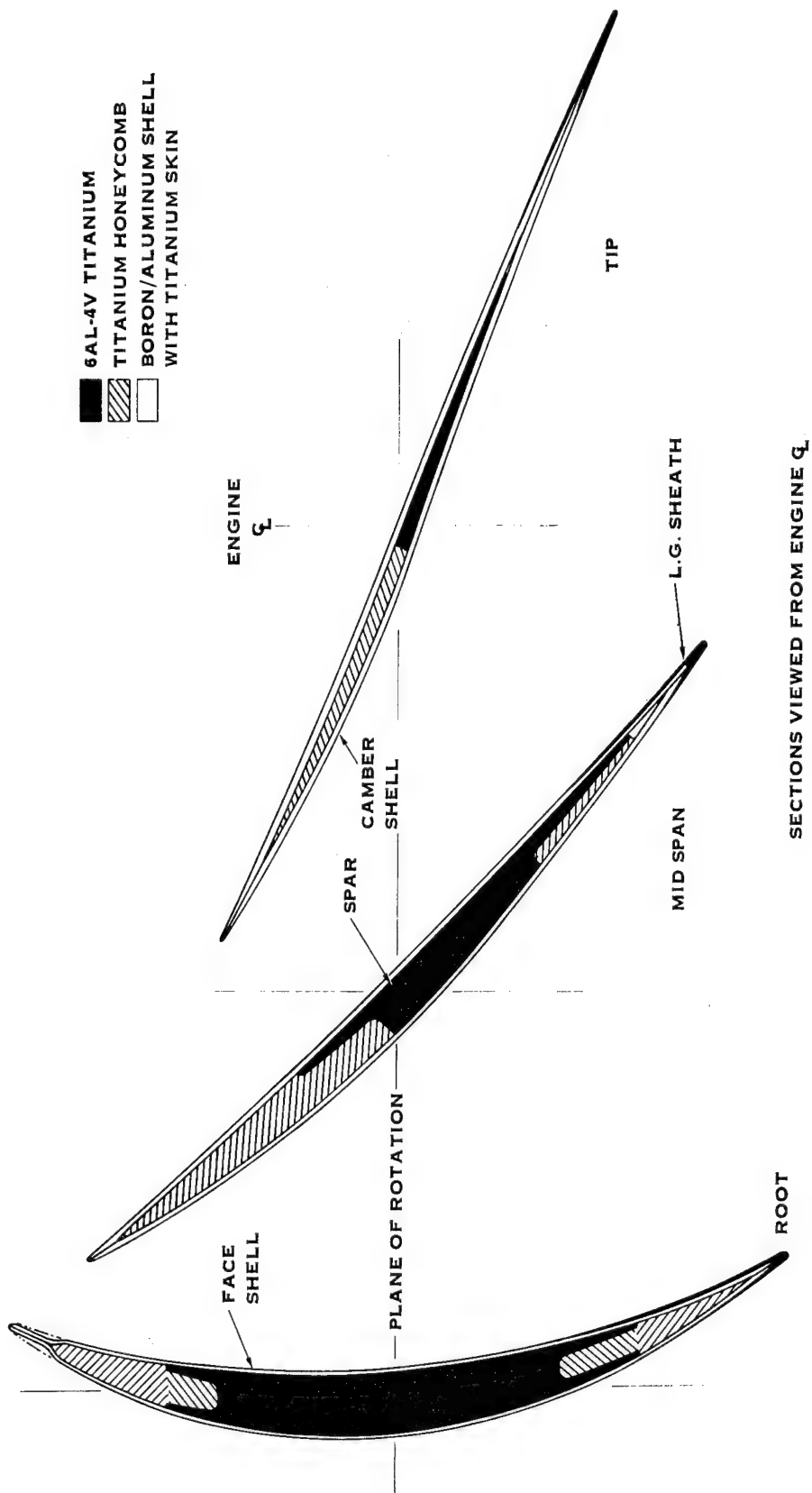
FIGURE 3. THREE TYPICAL CROSS SECTIONS OF JT9D SPAR & SHELL BLADE DESIGN CONCEPT
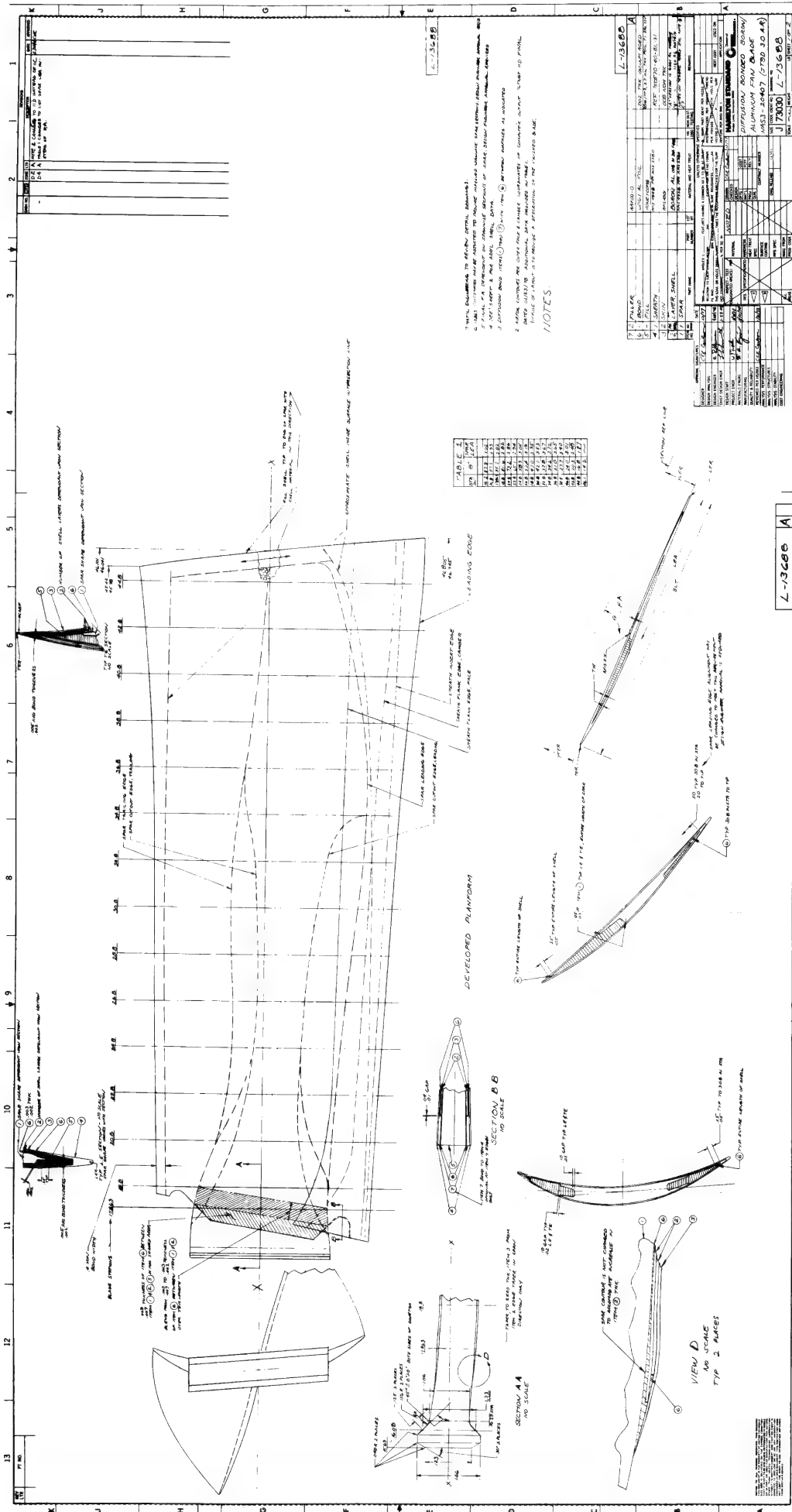
FIGURE 4. JT9D FAN BLADE CONFIGURATION (3.0 ASPECT RATIO)

FIGURE 5. JT9D FAN BLADE CONFIGURATION (3.0 ASPECT RATIO)

Table V. Blade Weight And Centrifugal Load By Component

	Weight		Centrifugal Load @ 3650 RPM	
	Kgs	Lbs	Newtons	Lbs
Spar				
Retention	1.47	3.25	1.00×10^5	2.24×10^4
Airfoil	1.83	4.03	1.95	4.39
SUB TOTAL	3.30	7.28	2.95×10^5	6.63×10^4
Shells	1.57	3.47	1.97×10^5	4.42×10^4
Sheath	0.12	0.27	0.15	0.34
Honeycomb	0.20	0.44	0.21	0.47
Aluminum Bond	0.05	0.10	0.06	0.14
TOTAL	5.25	11.56	5.34×10^5	12.0×10^4

3.1.3.2 <u>Static Stress Analysis</u>

The static stress analysis determines the static stress components resulting from centrifugal loads, gas bending moments and blade untwisting forces. The blade is analyzed at critical sections such as the blade root attachment and the shell tab ending lap joint with the spar and at each of the defining airfoil sections spaced at 5.08 cm (2 inch) intervals. The stresses are combined with the resultant values compared with a design criteria so as to judge margin of safety. In the case of the subject blade the determination is made that the static stress will meet a structural adequacy criteria leaving capacity to absorb a superimposed cyclic fatigue stress.

3.1.3.2.1 <u>Blade Root Attachment</u>

The blade root attachment stress calculation is a computation of four stresses, the dovetail bearing stress, the root shearing stress, the root tensile stress and the combined bending and tensile corner stress. The bearing stress is computed by dividing the centrifugal load, resolved into components normal to the dovetail surface, by the bearing area. The root shear stress is computed in like fashion with the root shear area divided into the centrifugal load. The tensile stress is the tensile area divided into the centrifugal load and the corner stress is the summation of root bending and tensile stresses. Given in Figure 6 is the computation of the root stresses and the margin of safety for both stress conditions when measured against the respective design criterias. With margins of safety ranging from 72 to 706%, it is readily apparent that the root system is adequately designed.

CENTRIFUGAL FORCE 5.34 X 10^5 N/(120X10^3 LBS)

BENDING MOMENT 1265 N·M/
(11,300 IN·LBS)

41.38 CM RAD
(16.29 IN)

F_a F_N

C

B

D

A
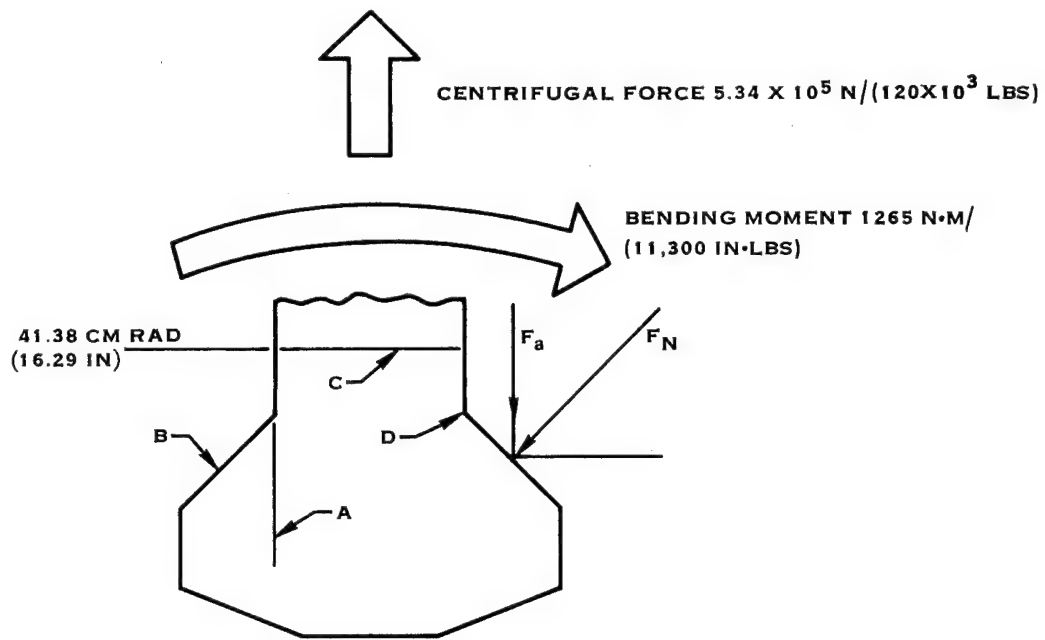
LOC	DES. ALL. MPa/(KSI)	STRESS MPa/(KSI)	MARGIN SAFETY
A	600 (87)	138 (20)	335%
B	414 (60)	241 (35)	72%
C	1000 (145)	124 (18)	706%
D	710 (103)	193 (28)	268%

FIGURE 6. BLADE ROOT STRESS ANALYSIS

3.1.3.2.2 Airfoil Static Bending and Centrifugal Stresses

The airfoil static stress analysis utilizes the following inputs to compute average stress at a given location:

- Cross section area

- Moments of inertia

- Airfoil section position in relation to its center of gravity

- Material stiffness and density properties

- Rotor speed

- Aerodynamic loads

In place of an actual rotor pressure distribution map, an approximation of typical compressor blade loading is utilized for convenience. This approximation assumes a distribution proportional to the radius squared times the blade chord length, i.e.,

$$\frac{r_1^2 \, b_1}{\Sigma \, r_N^2 bn} + \frac{r_1^2 \, b_2}{\Sigma \, r_N^2 bn} \, , \text{ etc.}$$ The application of this load is placed at 1/4 chord length

from the leading edge. The distribution is resolved into an axial component $(r^2 b \cos\theta)$ whose integral over the blade length is set equal to the rotor axial thrust and a tangential component, $(r^2 b \sin\theta)$, whose area integral is set equal to the rotor torque.

Where:

r = blade defining cross-section radius from engine centerline.

b = chord length of defining cross-section.

θ = angle formed between defining cross-section chord line and plane of rotation.

Given in Table VI are the 0/90 degree room temperature mechanical properties used in the design for the two aluminum matrices shells based on Hamilton Standard test data. As this table illustrates, only the design limit strength values differ between alloy systems. The difference in 0 and 90 degree tensile modulus properties between alloy systems presented in Section 3.2.3.1 is deemed based on too small a data base to warrant distinguishing the two systems by different properties for design purposes. The computerized static bending and centrifugal stress program properly orients each ply and computes an effective overall shell modulus. The program next

adjusts the material property inputs so as to produce "Effective" and "Equivalent" geometric properties which it uses to compute an effective stress. The effective area and area moments are a summation of the spar property and a shell property with the latter ratioed by the shell modulus divided by the spar modulus. These properties are used in computation of the effective bending stress. In like fashion the equivalent area and area moments have the shell property ratioed by shell density to spar density which is used to compute centrifugal stress. The bending stress is then adjusted for the actual shell modulus which is then added to the equivalent centrifugal shell stress to produce the blade maximum skin stress as given in Figure 7. This figure gives the two stress components and the vector sum which occurs on the concave side. The maximum computed stress of 363 MPa (52.7 ksi) occurs at the 45.5 cm (17.9 in.) station and similar stress levels extend over an inboard span length of 22.6 cm (8.9 in.) with an approximate linear decay to zero stress at the tip. Superimposed on Figure 7 is an estimated design allowable limit calculated by a rule of mixtures and based on the 0/90 degree tensile data. These values of 317 MPa (46 ksi) for AA6061 and 200 MPa (29 ksi) for AA1100 are both exceeded by the combined stress and by the centrifugal stress alone in the case of the AA1100 matrix alloy system. Two significant factors will illustrate that in all probability the shell stress will in fact be well within adequate safety margins. First the standard design practice of offsetting airfoil sections done to minimize gas bending load induced bending stresses was not performed. When this is done, bending stress levels below 35 MPa (5 ksi) can be expected. The static stress surveys performed on the APSI blade (A/F Contract F33657-73-C-0619) on which this design practice was employed had excellent static stress agreement between design values and test results and was characterized by a linear strain to speed behavior which illustrated a spar dominated/centrifugally loaded dominated load mechanism.

The second factor which would be employed as a standard practice would be the generation of tensile data on specimens simulating the shell construction. As given in Figure 8, which simulates a typical shell layup stress/strain elastic behavior, the true limit should be based on a percentage of strain at failure owing to the shell's non-linear elastic stiffness behavior. Figure 8 further illustrates that by idealizing the shell stress/strain behavior with two linear modulii as shown, or three if that significantly improved material behavior modeling, and using the previously computed combined static shell stress, an evaluation of a computed strain versus a design limit strain would be made. This entails defining stress limits over which a modulus value (E1, E2, etc.) is applicable as to enable calculation of a new predicted strain. Design limit strain would be set at perhaps 75 - 80% of strain to failure to provide capacity for additive dynamic loads. This "tool", which includes the supportive tensile data of simulated composite shell structures which defines the necessary stress/strain relationship to properly evaluate shell stress values, was not produced thus the interpretation of the stress levels against a true design limit cannot be made on this design.

Table VI. Boron Aluminum Shell Mechanical Properties

	0.2 mm B/AA6061/6Al-4V TIT		0.2 mm B/AA1100/6Al-4V TIT	
	SI Units	English	SI Units	English
Tensile Modulus				
0 Deg.	184 GPa	27.7 ksi	184 GPa	26.7 ksi
90 Deg.	117	16.9	117	16.9
Shear Modulus	48	7.0	48	7.0
Poisson's Ratio				
ν_{12}	0.23	0.23	0.23	0.23
ν_{21}	0.17	0.17	0.17	0.17
Design Limit Strength				
0 Deg.	669 MPa	97 ksi	586 MPa	85 ksi
90 Deg.	110	16	43	6.3
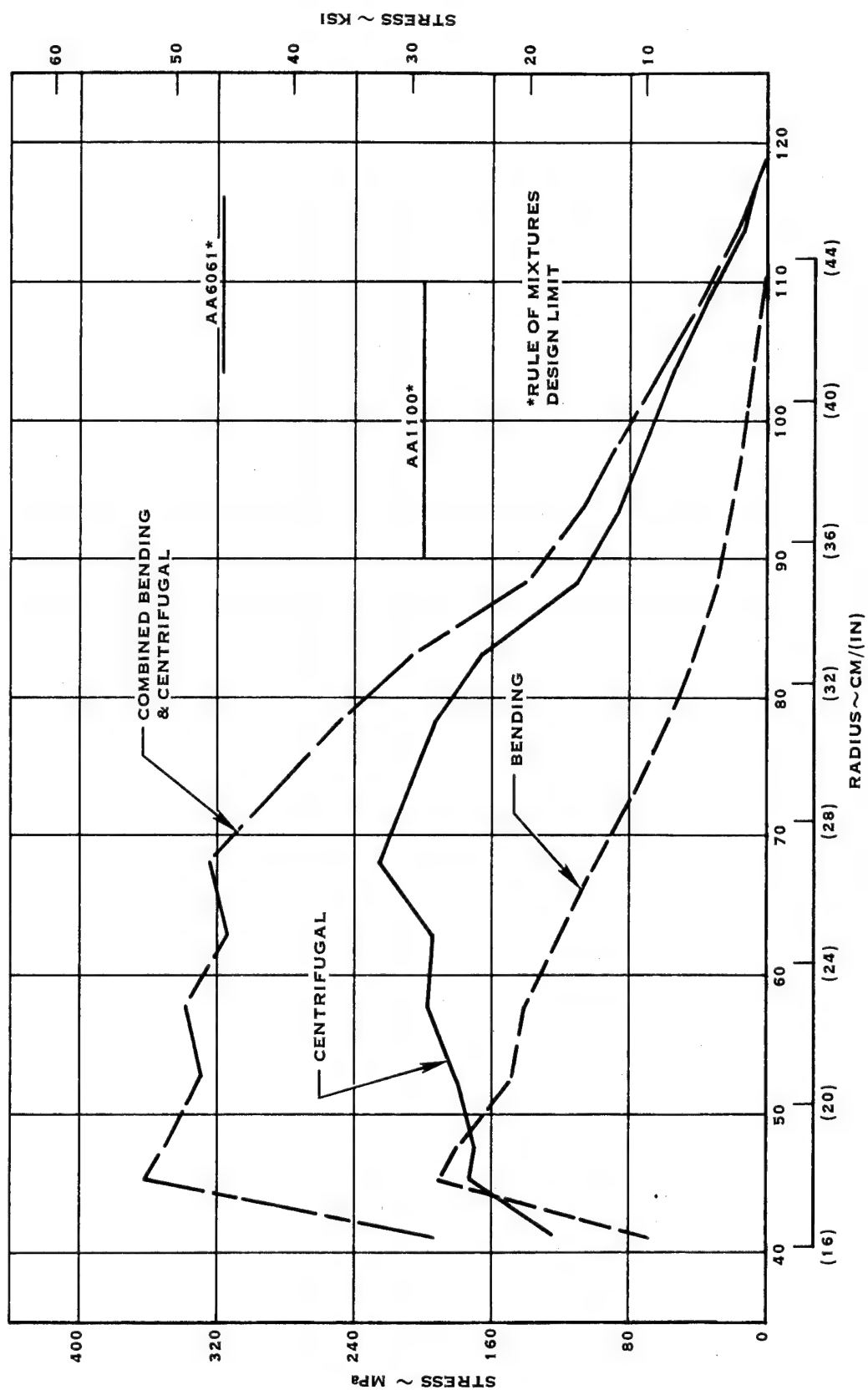
FIGURE 7. MAXIMUM STATIC SHELL STRESS AT 3650 RPM

27
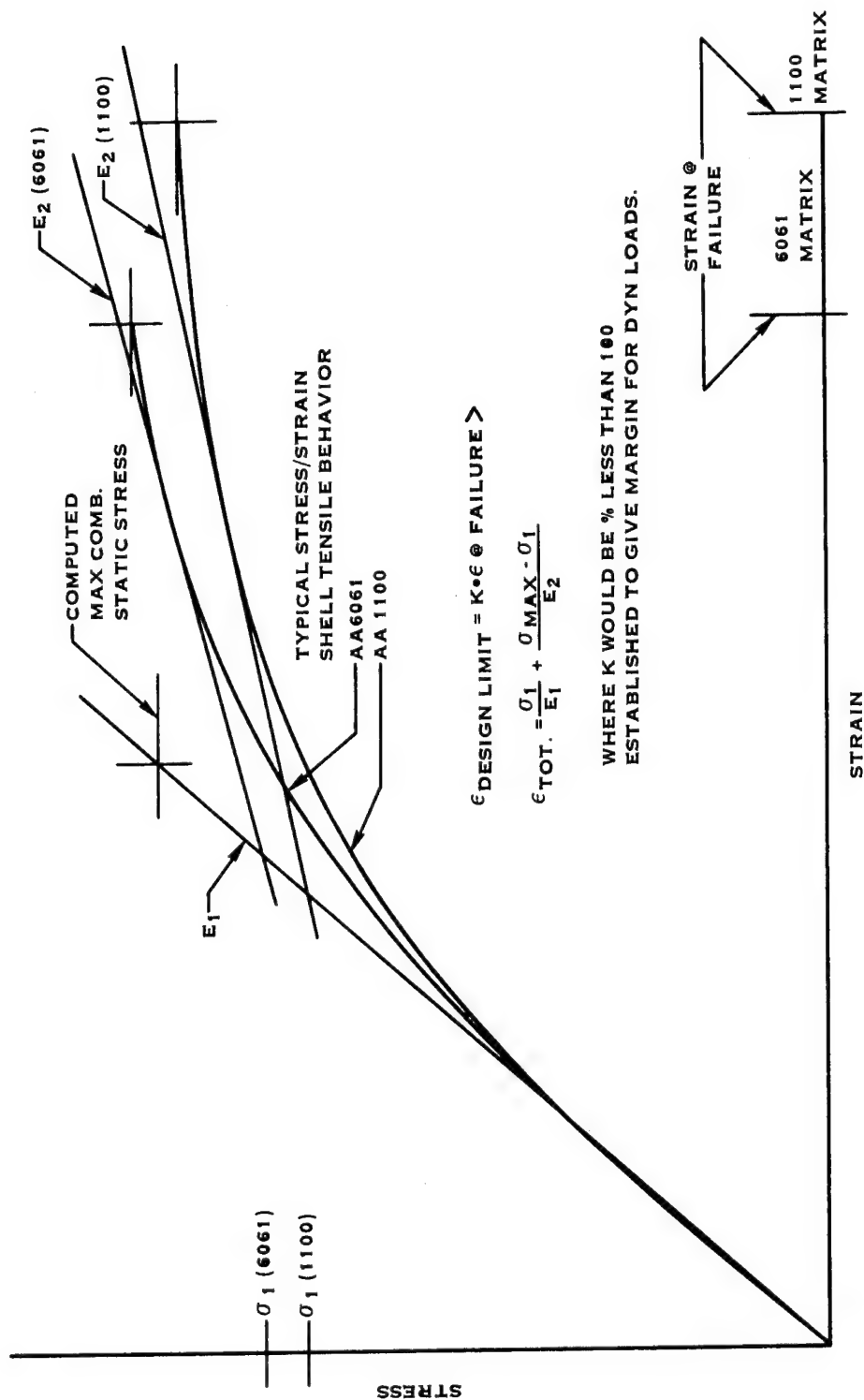
FIGURE 8. METHOLOGY UTILIZED TO ESTABLISH DESIGN ADEQUACY BASED ON NON LINEAR SHELL TENSILE DATA

28

3.1.3.2.3 Torsional Stress

In addition to the centrifugal and bending induced stresses, the blade will also incur stresses owing to a torsional displacement. The net effect of the centrifugal and gas bending loads cause the airfoil to twist toward a more axial airfoil chord alignment. Discussed in Section 3.1.3.1 was the calculated change of the airfoil chord angle made with the plane of rotation due to the induced loads. For the calculation, the blade is assumed to be a pre-twisted, continuous and geometrically non-uniform shaped rotating cantilever beam. The untwisting blade moment puts the airfoil extremities into compression while the center section is put into tension. The program, assumes the cantilever beam forms a continous surface with the supported end rigidly restrained in three axis. With the spar/shell construction featuring a substantial (18% of chord) airfoil leading and trailing edge undercut below the ID flowpath. The restrained boundary condition is not satisfied at these locations by the program. With substantial local stress calculation error induced by this design feature in the torsional beam analysis, the recent direction at Hamilton Standard has been to incorporate this stress analysis into the finite element [Bestran] stress calculation procedure. Therefore with that design tool not used for this program, no torsionally induced radial stress is presented. The torsional deflection data previously presented also is effected to a substantially lesser extent by the lack of restraint for the inboard airfoil extreamities.

3.1.3.3 Blade to Shell Tab Ending Stress Analysis

The spar/shell construction features the use of the spar to shell bond joints on the convex and concave sides of the spar as the means of load transfer from the airfoil to the blade root. The load shared by these bond joints results primarily from centrifugally induced forces on the shell, sheath and fill materials. Through both analysis and experience, it has been determined that large stress gradients occur at the inboard end of the shell in a tab ending area of finite radial length. In order to develop means of minimizing this local high stress, a comprehensive elasticity analysis in combination with laboratory overlap shear testing has been performed. The analysis considers all the load paths in the bi-axially loaded bond joint in the computation of its maximum principal joint stress. Lap shear specimen tests taken to failure provide average bond shear stress and substrate tensile stress data used to correlate the analysis to a test basis. A theoretical stress distribution whose integrated average stress matches the test shear stress data is thus generated. This solution is governed by elastic material properties, therefore, its absolute value computes higher than actual material strength values. The program does not recognize the plastic material flow and the resultant redistribution of stresses that would take place in real materials. This shortcoming is judged acceptable provided that test average shear stress data agrees with or is less than bond material shear strength data and that the product design computes a maximum principal stress no greater than 50% of the theoretical maximum allowable principal stress.

Given in Figure 9 are both the design model of the scarf cut tab ending and the evolved blade tab ending design. The above described design analysis indicated that a local bond thickness increase from 0.05 mm to 0.2 mm provided substantial shear stress reduction. In addition, the taper on the scarf cut also influences stress distribution which in this design was set at 19.1 mm (0.75 inches) of span length for a reduction of the inboard shell thickness from 0.61 mm (0.024 inch) to a sharp edge. The maximum computed bond material principal stress for the design was 222 MPa (32 KSI) which is approximately 25% of the theoretical maximum allowable principal stress of 858 MPa (124 KSI) which is based on a test average shear stress of 55 MPa (8 KSI). With the 55 MPa well within the annealed AA6061 aluminum alloy shear strength text book value of 83 MPa (12 KSI) and with the peak design stress being 25% of theoretical maximum value at failure, it is judged that the design meets the static structural criteria. A vibratory stress limit to be superimposed on the above static stress was not computed but is a feature available in the tab ending stress analysis program.

DESIGN MODEL TAB ENDING

M

P/A

SPAR

BOND

P/A

0.2MM
(0.008")

COMPOSITE
SHELL

0.2MM
(0.008")

M

L

BLADE DESIGN TAB ENDING

SPAR

BOND

0.05MM
(0.002")

0.2MM
(0.008")

TITANIUM SKIN
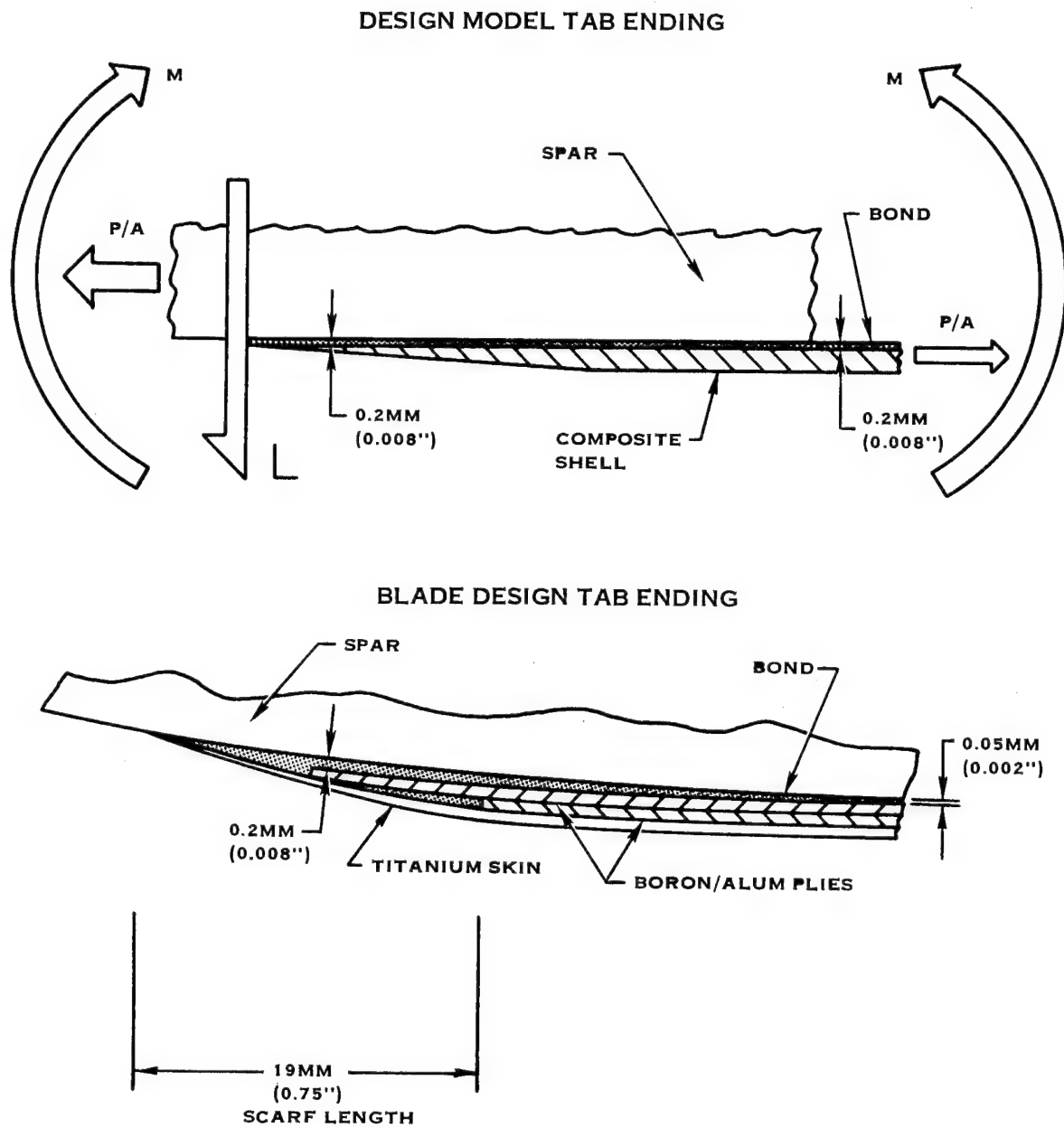
BORON/ALUM PLIES

19MM
(0.75")
SCARF LENGTH

FIGURE 9.   TAB ENDING DESIGN MODEL SIMULATING BLADE TAB ENDING DESIGN

31

3.1.3.4 Dynamic Response

A dynamic response analysis of the blade was made utilizing beam theory which assumes the blade is a rotating, twisted geometrically non-uniform cantilever beam made from a continuous isotropic material. The program computes the first three bending modes and the 1st torsion mode in a static and rotating environment. Given in Figure 10 is the uncoupled Resonant Frequency Response Diagram (Campbell Diagram) which plots the first two bending modes and the 1st torsion mode frequencies verses engine rotational speed. This diagram allows for determination of the existence of a potential low integral order engine induced vibration source stimulating a blade resonance within the engine operating envelope. The basic requirement is to minimize the potential of driving the blade in resonance by placing its intersection with the driving source either outside the operating envelope or at least at engine speed conditions only encountered in power lever transients. The Campbell Diagram has both the computed blade resonance and a predicted blade resonance which factors the computed value by an experience factor. Experience has shown that beam theory, with the assumptions necessary for its use, has historically predicted bending resonances too high and torsion modes too low. The 15% correction factor is a reasonable correction based on previous Spar and Shell blade programs. Given in Table VII is an analysis of these three resonances and low order excitation sources. The 1st bending and 2E intersect at 1600 rpm and the 2nd bending and 3E intersect at 2880 rpm are both in the operating range. However, both intersects are located at a substantial distance from the key constant engine speed points highlighted. The judgment thus is made that the success criteria for primary resonant frequency resonance has been met. In Hamilton Standard design efforts employing a finite element analysis the prediction of resonance frequencies has been made with extreme accuracy thus when employed it allows for the elimination of the requirement for experience factors.

The blade was analyzed for potential subsonic and supersonic torsional flutter response. The acceptance criteria for both is P&WA empirically derived thresholds for flutter prone responses. Each is based in part on 1st torsion vibratory response at operating speed with a minimum value of 150 Hz deemed the minimum acceptable frequency required. With a predicted torsional frequency of 295 Hz at redline speed the judgment is made that this design has met the criteria of avoidance of flutter prone operating conditions.

Table VII. Analysis of Primary Resonances & Excitation Sources

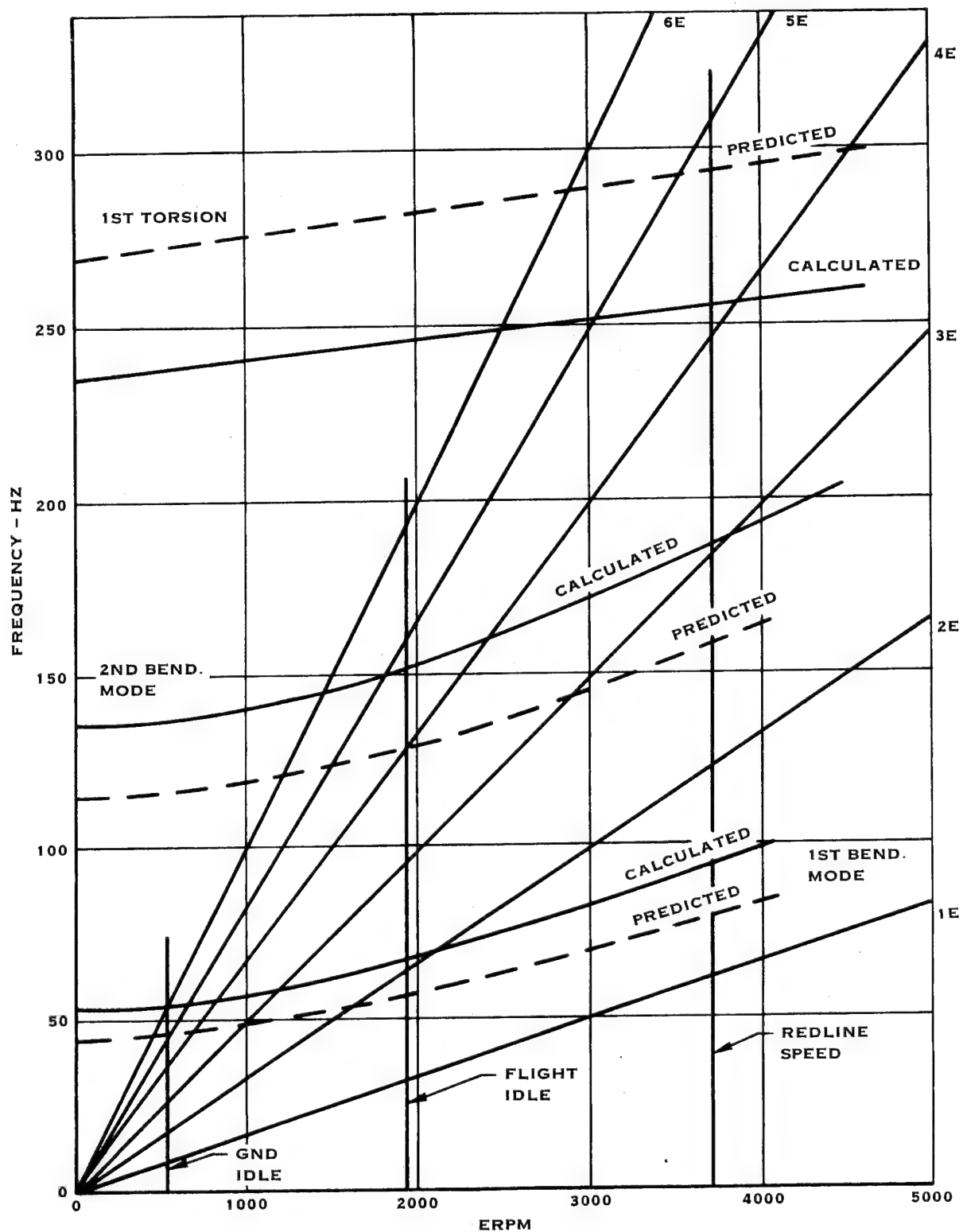| Resonance	Excitation	Intersection Within Operating Envelope
1st Bending Mode	1E	31% clearance @ redline speed
	2E	Intersect @ 1600 rpm– a non steady state operating speed.
2nd Bending Mode	2E	52% clearance @ redline speed.
	3E	Intersect @ 2880 rpm– a non-steady operating speed.
1st Torsion	3E	62% clearance @ redline speed.
	4E	21% clearance @ redline speed.

FIGURE 10. CALCULATED & PREDICTED PRIMARY UNCOUPLED RESONANT FREQUENCY
RESPONSE CONFIG. 2A

34

3.1.3.5 FOD Assessment

The objective of the FOD assessment was to analytically predict the survivability of the blade when impacted by 50% of a 1.36 Kg (3 lb.) bird at a highly vulnerable airfoil station. Review of the governing FAA Federal Aircraft Regulation 33 (FAR 33) which provides the turbine engine impact criteria and the subject JT9D turbofan engine flight envelope revealed that this slice mass exceeds the maximum capability of the engine in all but one flight sector. Figure 11 illustrates the fact that the imposed criteria exceeds the 1.82 Kg (4 lb.) FAA large bird maximum slice size at all flight conditions and impact zone locations except above 340 Kt true airspeed (TAS). Regulatory control of climb speed to 250 Kts indicated airspeed (IAS) (291 TAS) exists on most commercial flight routes with only unpopulated areas permitting up to a 340 IAS (396 TAS) within a 10,000 Ft cealing in which a probability of bird impacts exists. Carried further, Figure 11 also gives the impact velocity vector normal to the three airfoil sections which when used to compute impact momentum given in Figure 12, illustrates the severity of the imposed 0.681 Kg (1.5 lb.) slice size as compared to potential conditions within the flight envelope. The impact momentum normal to the blade section chord is of a magnitude of 81.7 N·sec which substantially exceeds that at the vulnerable 80 and 95% span airfoil stations which have maximum impact momentum values of 37.8 and 26.5 N·sec, which occur at 190 and 160 Kt TAS, respectively.

Irrespective of the severity of the analytic FOD test condition, the missile impact analysis was performed with this condition imposed on the airfoil with the results to be discussed in section 3.1.3.5.1. Section 3.1.3.5.2 discusses Hamilton Standard's correlation of test experience with the analytic analysis.

3.1.3.5.1 Missile Impact Analysis

The analysis employed is a computerized impact analysis developed by Hamilton Standard to predict time histories of loads, deflections and stresses. The program divides the impact object into six equal cylindrical slice elements treating these as fluid jets impinging upon the pressure side of the blade's leading edge. The blade's mechanical and geometric properties are inputted along with the impact velocity and mass conditions. The program was developed for three aspects of an impact event namely gross blade response, local blade response and local chordwise stressing. The three degrees of freedom gross blade response analysis was that program portion selected for use with this design. The combination of time restraints and previous QCSEE strain gage verification testing of this program portion led to confining the analysis to the gross blade response. This analysis assumes that the blade responds to an impact in its primary flatwise bending, edgewise bending, and torsional vibration modes. The blade is represented as a spring-lump mass system in which the mass in each mode is located at the impact station and the spring rate for each mode

35

is obtained by applying a static load at the impact station in the respective direction of motion. The mass for each mode is calculated so as to give the same frequency in each mode, in combination with the above respective spring rate, as the respective blade frequency. The analysis includes the effects of centrifugal stiffening, blade twist, retention stiffness and orientation, damping and blade motion in impact. Post-rocking behavior of blades that rock or exceed their retention moment capability can be determined by running the analysis in two stages. The analysis yields the maximum bending and torsion deflections and stresses as a function of selected time intervals from the impact event occurrence.

The impact object for this analysis as stated is taken as a 1.36 Kg (3 lb.) bird with an average density of 0.68 gms/cc (42.5 lbs/ft^3) which is assumed to be in a right cylindrical shape with a length to diameter ratio of 2:1. It is further assumed that the object's alignment is such that the "bird's" axis is normal to the resultant impact vector which services to cut right cylindrical impact sections. Figure 13 schematically gives the kinematics of the bird impact event and Table 8 defines the actual impact event conditions. As is illustrated by the table the means to achieve the target slice mass was to determine the slice mass at 125 Kt sea level takeoff flight condition and to then reduce the airfoil number from 30 to 10 to achieve a 0.657 kg (1.45 lb.) slice mass. From this input data time histories of impacting load, as well as blade reaction loads in the X, Y and torsional directions are calculated by the program. Corresponding time histories of three basic deflections, X, Y and Θ, at the impact site are also generated. The X-deflection is taken parallel to direction of the blade natural flatwise mode of vibration with the Y-deflection (primarily the edgewise deflection) normal to X. The torsional deflection is taken about the blade center of torsion at the impact station. The time histories of load and deflection for the 0.657 Kg impact event, which are calculated and plotted by the computerized analysis, are shown in Figure 14 and 15, respectively. The maximum deflection is in the flatwise X-direction amounting to 8.4 cm (3.3 in) at the impact site and 12.2 cm (4.8 in.) at the blade tip approximately 3.9 milli-seconds after initial impact. This deflection in the flatwise direction results in spanwise bending stress peaks at two locations along the blade span. These are generated by a second portion of the computer program which calculates the max chordwise stress at select span locations at specific instances of time after impact and are plotted by the program as shown in Figures 16 and 17. Three regions on the blade experienced high stresses owing to the impact event. Given below are those computed peak stress values at the root, mid span and impact site.

Location	Flatwise Stress	Edgewise Stress
41.4 cm (16.3 in)	− 672 MPa (97.5 ksi)	− 1103 MPa (160 ksi)
81.28 (32)	− 1206 (175)	− 138 (20)
102.87 (40.5)	+ 1586 (230)	----- -----

Obviously the calculation produced stress levels in excess of the mechanical properties of the blade. To evaluate stress levels which calculate above the ultimate strength of the titanium spar the interpretation of the calculation begins with recognition of the true material's behavior which can be idealized as an elastic/plastic linear stress/strain behavior as shown in Figure 18. The two envelope defining points are the 0.2% yield strength and the ultimate strength. The load portion which cause bending stresses to exceed yield strength is idealized to strain at a plastic modulus rate until reaching ultimate strength. Upon reaching the ultimate strength at the outer fiber, further load goes into raising the fiber stress of inboard fibers in a linear plastic distribution until the yield point is reached at a point between the neutral axis and the outer fiber. Further inboard this stress is distributed in a linear elastic manner until zero stress is reached at the neutral axis.

The abbreviated approach taken to evaluate the margin of safety with impact loads which generate stress levels in excess of the spar material yield strength is a comparison of the kinetic energy of impact with the total strain energy necessary to bring the spar outer fiber to ultimate stress. An idealized spar stress distribution is assumed based on the impact stress and gas bending static stress calculation is shown in Figure 18. A bending stress distribution shown in Figure 18 assumes that the maximum permitted load takes the spar outer fiber only to ultimate strength stress level. Plastic and elastic linear stress distribution is based on a central neutral axis with the location of the yield point stress spar found by trigonometry. This neutral axis placement naturally is inconsistent with a combined loaded member (centrifugal and bending loads), however, for this gross structure adequacy approximation it was felt justifiable.

The kinetic energy of impact normal to the 80% span leading edge by an 0.681 kg (1.5 lb.) bird slice is 7.2×10^3 N·M (5.3×10^3 lb·ft) assuming conservation of energy, which is highly conservative. This kinetic energy is then compared to a maximum potential energy of flexure. Employing the distribution constraints discussed above, a total potential strain energy of flexure of 8.1×10^4 N·M (6×10^4 lb·ft) can occur before failure. This approximate 15 : 1 ratio of strain energy to impact kinetic energy

thus indicates that a very large margin of safety exists. With this amount of margin it was judged that the design met a structural adequacy evaluation and, it was not considered necessary to perform a more rigorous plastic analysis.
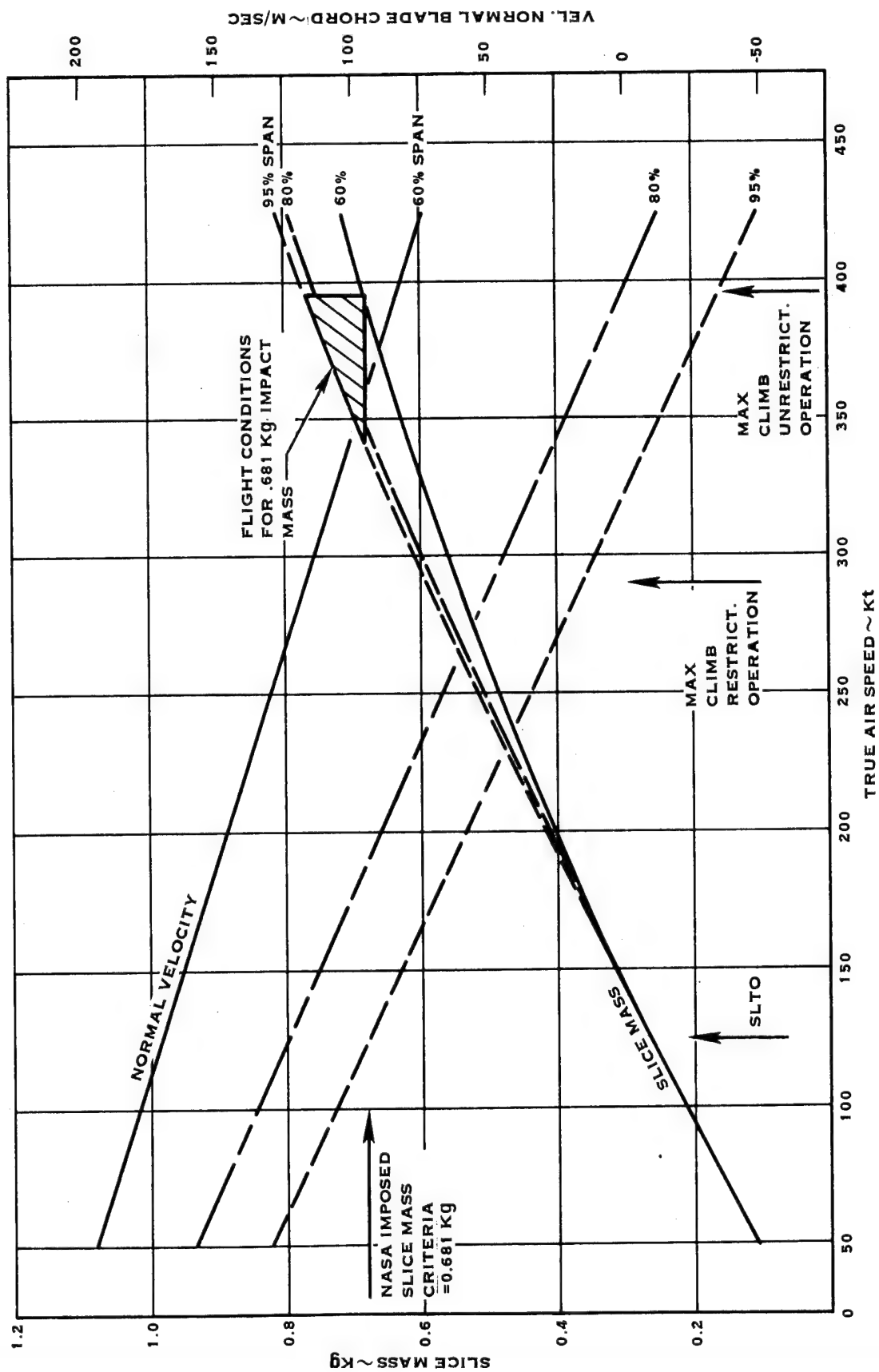
FIGURE 11. BIRD FOD IMPACT CRITERIA COMPARED WITH POSSIBLE FLIGHT CONDITIONS WHICH WOULD MEET SAME WITH F.A.R. 33 LARGE BIRD IMPACT CRITERIA
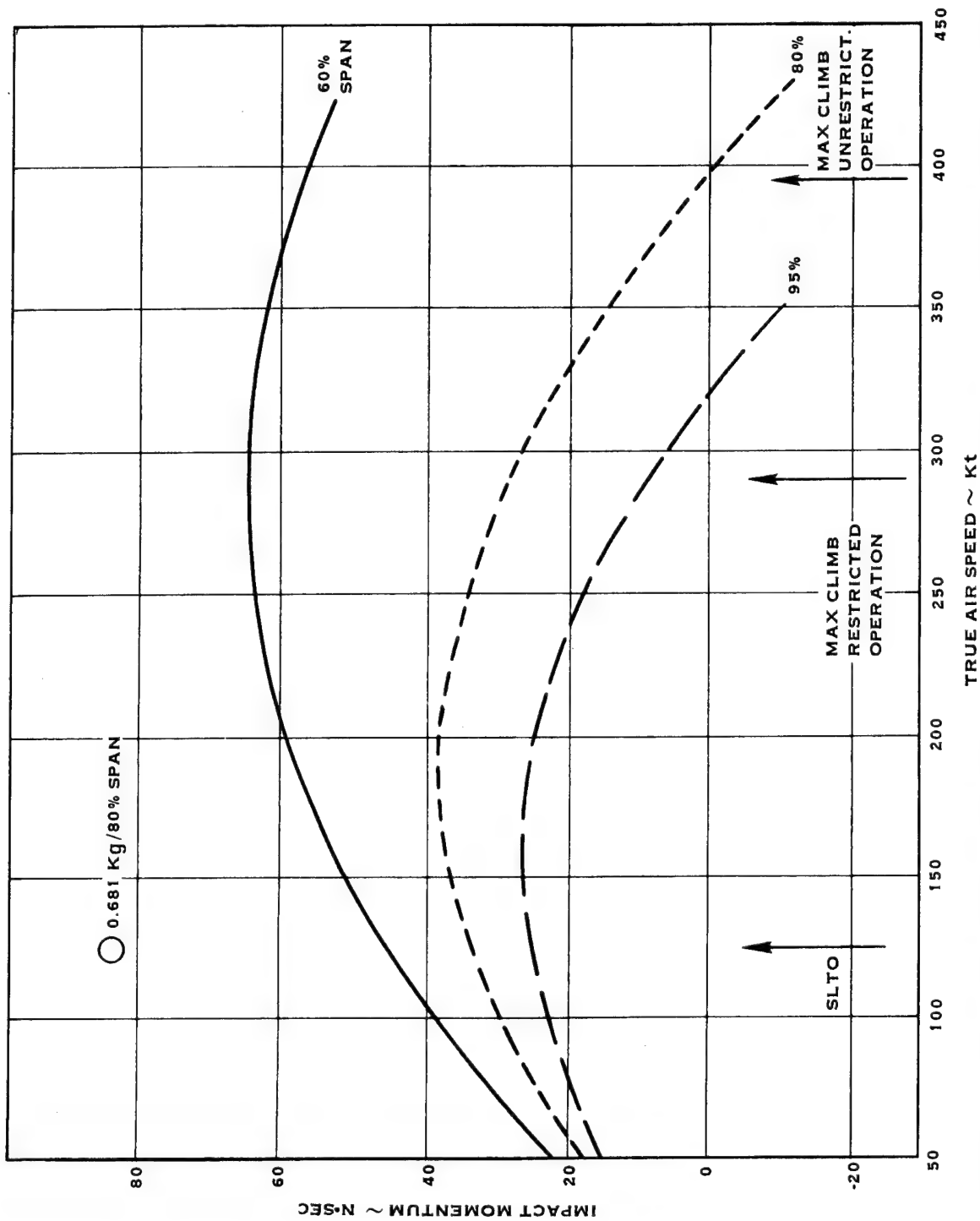
39

FIGURE 12. BIRD FOD IMPACT CRITERIA COMPARED WITH KINEMATICS OF POSSIBLE IMPACT EVENTS WHICH WOULD MEET F.A.R. 33 LARGE BIRD IMPACT CRITERIA
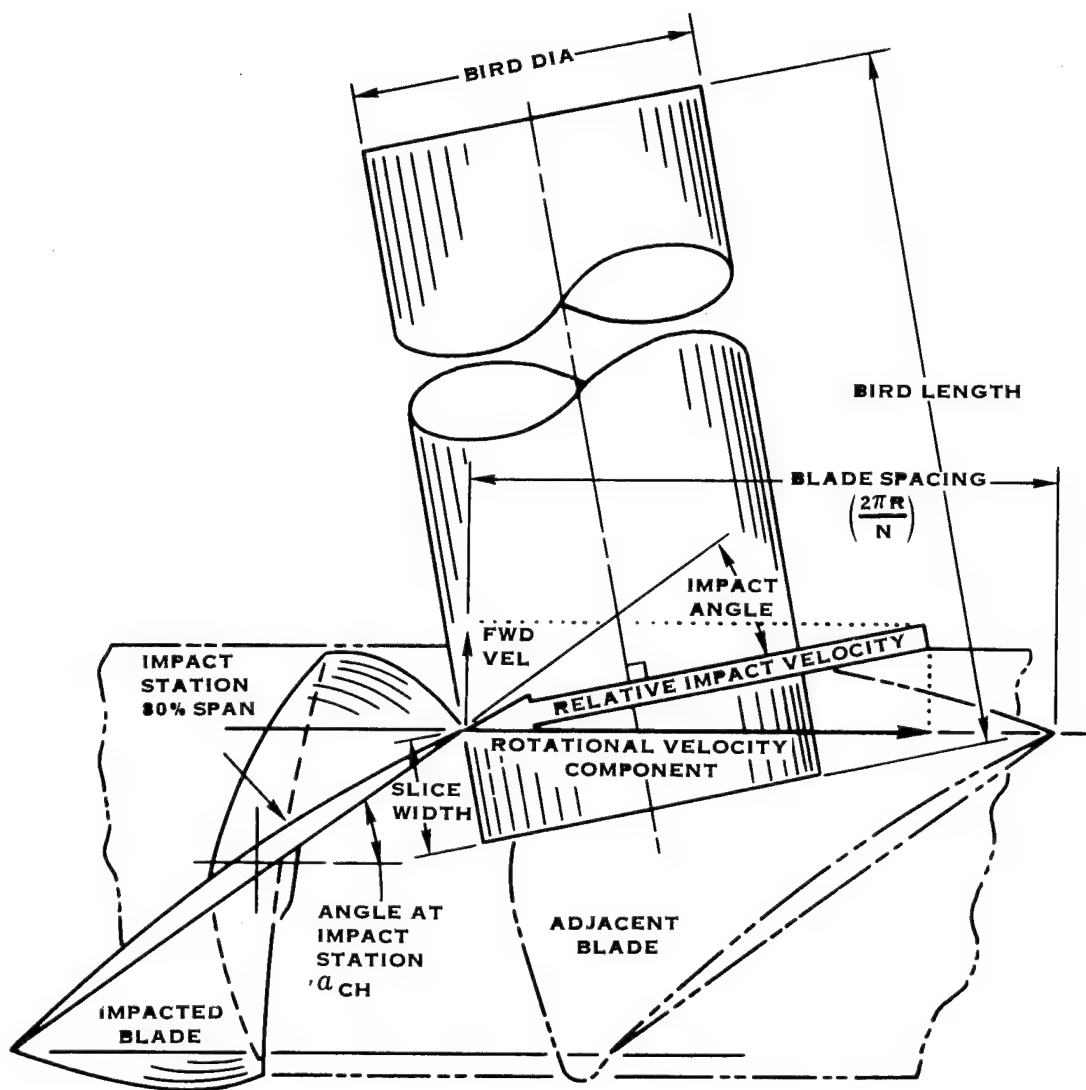
FIGURE 13. FOD IMPACT KINEMATICS

41

Kinematics of Two Analytically Computed JT9D Impact Events

	JT9D SLTO/125 SI Units	KT Flight Velocity English Units	JT9D 1 1/2 Lb Slice of 3 Lb Bird SI Units	English Units
"Bird" Characteristics				
Weight	1.36 kg	3 lb	1.36 kg	3 lb
Density	0.68 gms/cc	42.5 lbs/ft^3	0.68 gms/cc	42 lbs/ft^3
Dia./Length	10.85/21.69 cm	4.27/8.54 in	10.85/21.69 cm	4.27/8.54 in
Coeff. Restitution	0.0	0.0	0.0	0.0
Blade Parameters				
Rad. Impact Loc.	102.87 cm	40.5 in	102.87 cm	40.5 in
% Span	80	80	80	80
Impact Station & Plane Rot.	0.48 rad	27.5 deg	0.48 rad	27.5 deg
No. Blades/Disk	30	30	10 *	10 *
Angle Flatwise Mode	2.70 rad	154.8 deg	2.70 rad	154.8 deg
Angle Edgewise Mode	1.42	81.1	1.42	81.1
Impact Parameters				
RPM	3650	3650	3650	3650
Flight Velocity	64.3 m/sec	211 ft/sec	64.3 m/sec	211 ft/sec
Result Impact Vel.	398.4	1307	398.4	1307
Normal Impact Vel.	124.4	408	124.4	408
Impact with Bld. Chord	0.318 rad	18.2 deg	0.318 rad	18.2 deg
Slice Length/Mass	3.48 cm/ 0.219 kg	1.37 in/ 0.482 lb	10.44 cm/ 0.657 kg	4.11/1.44 lb
Normal Impact Momentum	27.24 N · SEC	6.12 lb · SEC	81.73 N · SEC	18.37 lb · SEC
Normal Impact K.E.	1.69 x 10^3 N·M	1.25 x 10^3 lb ft	3.74 x 10^3 lb ft	3.74 x 10^3 lb ft

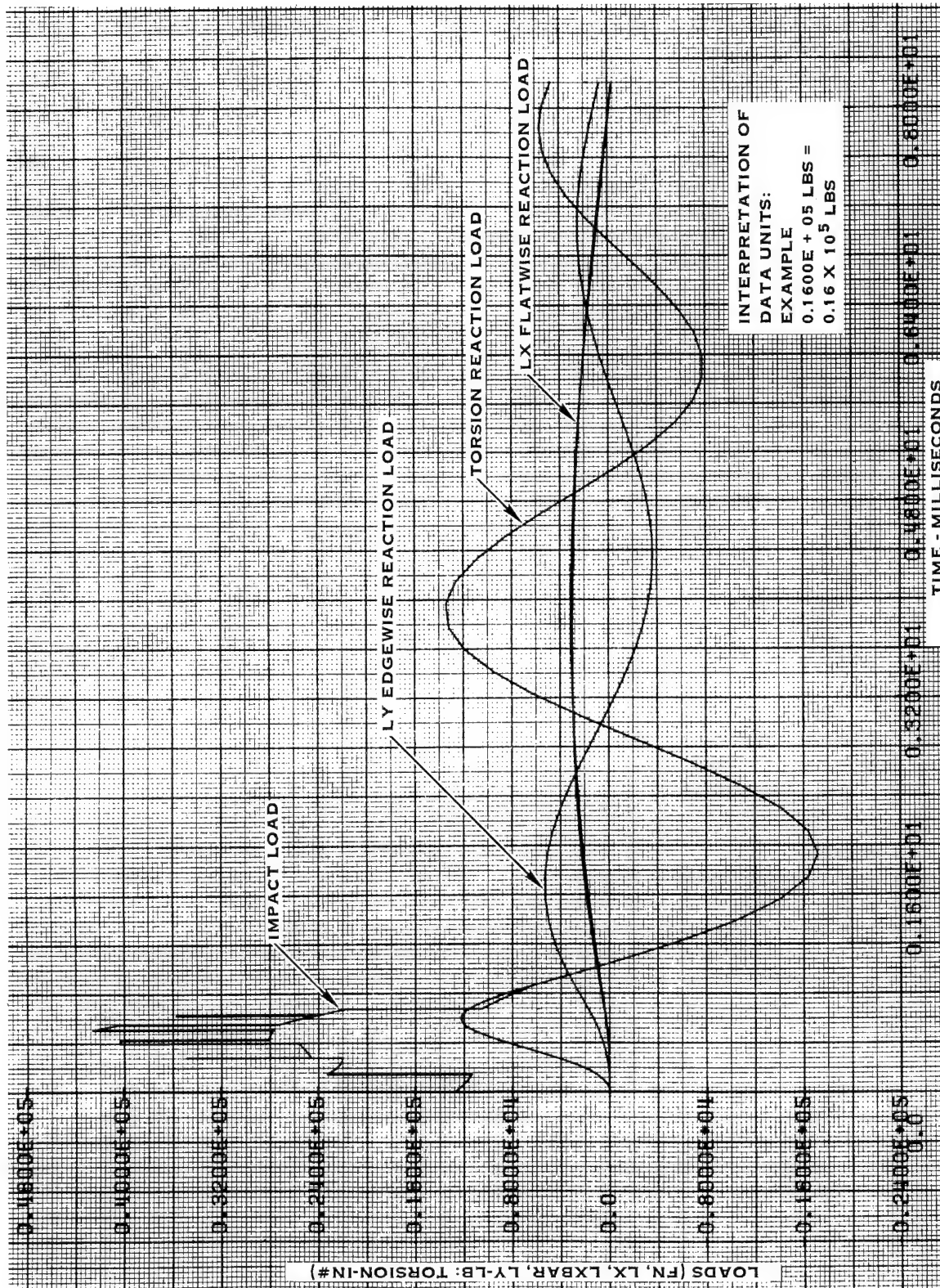* Blade reduction required to achieve target slice size.

FIGURE 14. FOD IMPACT BLADE LOAD TIME HISTORY AT IMPACT SITE
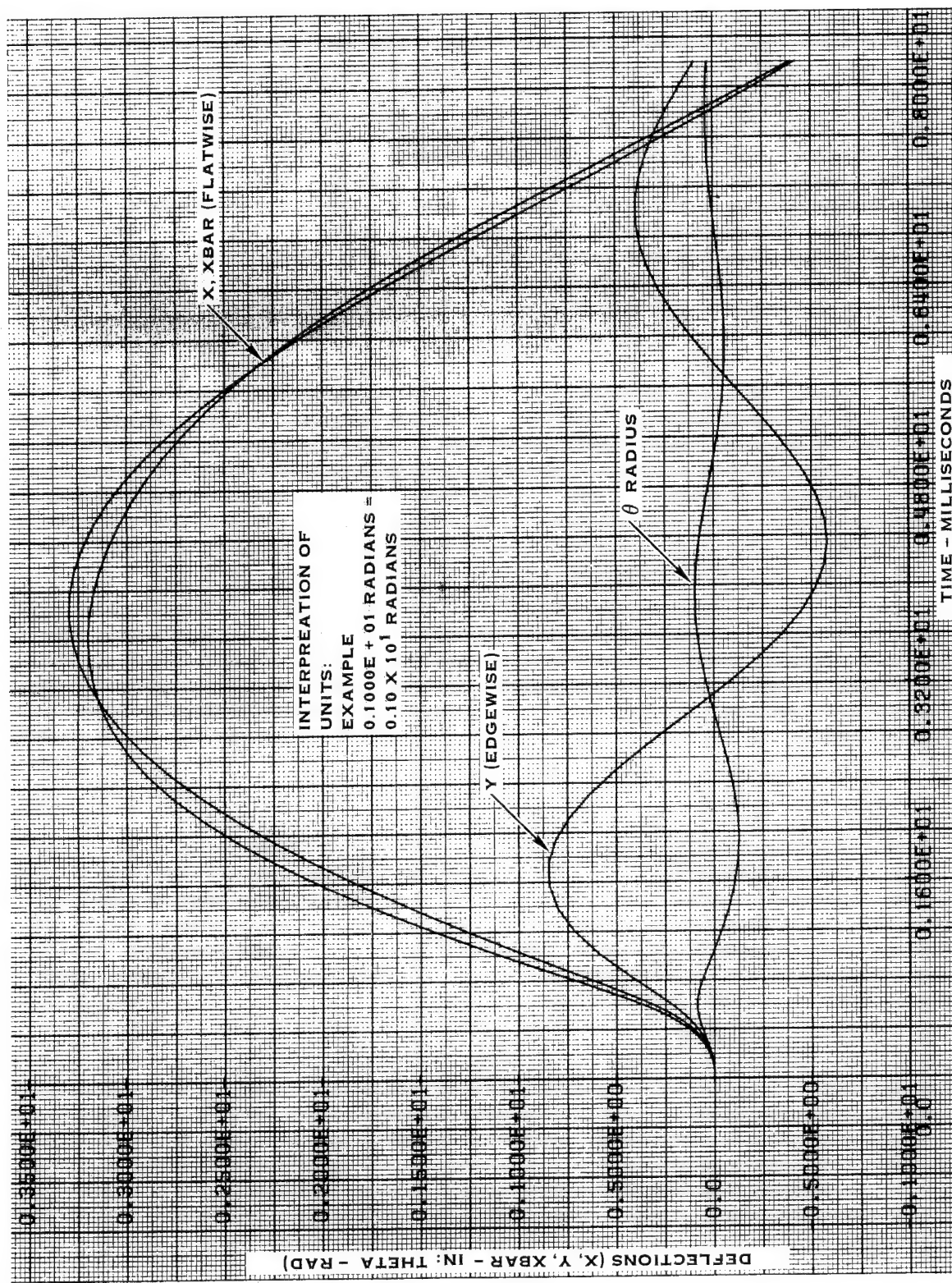
43

FIGURE 15. FOD IMPACT INDUCED BLADE DEFLECTION TIME HISTORY AT IMPACT SITE

44

FIGURE 16. FOD INDUCED BLADE FLATWISE BENDING STRESS TIME HISTORY

45
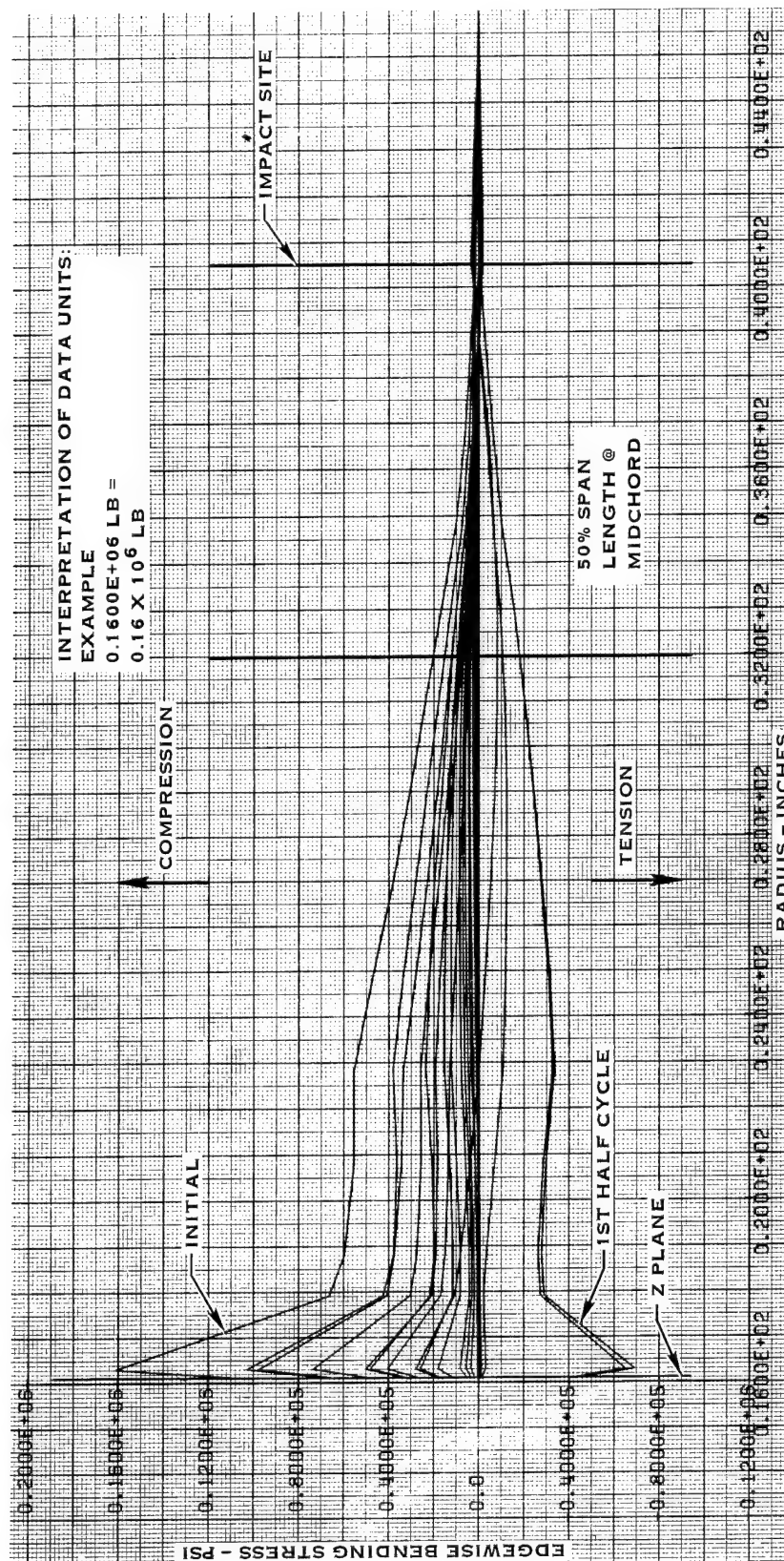
FIGURE 17. FOD INDUCED BLADE EDGEWISE BENDING STRESS TIME HISTORY

46

IDEALIZED SPAR RECTANGULAR CROSS SECTION
ILLUSTRATING STRESS/STRAIN THICKNESS WISE DIST.

$$a = \frac{E_P/E_e \cdot \sigma_y \cdot h}{\sigma_U + (E_P/E_e - 1)\sigma_y}$$

SECTOR 1 - ELASTIC STRAIN ENERGY

$$U_e = \frac{\sigma_y^2 W}{3 E_e}\left[a + h - a^3/h^2\right]$$

SECTOR 2 & 3 - PLASTIC STRAIN ENERGY

$$U_P = \frac{W(h-a)(\sigma_u - \sigma_y)}{E_P}\left[2\sigma_y + \frac{(\sigma_u - \sigma_y)}{3}\right]$$

STRAIN ENERGY CAPACITY @ 7.2×10^5 IN•LB ≫
BIRD IMPACT KINETIC ENERGY @ 4.7×10^4 IN•LB

BENDING STRESS DIST. OWING TO BIRD IMPACT
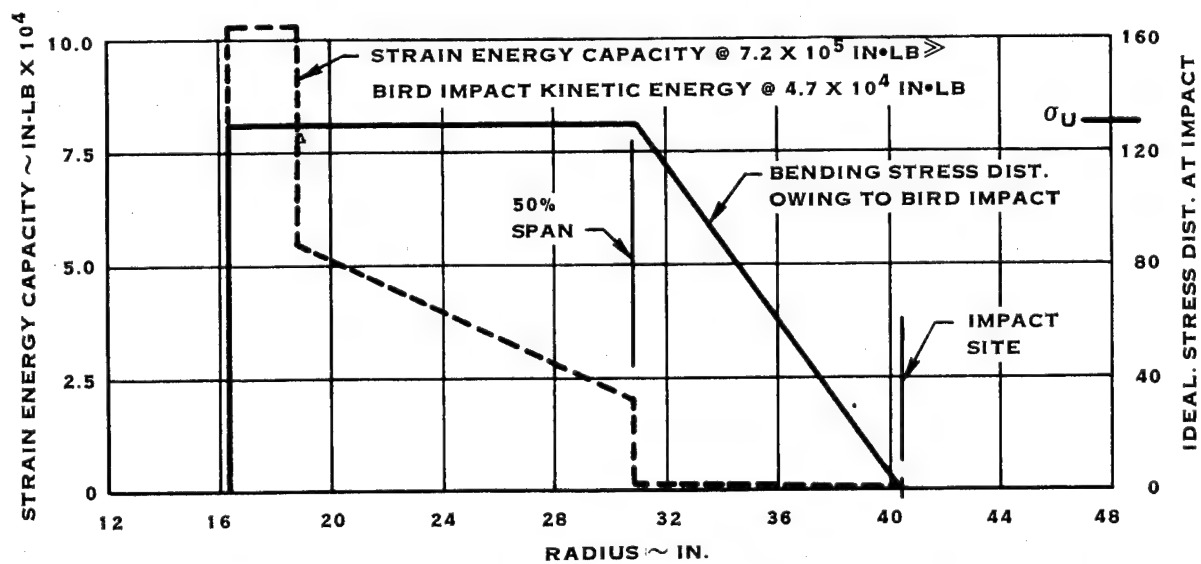
50% SPAN

IMPACT SITE

FIGURE 18. STRAIN ENERGY BLADE CAPACITY VRS KINETIC ENERGY OF
IMPACT WITH 1.5 LB BIRD SLICE AT 80% SPAN

47

3.1.3.5.2 Related FOD Test Experience

Hamilton Standard has acquired substantial experience in FOD testing of composite blades beginning with the boron epoxy shell/hollow steel spar JT9D blade. The large fan blade FOD experience evolved through a series of Q-Fan and QCSEE fan blade evolutionary changes culminating in the QCSEE fan blade with testing conducted under contract NAS3-17837. This blade which featured polyimide adhesive bonding of a 6Al-4V titanium sheath to a boron/aluminum shell which in turn was also adhesively attached to a solid titanium spar proved to be the most successful large composite blade FOD demonstration testing conducted to date. As part of this testing, stress measurements at various inboard blade stations were correlated with those predicted by the missile impact analysis.

The JT9D blade of this program draws the QCSEE experience but in addition adds features which should further enhance FOD impact tolerance. Chief among these features are diffusion bonding of sheath details and metal joining of the sheath to the shells.

A means of examining the projected success of the JT9D blade is provided by comparing its impact kinematics with those of the previously conducted QCSEE tests. Most significant in this data, as shown in Table IX are the normal impact momentum and kinetic energy. The JT9D impact event falls half way between the two QCSEE test conditions. However, the JT9D airfoil shape, as defined by the thickness/chord ratio, is approximately 84% the thickness of the QCSEE blade at a given chordwise location. This shape factor would tend to reduce the FOD resistance of the JT9D blade somewhat. The tangential or in-plane impact momentum and kinetic energy both, are substantially higher than that experienced in the QCSEE tests, however, this vector component is not considered the principal cause of catastropic blade damage owing to the high blade stiffness in an edgewise plane.

Illustrative of the QCSEE impact tests are Figures 19 and 20. The 0.681 kg slice event with a 22.2 degree impact angle survived with but a 1.4% blade weight loss. The 0.763 kg slice event at 32.3 degree impact angle survived with a 3% blade weight loss. The leading edge damage to that blade is representative of what should be expected given an impact event of this degree of severity. The trailing edge damage, which is judged to be due to torsional reactionary loads causing high local shear and peel stresses, may be eliminated through a combination of changes in the shell ply orientations and improvements afforded by metal bond joint formation.

As a final point in this analysis, the spar shell composite blade of QCSEE-type construction did survive impact events judged to be two to three time as severe as those to be experienced in the large bird impact of a fully bladed rotor operating within the engine flight envelope. The JT9D blade design which was evaluated at a slice mass roughly three times that possible in its rotor system is considered to have a similar FOD impact resistance to that demonstrated in the QCSEE program.

TABLE IX. KINEMATICS OF THE JT9D ANALYTICAL CONDITION COMPARED WITH TWO QCSEE TEST CONDITIONS

	JT9D SLTO Impact Anal.		QCSEE SLTO FOD Sym. Test		QCSEE Climb FOD Sym. Test	
	SI Units	Eng. Units	SI Units	Eng. Units	SI Units	Eng. Units
Bird Characteristics						
Weight	1.36 kg	3 lb	1.33 kg $ Avg	2.94 lb	1.126 kg	2.48 lb
Density	0.68 gms/cc	42.5 lbs/ft^3	UNK #	UNK #	UNK #	UNK #
Dia/Length Ratio	2:1	2:1	App 2:1	App 2:1	App 2:1	App 2:1
Blade Parameters						
Percent Span	80	80	80	80	80	80
ch Angle	0.48 Rad	27.5 Deg	0.56 Rad	32.3 Deg	0.39 Rad	22 Deg
Blades Per Disk	10 *	10 *	1	1	1	1
Thick/Chord Ratio	0.032	0.032	0.038	0.038	0.38	0.038
LE Radius	0.61 mm	0.024 in.	0.060 mm	0.0235	0.60 mm	0.0235 in.
Impact Conditions						
Blade Tangenial Vel.	393 m/sec	1250 ft/sec	253 m/sec	830 ft/sec	253 m/sec	830 ft/sec
Flight Velocity	232 km/hr	125 kt	22 km/hr	12 kt	22 km/hr	12 kt
Result. Impact Vel.	398 m/sec	1307 ft/sec	253 m/sec	830 ft/sec	253	830
Impact Angle	0.318 Rad.	18.2 Deg.	0.56 Rad.	32.3 Deg.	0.39 Rad.	22.2 Deg.
Slice Mass	0.657 kg	1.45 lb	0.763 Avg.	1.68 lb	0.681	1.50 lb
Normal Impact Mom.	81.7 N·sec	18.4 lb$_f$·sec	103.2 N·sec	23.2 lbf·sec	65.1 N·sec	14.6 lb$_f$·sec
Normal Impact K.E.	5084 N·M	3750 lb$_f$·ft	6973 N·M	5143 lb$_f$·ft	3112 N·M	2295
Tangential Impact Mom	248.6 N·sec	55.9 lb$_f$·sec	163.2 N·sec	36.7 lb$_f$·sec	159.5 N·sec	35.9 lb$_f$·sec
Tangential Impact K.E.	4.70 x 10^4 N·M	3.47 x 10^4 lb$_f$·ft	1.74 x 10^4 N·M	1.29 x 10^4 lb$_f$·ft	1.87 x 10^4 N·M	1.38 x 10^4 lb$_f$·ft

* Adj. from 30 to meet slice mass criteria
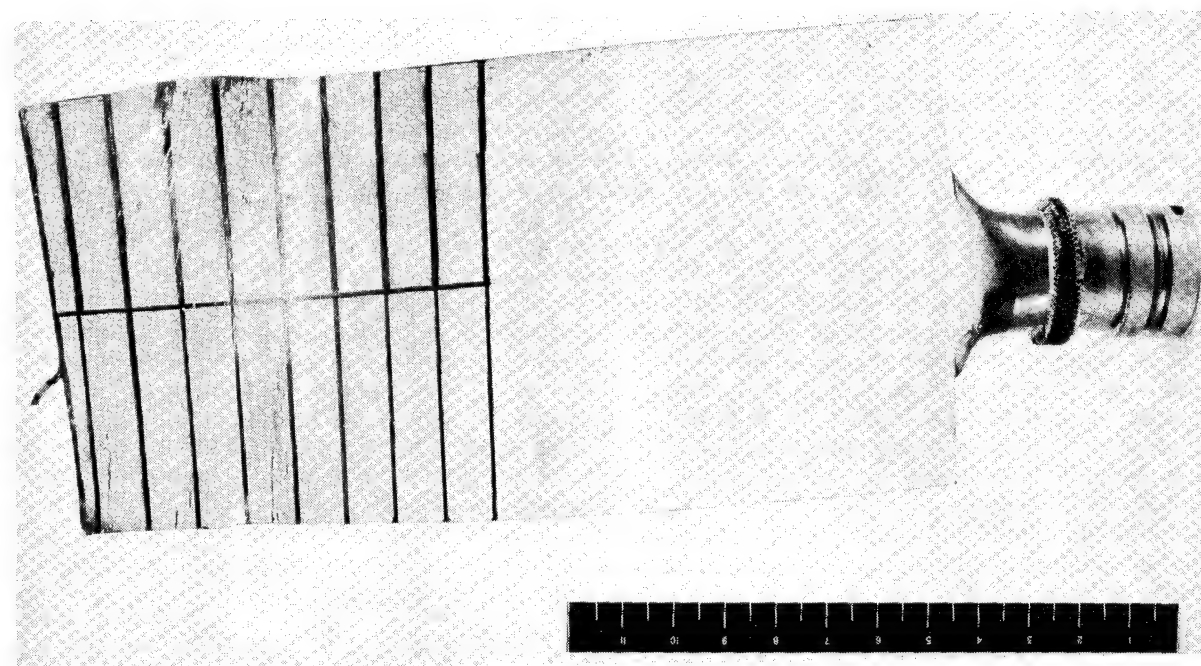
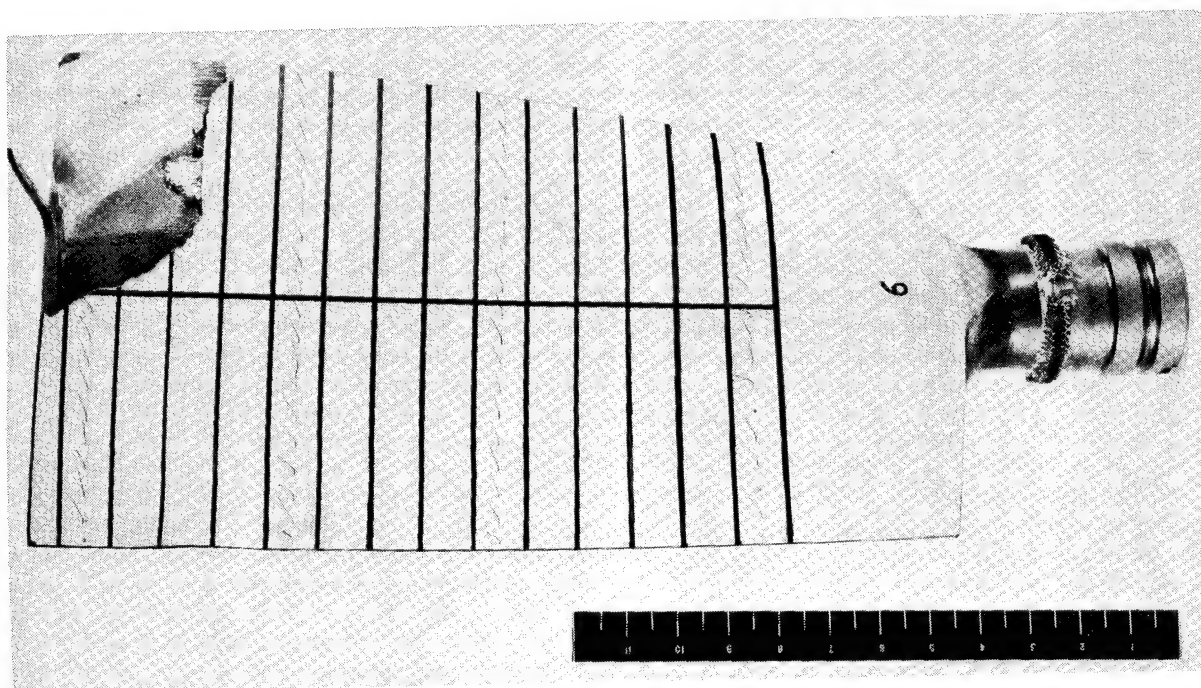\# Tests included actual birds

\$ Avg. of 3 impact events

FIGURE 19. QCSEE BLADE REAL BIRD IMPACT TEST WITH .681 KG IMPACT SLICE
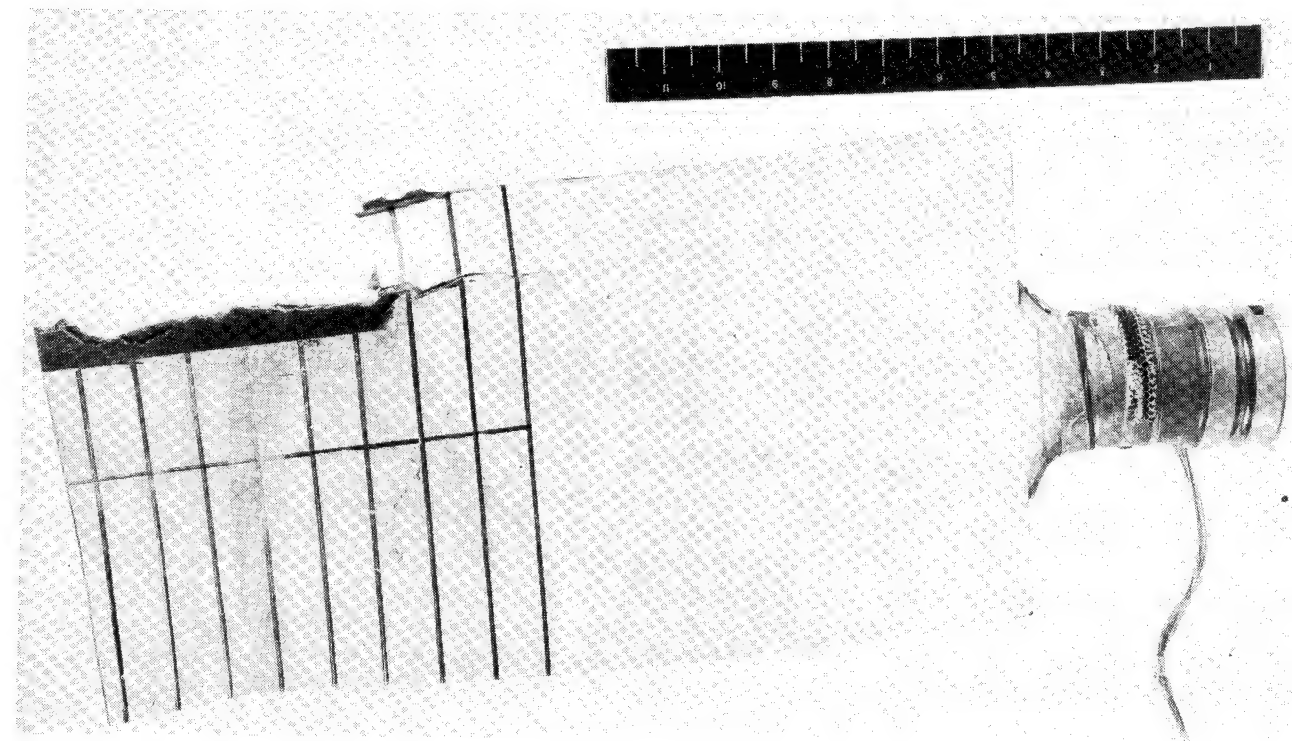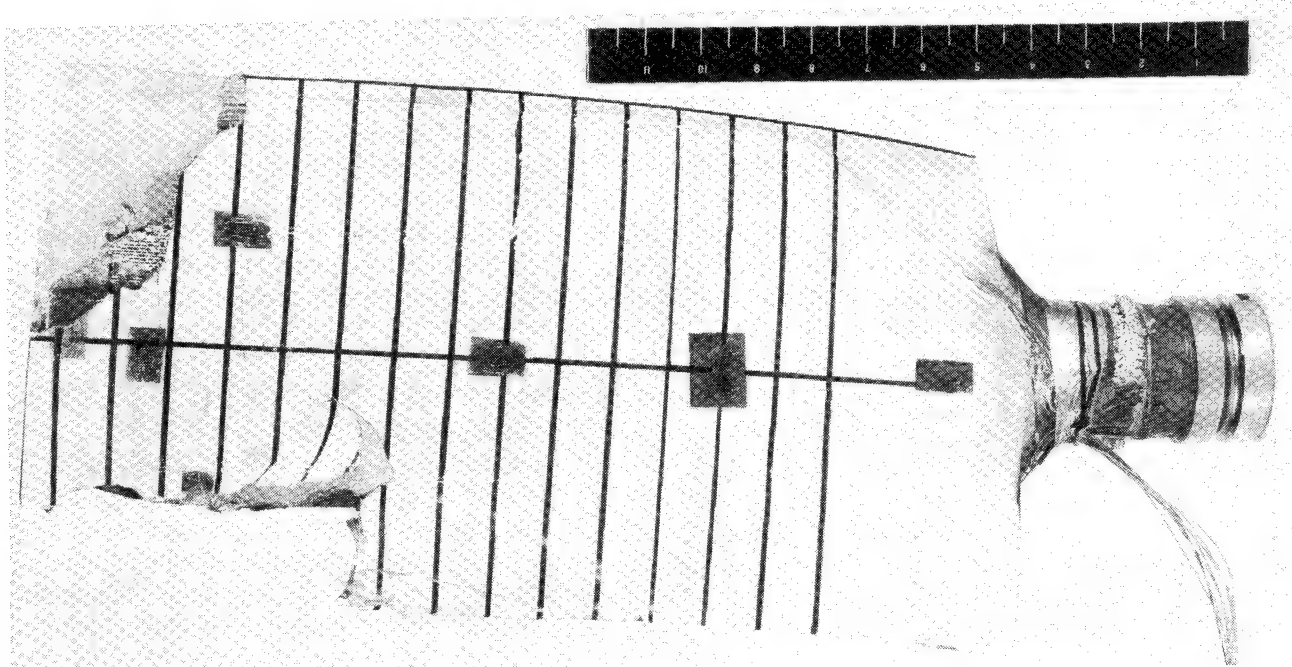AND 22.2 DEGREE IMPACT ANGLE

FIGURE 20. QCSEE BLADE SIMULATED BIRD IMPACT TEST WITH .763 KG IMPACT SLICE AND 32.3 DEGREE IMPACT ANGLE

3.1.4 Design Summary

The purpose of the Design Task, which included selection of an existing applicable blade design; conduction of preliminary design studies leading to a selection of two alternate blade designs; and the refinement of the two selected designs to the point of assessment of major structural considerations, was accomplished. The selected design model was an existing joint Pratt & Whitney and Hamilton Standard JT9D composite 1st stage fan blade with a 3.0 aspect ratio. With the external geometry established, the preliminary design utilized basic beam analysis in the calculations performed to meet preliminary structural and weight objectives. The optimum design which featured a hollow titanium spar was projected to reduce the first stage rotor weight by 39%. The ongoing industry efforts at superplastic forming titanium shapes makes this design a potential future approach for fan blades in high by-pass ratio turbofan engines. Owing to a current shortfall of proven titanium forming technology the prudent choice was made of the lower risk light weight titanium spar blade. This blade design which reduces the first stage rotor system weight by 14% utilizes available manufacturing technology. The two detail designs of this configuration consists of two aluminum alloy choices, AA6061 & AA1100, for the composite matrix. This variant provides tradeoffs of transverse strength for impact resistance. Structural analysis conducted included calculation of static bending and centrifugal stresses, blade dynamic response, shell tab ending stress distribution and FOD impact assessment. This latter analysis considered the structural effect of a bird impact slice of 0.681 kg. (1.5 lb) from a 1.362 kg. (3 lb) bird at a takeoff flight condition. Based on these analyses of the blade, the design met the criteria for a successful configuration and is considered adequate as a foundation for a full scale development program was established.

3.2 TASK II - PROCESS DEVELOPMENT

The dual purpose of the program was, in addition to blade design, process development of key processing parameters and/or design features leading to demonstration pressings of simulated airfoils. The following key features were selected for process development:

- Metal joining for structural joints.

- Titanium honeycomb evaluation as a filler material.

- Evaluation of large diameter boron/aluminum matrix materials as candidate shell materials.

In keeping with the process goals, the following material tests were selected for test evaluation:

- Basic strength, stiffness and elongation properties of 0.2mm (0.008 in) boron fiber in aluminum matrixes of AA1100 and 6061 alloys.

- Shear strength properties of bond joints formed between 6Al-4V titanium and the candidate boron/aluminum composite materials with both AA1100 and 6061 aluminum alloy foils.

- Titanium honeycomb compression strength and honeycomb bond strength when diffusion bonded to facing materials simulating the blade application.

With an end goal of producing demonstration hardware, the choice was made to utilize the avaliable tooling from the Hamilton Standard QCSEE Variable Pitch Blade Program conducted under Contract NAS-17837. This airfoil is of similar size and shape to the design blade with the exception of the circular shaft root retention which replaces a conventional dovetail attachment. It was judged to be a good compromise shape to use for demonstration of key process design features.

3.2.1 Simulated Airfoil Pressing Description

The QCSEE blade (HS drawing P/N 759043) featured a blade construction adhesively assembled after shell manufacture. The high temperature dies, intended for shell manufacture only, required modifications to allow for the addition of spar to shell and sheath to shell joining operations at metal bonding temperatures. The basic

configuration of the blade is given in Figure 21. The basic construction of the blade has the following features:

- A solid 6A1-4V titanium spar

- 0.2mm (0.008 in) boron/aluminum columnar composite plies utilizing either AA1100 or AA6061 aluminum matrixes.

- Shells made from seven boron/aluminum layers aligned at 90°, ±45°, and ±20° to the blade 5° airfoil sweep axis and bonded to a 0.25 mm (0.010 inch) 6A1-4V titanium erosion protection outer skin. See Figure 22.

- 3A1-2.5V titanium honeycomb of 128 kg/m^3 (8#/ft^3) density used to fill the spar fore and aft radial cavities. This density was selected on the basis of availability. See Figure 23.

- AA6061 aluminum alloy for metal joining spar to shells and sheath to shells.

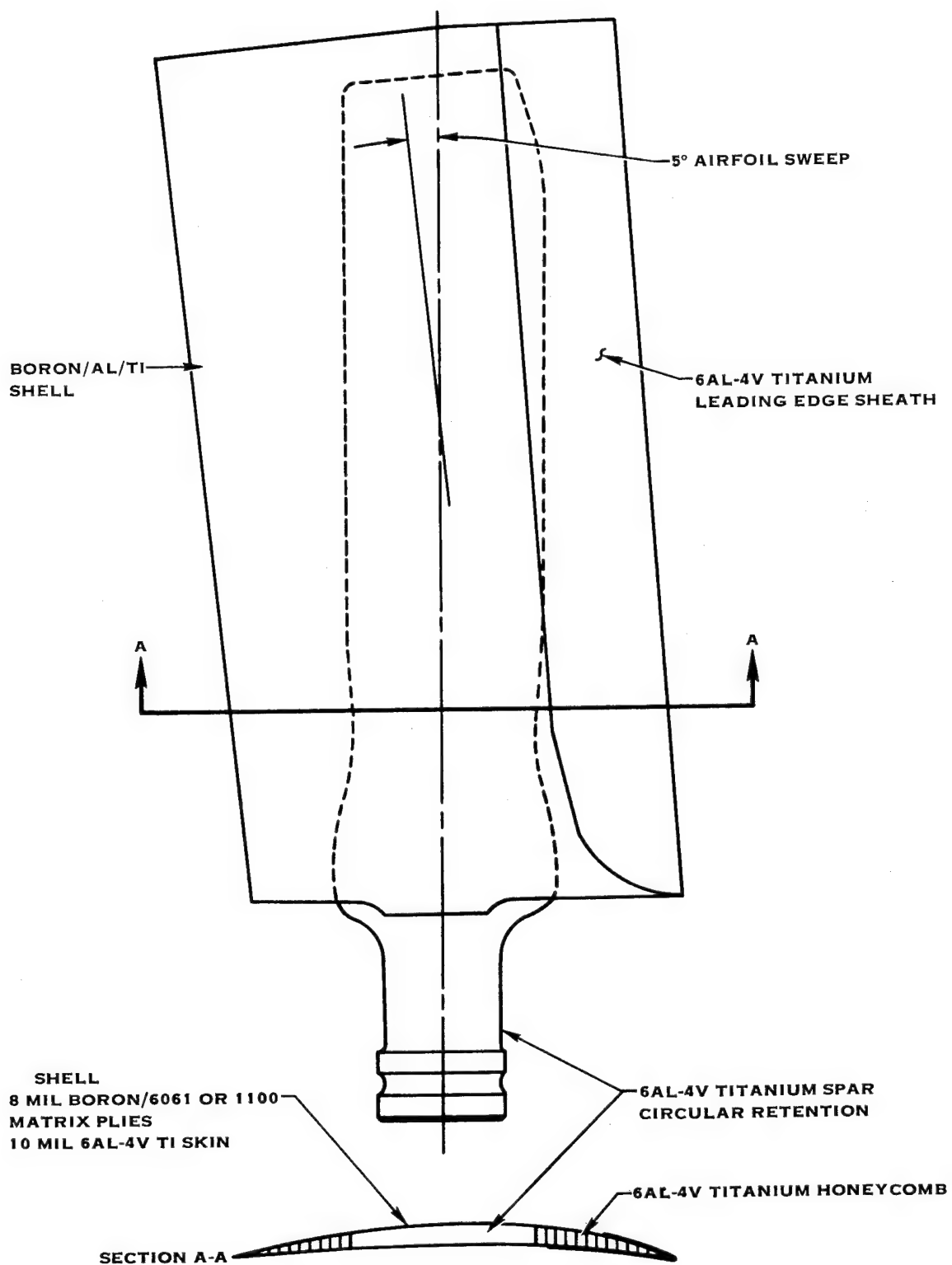- Three piece 6A1-4V titanium sheath aluminum bonded assembly. See Figure 24.

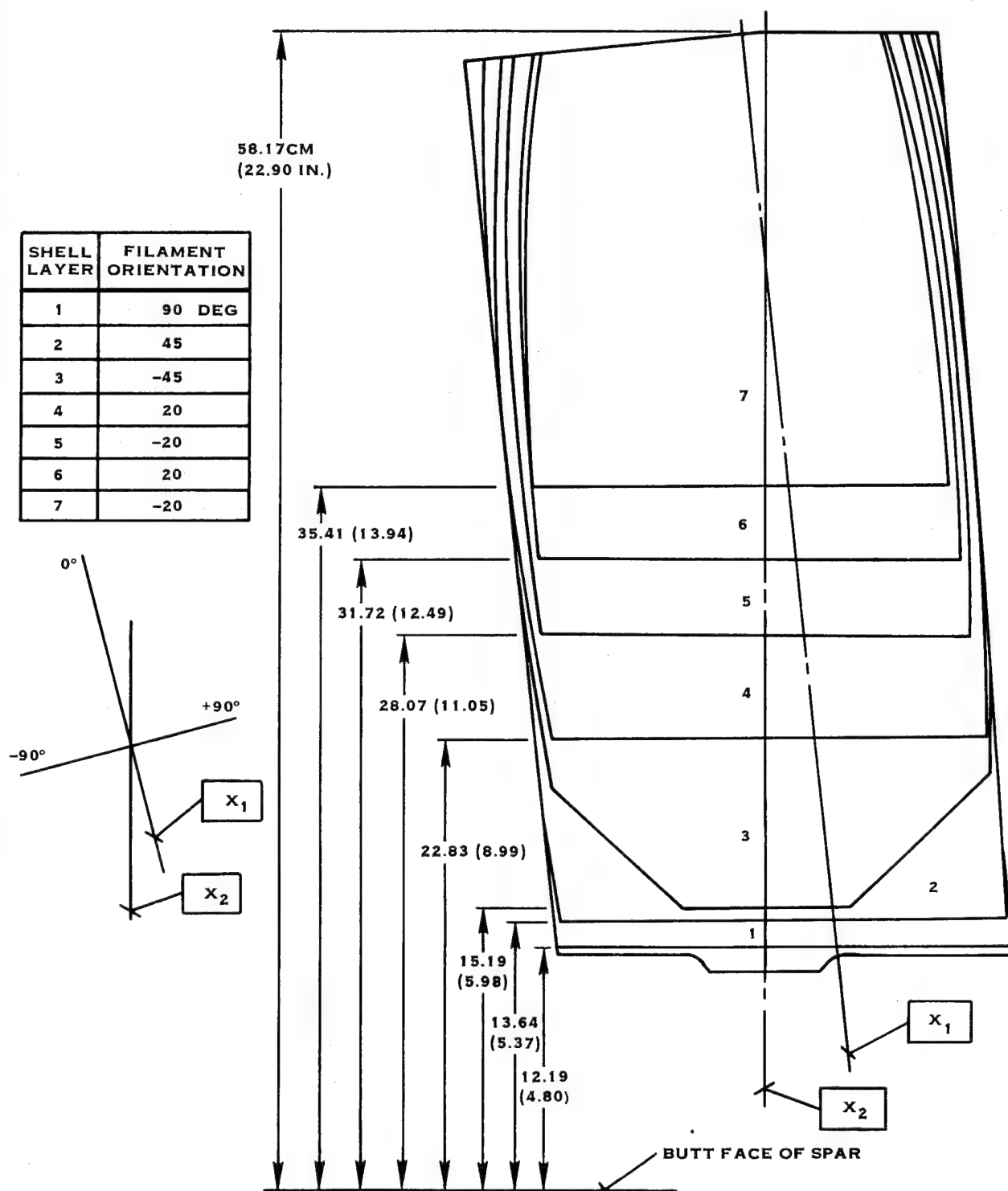**FIGURE 21. SCHEMATIC OF DEMONSTRATION AIRFOIL PRESSING CONSTRUCTION**

56
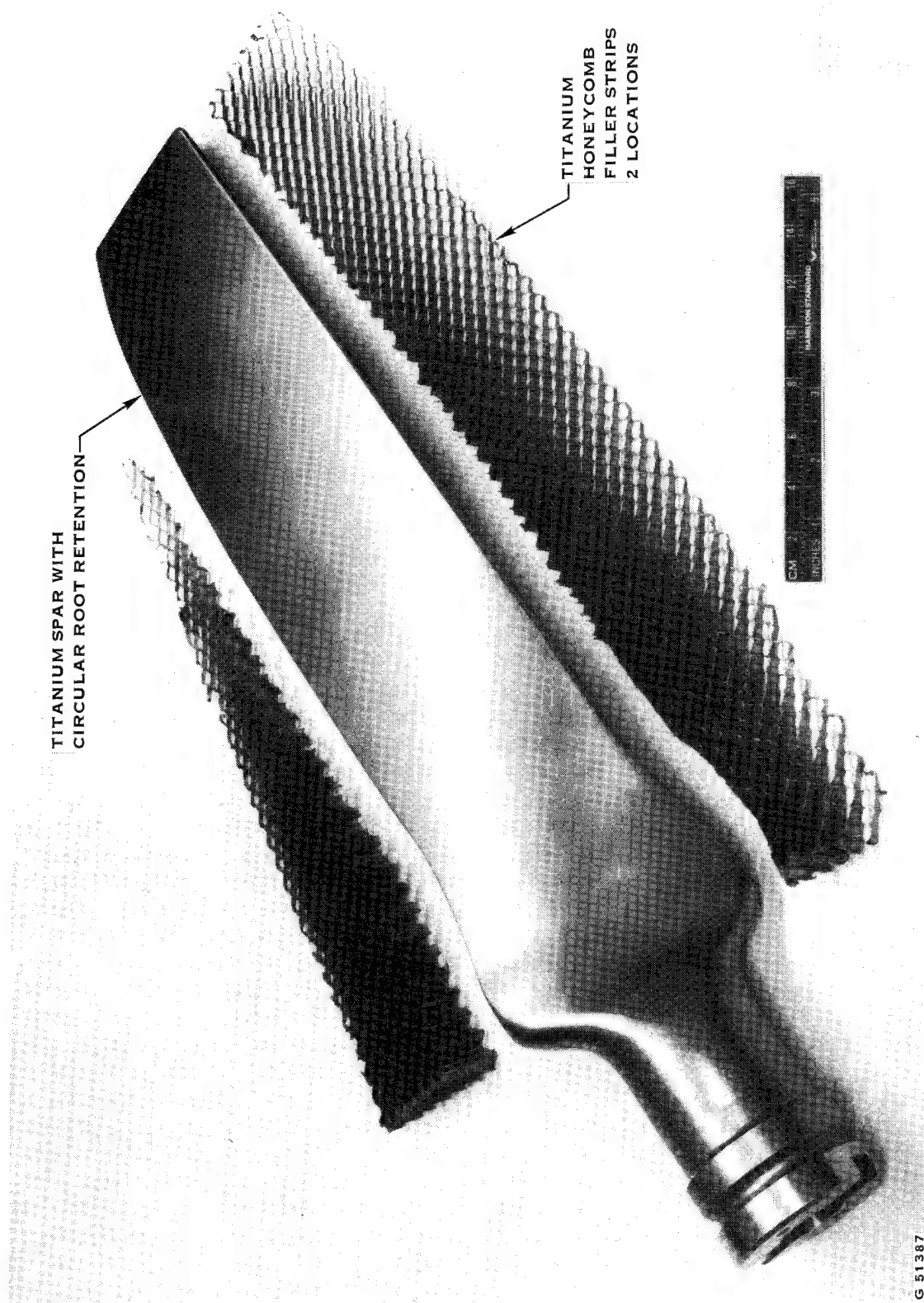
FIGURE 22. DEMONSTRATION AIRFOIL SHELL LAYUP

57

TITANIUM
HONEYCOMB
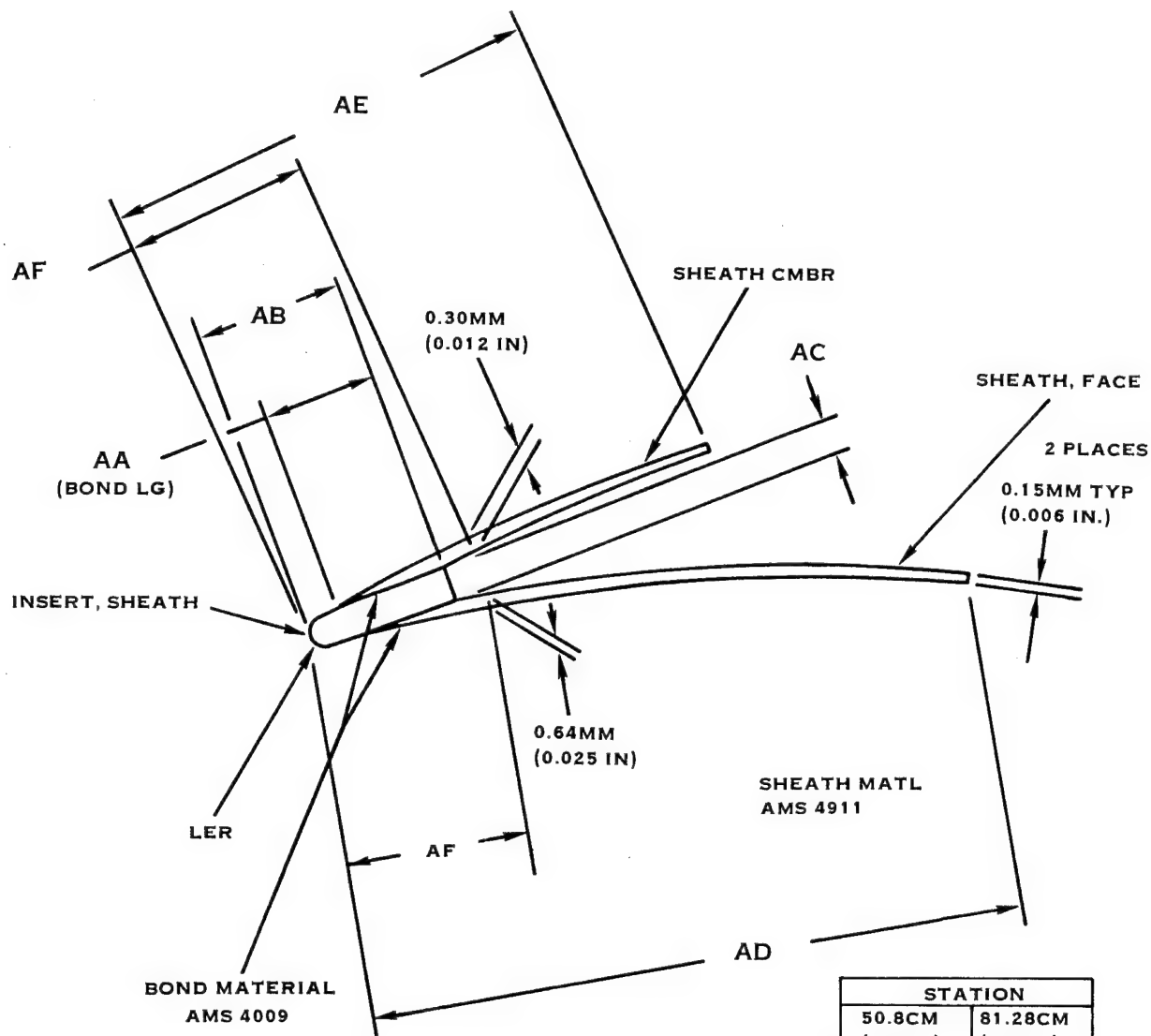FILLER STRIPS
2 LOCATIONS

TITANIUM SPAR WITH
CIRCULAR ROOT RETENTION

G 51387

FIGURE 23. DETAIL CORE PARTS FOR DEMONSTRATION AIRFOIL PRESSING

58

	STATION	
	50.8CM (20 IN.)	81.28CM (32 IN.)
AA	2.54MM (0.100 IN)	6.53MM (0.257 IN)
AB	3.58 (0.141)	6.76 (0.266)
AC	1.37 (0.054)	1.01 (0.040)
AD	61.19 (2.409)	61.72 (2.430)
AE	44.22 (1.741)	39.01 (1.536)
AF	4.06 (0.160)	8.13 (0.320)
LGR	0.57 (0.0225)	0.60 (0.0235)

FIGURE 24. LEADING EDGE SHEATH GEOMETRY FOR DEMONSTRATION AIRFOIL PRESSING

3.2.2 Metal Bonding Facility

3.2.2.1 Die Modification

The tooling utilized on this program was supplied rent free from the NASA QCSEE FOD Demo Blade Program conducted at Hamilton Standard. That particular blade had a similar boron/aluminum shell to the demonstration pressings, however, joining of shells to the spar and the sheath to the shells was accomplished by using a polyimide adhesive. Thus owing to processing temperatures, die material selection for the QCSEE program was tool steel for shell fabrication and aluminum alloy for subsequent adhesive bonding of shells to spar. With the necessity to use the tool steel dies for the metal bonding trials a modification was necessary to accommodate the spar's circular shank. Figure 25 shows the before and after modification of the die depicting the necessary circular relief cuts and spar location fixturing added to allow for shell to spar metal joining.

3.2.2.2 Vacuum Chamber Fabrication

The QCSEE program shell consolidation utilized a stainless steel vacuum bag along with a heated chamber in which a press provided consolidation pressure. With a need to optimize the metal bond joint between the titanium spar and the boron/aluminum shell, the judgment was made to utilize a retort chamber to provide the high vacuum condition required. To accommodate the blade geometry, a larger chamber than available was required. A company funded effort to design and construct the necessary retort was performed and is shown in Figure 26. Both shell consolidation and blade assembly were conducted in this new facility which demonstrated during usage a 2×10^{-2} torr vacuum capability which was well below the 1×10^{-1} torr minimum level deemed necessary for contamination free bonding.

60

DIFF. BOND
DIES AS
ORIGINALLY
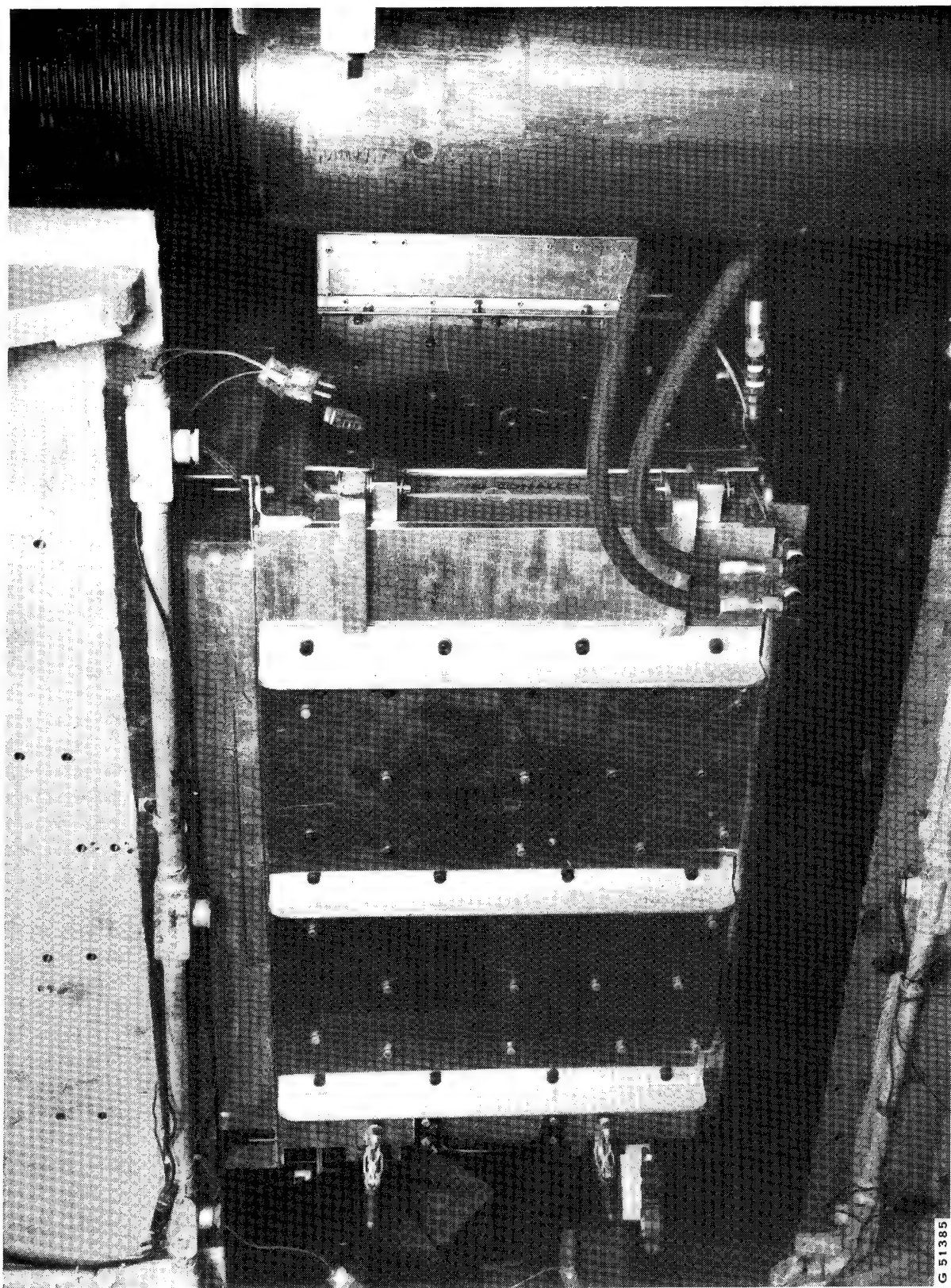MANUFACTURED
FOR SHELL
PRESSINGS ONLY

G 51384

BEFORE
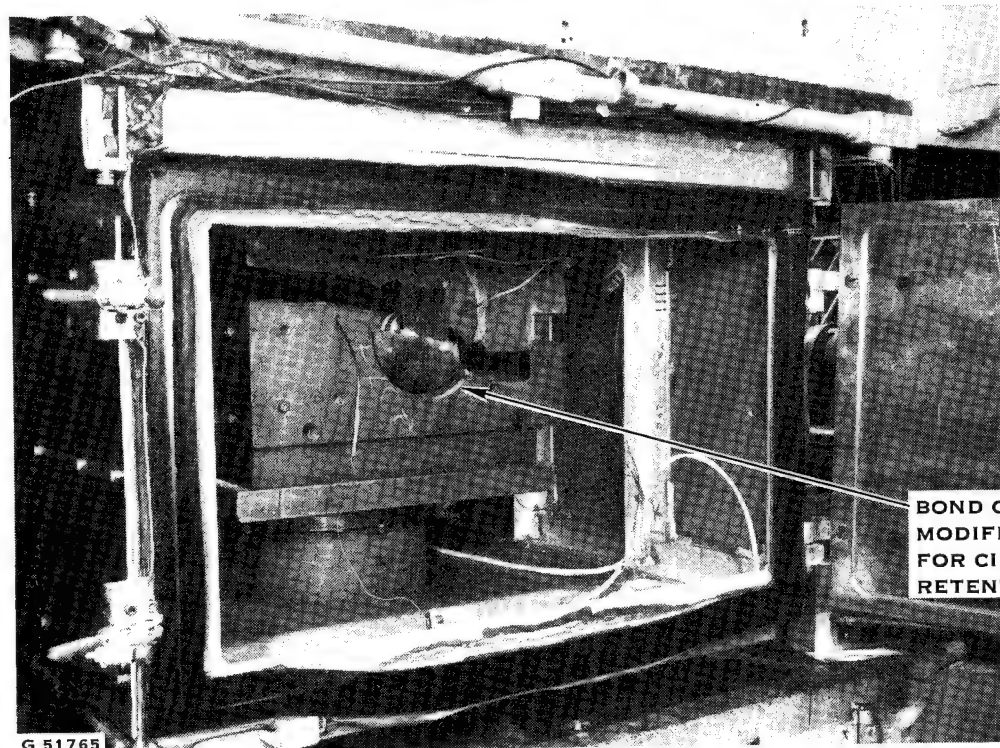
BOND CAVITY
MODIFICATION
FOR CIRCULAR
RETENTION SPAR

G 51765

AFTER

FIGURE 25. SHELL DIFFUSION BONDING DIES MODIFIED FOR METAL JOINING
OF DEMONSTRATION AIRFOILS

FIGURE 26. VACUUM RETORT FABRICATED FOR DEMONSTRATION AIRFOIL PRESSING
SHELL CONSOLIDATION & METAL BONDING

G 51385

3.2.3 Materials & Process Verification

3.2.3.1 Boron/Aluminum Mechanical Property Evaluation

With considerable data previously generated on large diameter boron fiber rein-
forced aluminum matrix composite panel material, Reference 2, the judgement was
made only to verify that the material to be used possessed typical properties. The
previous mechanical property study evaluated the same 0.2 mm (0.008 inch) diameter
fiber produced by both Composite Materials Corporation (CMC) and AVCO in both
caddidate aluminum matrix materials. The properties of ultimate tensile strength,
tensile modulus and percent strain at failure were chosen for evaluation in both the
fiber longitudinal and transverse directions. Post test macro examination of the
tensile specimens also was planned so as to verify quality of consolidation. With the
need to minimize the potential for titanium surface contamination, a vacuum atmos-
phere was selected for the bonding of all material for testing in addition to the trial
blade fabrication efforts.

Materials selected for use in this program consisted of boron fibers produced
by CMC and made into tape by Union Carbide. The tape consisted of 0.05 mm
(0.002 inch) aluminum foil backing with an aluminum plasma spray adhering the
0.2 mm boron fiber to the backing. Both candidate matrix systems of AA1100 and
AA6061 aluminum alloys were used to produce the two desired composite materials.

To acquire the selected data, three panels of 11.4 cm (4.5 in.) length by 8.9 cm
(3.5 in.) width were consolidated from six parallel boron/aluminum layers. Consoli-
dation conditions were performed to Hamilton Standard processing specifications
whose principal parameters are given below:

| | Alloy System | |
	AA1100	AA6061
Temperature	540°C (1005°F)	546°C (1015°F)
Pressure	37.9 MPa (5500 psi)	37.9 MPa (5500 psi)
Vacuum	10^{-1} torr	10^{-1} torr
Time On Condition	15 Minutes	10 Minutes

A total of fourteen tensile coupons of 1.4 mm x 6.35 mm cross sectional size were cut from the aforementioned panels producing the following specimen mix of fiber orientation and matrix alloys:

	AA1100	AA6061
Longitudinal	4	2
Transverse	5	3

The tests were performed following a proposed ASTM specification entitled "Standard Method of Test for Tensile Properties of Fiber Reinforced Metal Matrix Composites". Table X gives all the results obtained from these tests along with average values for each property and matrix alloy. The columns identified as normalized adjusts the test values to a 50% fiber volume content so as to enable direct comparison with published data. The normalized average data is compared with published data in Table XI.

Examination of the new test data in light of both the total historic data base and the data scatter incurred in substantive sample lots (30 samples required for a meaningful standard deviation calculation) indicates that the new data is well within a projected typical one standard deviation band. By using the ratio of one standard deviation to the mean value of the 6061 matrix/CMC fiber/air bond cycle data a variance of ± 10% for 0° orientation and ± 23% for 90° orientation is generated. Taking a weighted average strength value without regard to fiber source or process method and applying a typical variance yields the expected band for the 68.27% data population base (1 standard deviation). Given below is the comparison of new test data to the weighted average data and the expected data scatter band which illustrates that the test data is typical data.

Matrix	Orientation	Weighted Average Strength	Weight Average Strength & Variance	Average Strength New Data
1100	0	1197 MPa	1077 – 1317 MPa	1110 MPa
	90	51	39 – 63	61
6061	0	1352	1217 – 1487	1255
	90	124	95 – 153	162

Only in the case of the 90° orientation AA6061 alloy is the band exceeded and with appreciation of the fact that the matrix carries the load at this orientation and that the value exceeds the upper limit, it is judged to represent satisfactory material. With the small sampling of tensile modulus data both in the new data and in the historic data base a rigorous evaluation of data quality cannot be made. Engineering judgement is made that although lower in tensile modulus in the zero degree orientation, the value is within 10% of the weighted average value (without regard to fiber source and process method) of the historic data base and thus is acceptable. In similar manner the 90° orientation tensile modulus is also judged to represent satisfactory material.

Microstructural work was performed on all three test panels (#1331, 1332 and 1334). Figures 27 and 28 illustrate structures of tensile remnants from the two 0.2 mm boron/1100 panels (#1331 and 1332). It can be seen that both panels were fully compacted and were characterized by a generally uniform fiber distribution. Figure 29 shows structures from the 0.2 mm boron/6061 panel (#1334). This panel was fully compacted and exhibited uniform fiber distribution.

TABLE X. BORON/ALUMINUM COMPOSITE PANEL TENSILE PROPERTIES

| Panel Composition	Panel No.	Spec. No.	Fiber Orient.	UTS – MPa/(KSI) Meas.	UTS – MPa/(KSI) Normal. *	Ten. Mod. –GPa/(MSI) Meas.	Ten. Mod. –GPa/(MSI) Normal. *	Strain @ Failure μMM/MM
0.2 mm Boron/AA1100 Aluminum CMC Fiber in a UC Tape	1331	L1	0°	1138 (165)	1131 (164)	--	--	--
		L2		1207 (175)	1193 (173)	287 (27.1)	185 (26.8)	6300
	1332	L1		1096 (159)	1083 (157)	--	--	--
		L2		1055 (153)	1041 (151)	187 (27.1)	184 (26.7)	5400
		$\overline{X}$		1124 (163)	1110 (161)	187 (27.1)	185 (26.8)	5800
	1331	T1	90	60 (8.7)	59 (8.6)	--	--	--
		T2		57 (8.3)	57 (8.2)	116 (16.8)	114 (16.6)	620
		T3		68 (9.8)	67 (9.7)	--	--	--
0.2 mm Boron/AA1100 Aluminum CMS Fiber in a UC Tape (Continued)	1332	T1		52 (7.6)	52 (7.6)	--	--	--
		T2		71 (10.3)	70 (10.1)	148 (21.4)	145 (21.0)	1100
		$\overline{X}$		61 (8.9)	61 (8.8)	132 (19.1)	130 (18.8)	860
0.2 mm Boron/AA6061 Aluminum CMC Fiber in a UC Tape	1334	L1	0	1138 (165)		--	--	--
		L2		1489 (216)		211 (30.7)	204 (29.6)	7900
		$\overline{X}$		1310 (190)	1255 (182)	211 (30.7)	204 (29.6)	7900
		T1	90	166 (24.1)		--	--	--
		T2		170 (24.7)		134 (19.4)	130 (18.8)	1600
0.2 mm Boron/AA6061 Aluminum CMC Fiber in a UC Tape (Continued)		T3		161 (23.4)		--	--	--
		$\overline{X}$		166 (24.1)	162 (23.5)	134 (19.4)	130 (18.8)	1600

$$* \quad \frac{X^V/_o}{50^V/_o} = \frac{UTS\ (X^V/_o)}{UTS\ (50^V/_o)} = \frac{ET\ (X^V/_o)}{ET\ (50^V/_o)} \quad \text{With fiber volume } 40 < x < 60\ ^V/_o$$

66

TABLE XI. BORON/ALUMINUM TENSILE PROPERTIES COMPARED WITH HAMILTON STANDARD DATA BASE

| Panel Composition	Program	Fiber Source	Bond Cycle	0° Fiber Direction					90° Fiber Direction			
				No. Spec.	UTS MPa/(KSI)	No. Spec.	Ten. Mod. GPa/(MSI)	No. Spec.	UTS MPa/(KSI)	No. Spec.	Ten. Mod. GPa/(MSI)	
0.2 mm Boron/ AA1100 Aluminum	NASA	CMC	Q/V	4	1110 (161)	2	187 (27.1)	5	61 (8.8)	2	130 (18.8)	
	AFML*	CMC	AIR	4	1138 (165)	3	220 (31.9)	3	54 (7.9)	3	107 (15.5)	
	AFML*	AVCO	AIR	4	1255 (182)	4	201 (29.1)	4	49 (7.1)	2	96 (13.9)	
0.2 mm Boron/ AA6061 Aluminum	NASA	CMC	Q/V	2	1255 (182)	1	204 (29.6)	3	162 (23.5)	1	130 (18.8)	
	AFML*	CMC	AIR	49	1351 (196)	3	240 (34.8)	41	119 (17.2)	2	123 (17.9)	
	AFML*	AVCO	AIR	4	1379 (200)	4	239 (34.7)	4	151 (21.9)	4	143 (20.7)	
	AFML*	CMC	VACUUM	10	1372 (199)	-	--	16	118 (17.1)	-	--	
	AFML*	CMC	Q/V	4	1289 (187)	1	219 (31.7)	4	180 (26.1)	4	141 (20.5)	

All Properties Normalized For 50 $^V/_o$ Fiber Content

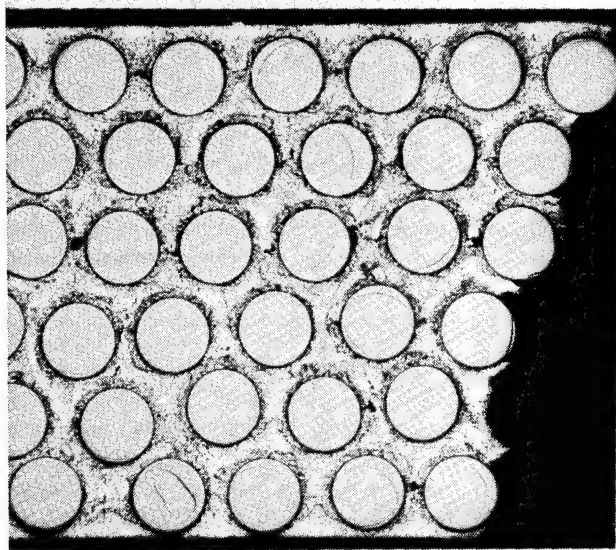* Reference 2, See Section 6.0.
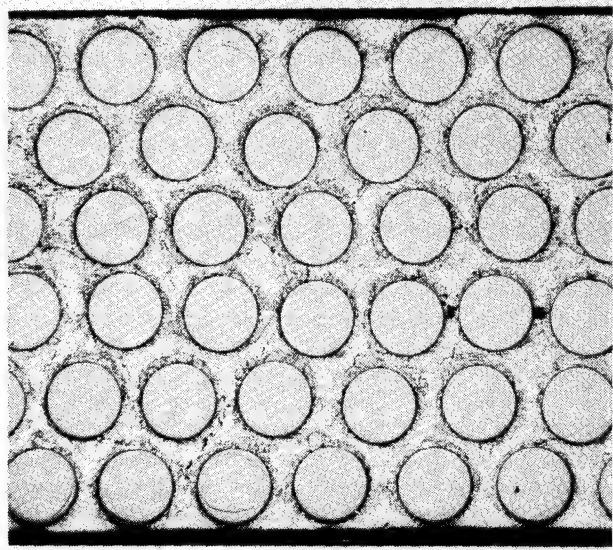
67
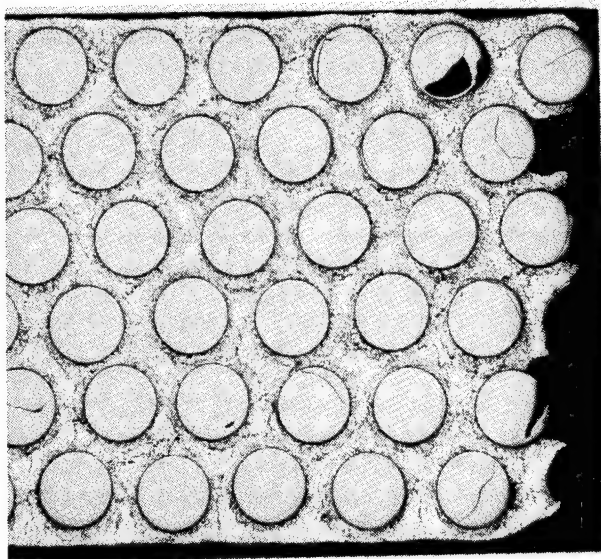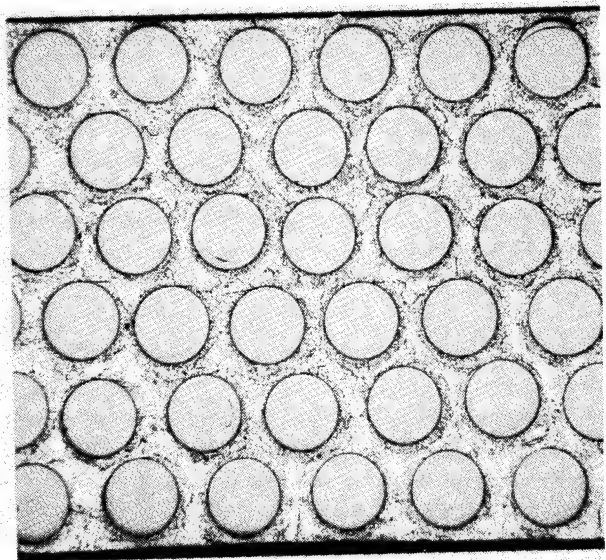
Fracture
50X

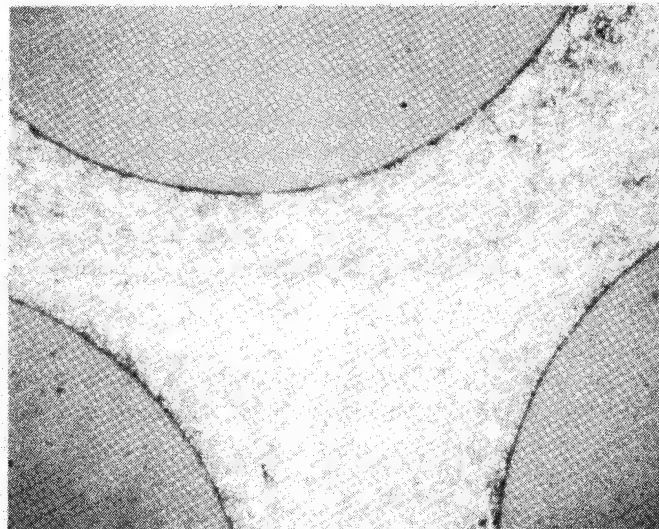Typical Cross Section
50X
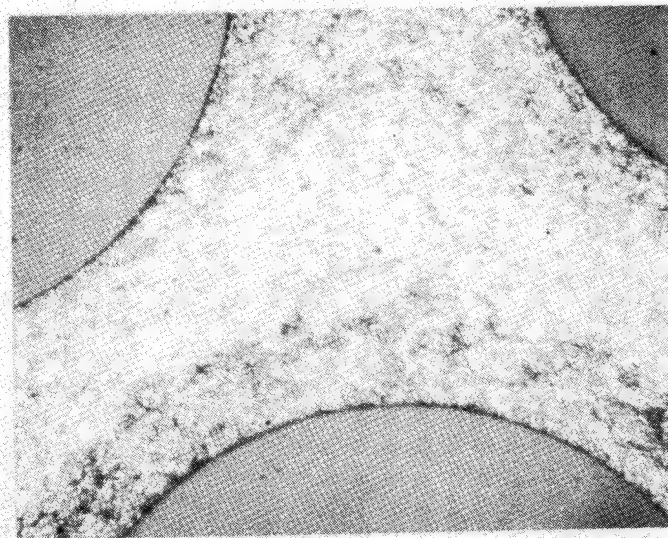
Center of Composite
500X

FIGURE 27. MICRO EXAMINATION OF .2MM BORON/AA1100 ALUM TENSILE
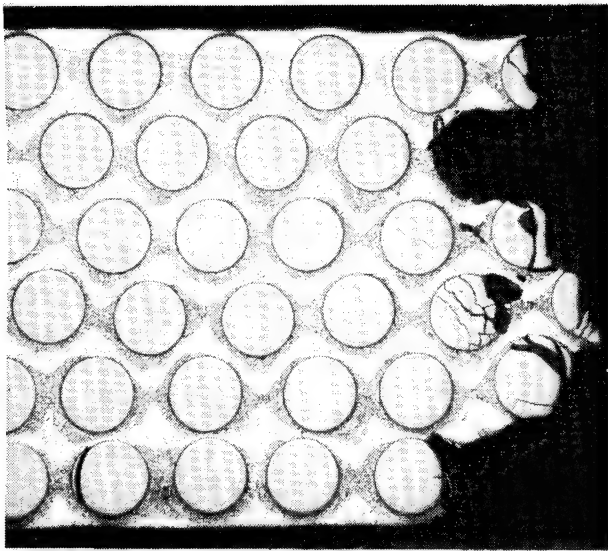REMNANT FROM PANEL 1331
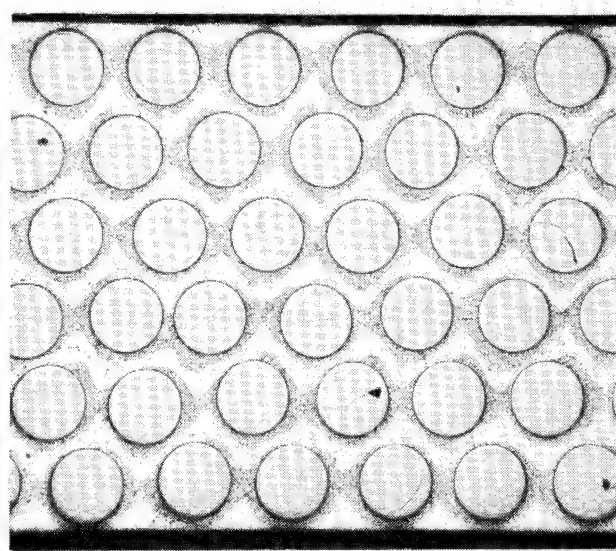
Fracture
50X

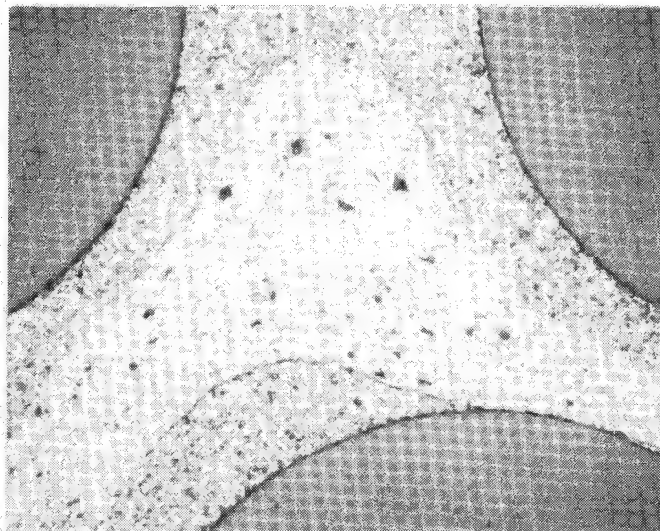Typical Cross Section
50X

Center of Composite
500X

FIGURE 28. MICRO EXAMINATION OF .2MM BORON/AA1100 ALUM TENSILE
REMNANT FROM PANEL 1332

Fracture
50X

Typical Cross Section
50X

Center of Composite
500X

FIGURE 29. MICRO EXAMINATION OF .2MM BORON/AA6061 ALUM TENSILE
REMNANT FROM PANEL 1334

3.2.3.2 Metal Bond Shear Strength Evaluation

In preparation for evaluation of candidate aluminum alloys for shear joint applications, panels were formed from 12 unidirectional layers of boron/aluminum. Panels from both matrix alloys in combination with the 0.2mm boron fiber were made so as to evaluate the candidate substrates with the candidate bond materials. The panel material was consolidated using the same parameters as given in Section 3.2.3.1 with vacuum conditions of 10^{-4} torrs achieved in the laboratory retort.

A double strap joint specimen was selected for shear strength evaluation based on its ability to minimize side deflections thus giving near pure shear results. The specimen, shown in Figure 30, forms four shear surfaces each of 8.9mm length by 12.7mm width. Both candidate matrix materials (AA1100 and AA6061 aluminum) were tested with bond joints formed by the same alloy and bonded to 6Al-4V titanium bar stock. In addition, an AA1100 matrix alloy composite panel was bonded with AA6061 aluminum foil to the titanium stock. Given in Table XII are the results of these tests conducted per ASTM3528-76 with the exception of coupon geometry. The AA6061 alloy bonds formed with both alloy matrixes produced results of 105 MPa (15.3 ksi) and 77 MPa (11.2 ksi) which compares reasonably well with text book shear strength value of 83 MPa (12 ksi). Micro examination of test remnants in each case indicated full surface bonding, full consolidation and no observable intermetallic formation with the titanium stock. Figures 31 and 32 are the enlargements of typical bonded surfaces.

The AA1100 matrix panel joined to the 6Al-4V titanium stock with parent material produced an unusually low shear strength result of 11 MPa (1600 psi). This compares with a text book shear strength value of 62 MPa (9 ksi). Micro examination, Figure 33, indicated full bonding during fabrication with no observable intermetallic formation with the titanium, processing cracks or inclusions. The failure plane was found to be between the surface formed by the bond material and the boron/aluminum simulated shell material. As a result of the test effort expended on bond strength evaluation, no conclusion can be reached as to suitability of AA1100 aluminum as a bond material. Low bond strength properties have been reported on AA1100 matrix materials in reference 2 publication, thus lending weight to avoidance of this alloy in this application. With shear strength values considered adequate for AA6061, the choice was made to use this alloy in subsequent simulated airfoil pressings.
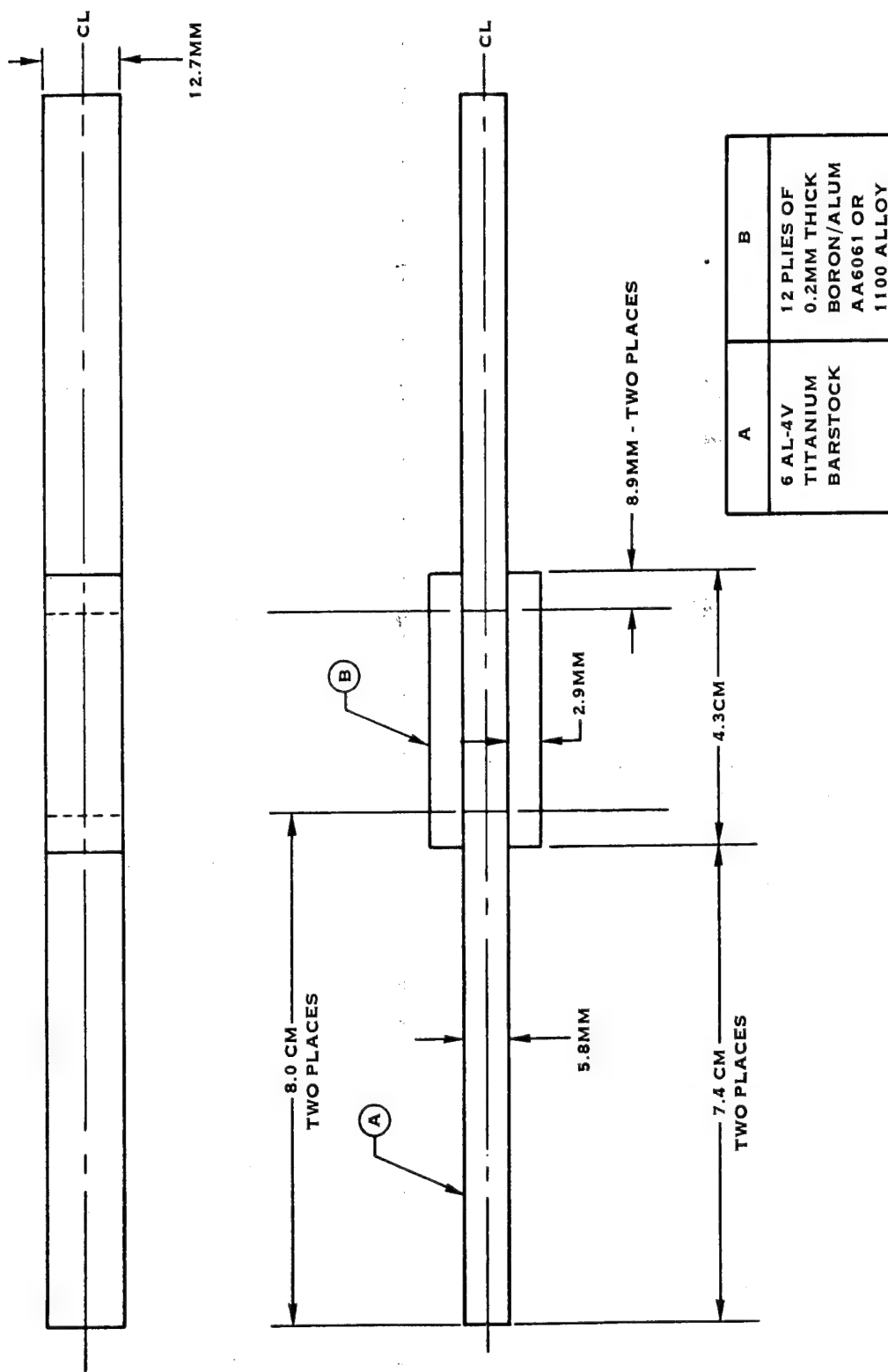
FIGURE 30. DOUBLE STRAP JOINT SPECIMEN USED TO EVALUATE BOND STRENGTH OF BORON/ALUMINUM & TITANIUM DIFFUSION BOND JOINTS

Table XII. Double Strap Joint Lap Shear Test Results of Two Candidate Aluminum Bond Joint Alloys

| Specimen No.	Composite Panel Material (Strap Material)	Bond Material	Tensile Bar Stock	Shear Strength MPa/(PSI)	Failure Mode
VST-1	0.2mm Boron/AA6061 Aluminum	AA6061	6Al-4V Titanium	105 (15,260)	Partially between bond foil and composite panel and partially within composite.
VST-2	0.2mm Boron/AA1100 Aluminum	AA1100	6Al-4V Titanium	11.3 (1640)	Between bond foil and composite panel.
VST-3	0.2mm Boron/AA1100 Aluminum	AA6061	6Al-4V Titanium	76.9 (11,160)	Within composite panel.
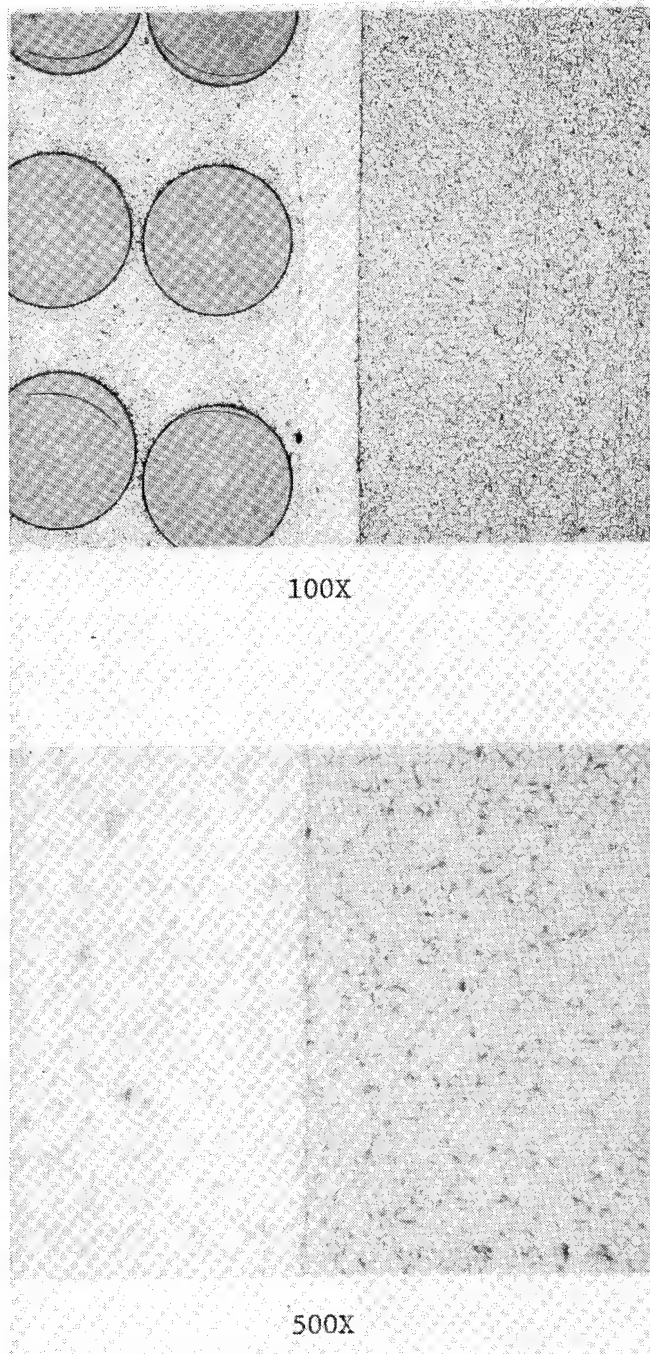
100X

500X

FIGURE 31. BOND JOINT FORMED BETWEEN COMPONENT MATERIALS:
.2MM BORON/AA6061 COMPOSITE; AA6061 FOIL; 6AL-4V TITANIUM
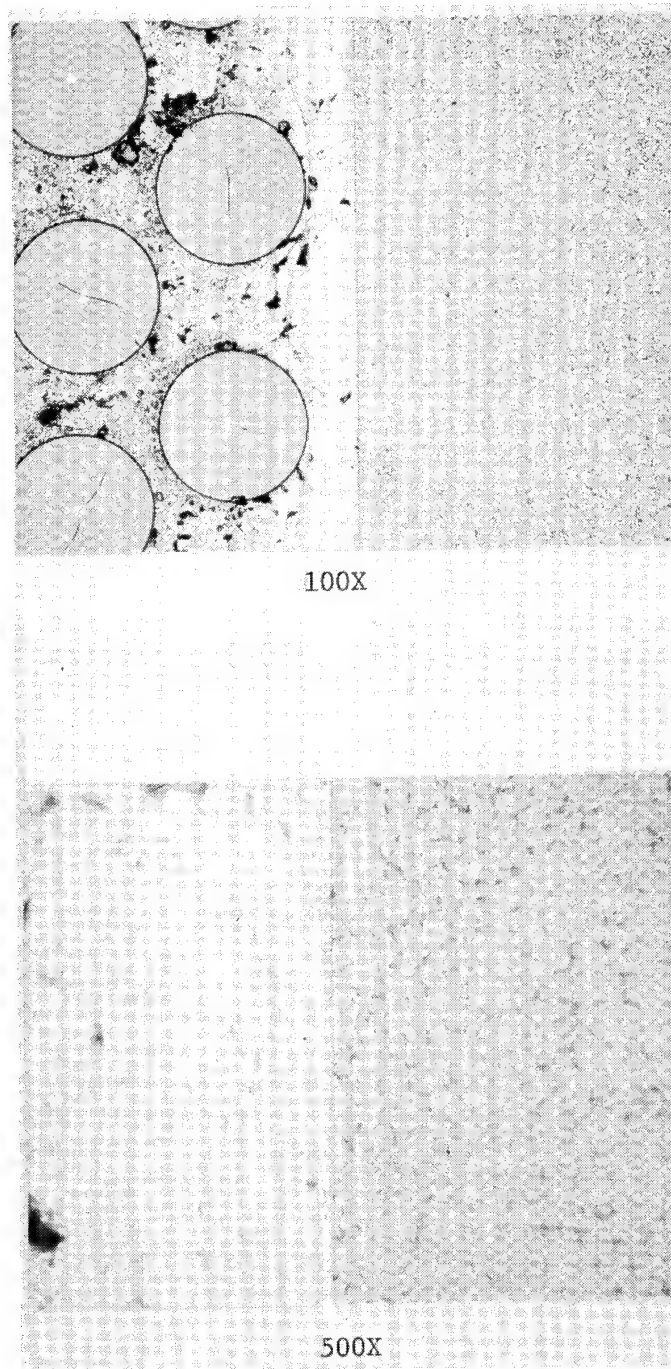
100X

500X

FIGURE 32. BOND JOINT FORMED BETWEEN COMPONENT MATERIALS:
.2MM BORON/AA1100 COMPOSITE; AA6061 FOIL; 6AL-4V TITANIUM
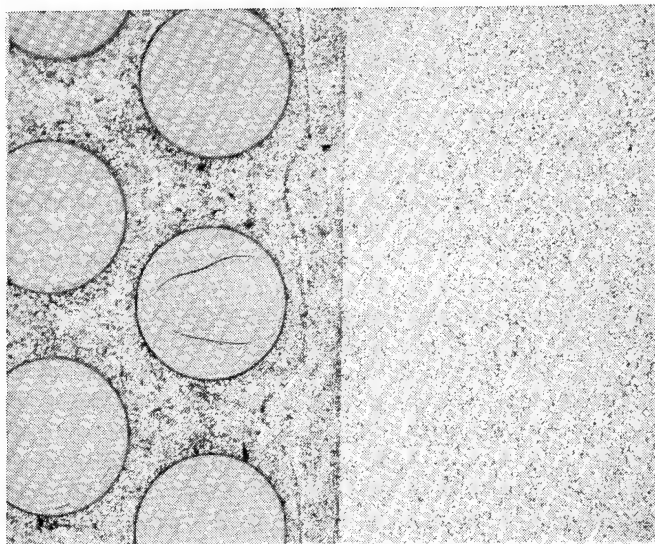
100X
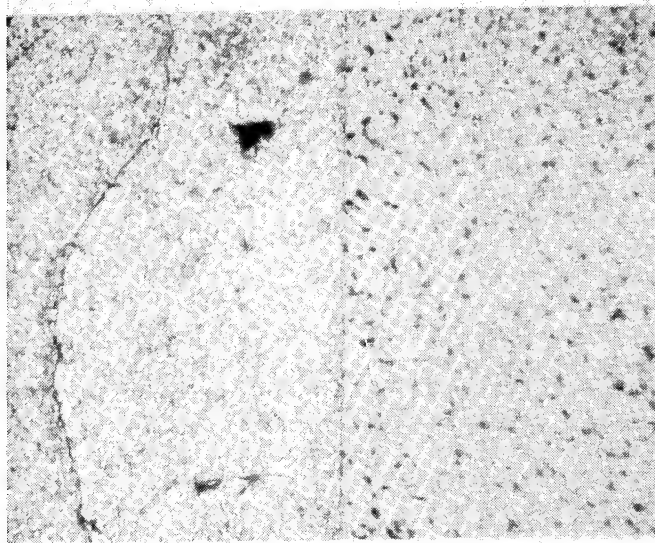
500X

FIGURE 33. BOND JOINT FORMED MATERIALS:
.2MM BORON/AA1100 COMPOSITE; AA1100 FOIL ;6AL-4V TITANIUM

3.2.3.3 Titanium Honeycomb Process & Property Evaluation

The preliminary design task selected a construction which featured titanium honeycomb strips fore and aft of the spar. The functional purpose of the honeycomb is to provide a lightweight internal reinforcement increasing the rigidity of the shell panels between the unsupported length formed by the joints with the spar and the shell leading and trailing edges. With a need to minimize potential panel vibration, candidate materials were examined with the selection of titanium honeycomb best meeting the combination of lightweight and strength at processing conditions.

With the necessity to form the spar to shell bond joint at 34.5 MPa (5000 PSI) and 533°C (1000°F), it was recognized that no candidate material could alone support the processing load without incurring substantial deformation. By bonding to materials of vastly different compressive properties, the more rigid material provides a control of the shell deflection. Thus, in theory, with well-matched, rigid die surfaces, a continuous exterior contour can be maintained with control of die surface travel. In practice, however, an experimental means has been employed to enhance the pressure distribution over a bonding surface. This method includes use of an aluminum insert between the die surface and the assembly to be bonded. With this "tool" employed for low volume experimental programs, the simplicity of the theoretical mechanics of bonding dissimilar compressive strength materials is modified. In bonding practices anticipated to be used, a substantial compressive rigidity requirement for the filler material was anticipated. Thus a primary property selected for evaluation is the compressive and "crush strength" of candidate honeycomb materials.

A second consideration with the use of titanium honeycomb as a sandwich construction core material in the application stress field is its bond strength requirements. The honeycomb to shell bond joint carries both a centrifugally generated shear stress and localized vibratory induced shear and peeling stresses. Owing to both the difficulty of obtaining meaningful shear stress test results with honeycomb and the potential existence of a peeling failure mode, the choice of a peel test was made to evaluate honeycomb bond quality.

Three available titanium honeycomb materials all made from 3Al-2.5V titanium with varying densities were selected for evaluation.

1. 109 kg/m^3, 0.05mm foil, 4.76mm cell
    (6.8 lb/ft^3, 0.002" foil, 3/16" cell)

2. 128 kg/m^3, 0.094mm foil, 6.35mm cell)
    (0.80 lb/ft^3, 0.0037" foil, 1/4" cell)

3. 352 kg/m^3, 0.013mm foil, 4.76mm cell)
    (22 lb/ft^3, 0.005" foil, 3/16" cell

The first consideration of honeycomb compressive/crush strength consists of a room temperature test measuring peak stabilized compressive strength and the subsequent lower constant load plastic deformation "crush strength." Coupons measuring 25.4mm x 25.4mm (1.0 in x 1.0 in) with a cell stabilization sheet bonded to both sides of the cell are tested to ASTM C365-57 and MIL-STD-401 with the exception of coupon geometry. As is readily seen in Table XIII the highest density honeycomb (352 kg/m^3) yields at a weighted average stress level of 31.4 MPa (4560 psi) which is less than the proposed elevated temperature bonding pressure of 34.9 MPa (5000 psi). With an expected 45% reduction in strength at 533°C (992.5°F) temperature, the shortfall in compressive strength becomes approximately 50% of the applied load. The result of these tests is the verification of the necessity to control the travel of the entire die surface. If travel were allowed to be strictly a function of the resistance of the detail parts to compaction, the regions supported by the honeycomb alone would undergo substantial deflection during bonding with a resultant permanent local depression unavoidable.

The bond test specification employed for peel strength evaluation was ASTM D-1781. Exceptions to the specification involved the test coupon geometry which measured 76.2mm (3.0 in) in length by 25.4mm (1 inch) in width by 15.2 - 20.3mm (0.6-8 in) in depth. Diffusion bonded to both sides of the honeycomb cells was a 0.41mm (0.016 in) foil of 6Al-4V titanium creating bond joint thickness of 0.09-0.36mm (0.0035-0.014 in) using AA6061 aluminum foil. The titanium cover sheet on one side was prebent to form a small bond radius. Testing was performed on a tensile test machine to measure the average load required to maintain the continuing peel separation of the titanium foil from the honeycomb cells. The results of those tests are presented in Table XIV. The peel strength increased with honeycomb surface area with the 352 kg/m^3 density material 3.8 times the peel strength of the 109 kg/m^3 density product at 12.4 N/cm (7.1 lbs/in) versus 3.3 N/cm (1.9 lbs/in), which roughly follows surface area ratios. No substantative fillet formation was judged to have occurred owing to low wetting tendencies of the bonding material on titanium. A determination of the adequacy of this data for the product application was not made. Engineering judgment is that the honeycomb to shell joints would be adequate for the loads to be applied.

Table XIII. Stabilized Compressive Strength and Crush Strength Properties of Candidate 3Al-2.5V Titanium Honeycomb Material

Honeycomb Density kg/m³/(lbs/ft³)	Number Specimens	Cover Material	Average Stabilized Comp. Strth. MPa/(psi)	Average Crush Strength MPa/(psi)
109 (6.8)	1	6Al-4V Tit.	9.6 (1350)	2.3 (330)
128 (8.0)	2	6Al-4V Tit.	12.1 (1750)	4.7 (675)
	1	0.2mm B/6061 Alum	9.2 (1340)	3.4 (500)
Weighted Average			11.1 (1615)	4.2 (615)
352 (22)	2	6Al-4V Tit.	35.2 (5100)	15.5 (2250)
	4	0.2mm B/6061 Alum	29.6 (4290)	14.4 (2090)
Weighted Average			31.4 (4560)	14.8 (2145)

Table XIV. Average Peel Strength of Three Candidate 3Al-2.5V Titanium
Honeycombs Bonded to 6Al-4V Titanium

Honeycomb Density kg/m^3/(lbs/ft^3)	Number Specimens	Peel Strength N/cm/(lbs/in)	Theoretical Bond Area Ratio
109 (6.8)	2	3.3 (1.9)	1:1
128 (8.0)	7	6.5 (3.7)	1.4:1
352 (22.0)	5	12.4 (7.1)	2.5:1

80

3.2.4 Simulated Airfoil Pressings - Part Manufacture

3.2.4.1 Shell Fabrication

The exterior shell geometry for the simulated airfoil pressings were based on the QCSEE FOD demonstration blade (HS drawing 759043). With the selection of 0.2 mm (0.008 in.) boron/aluminum in place of 0.14 mm (0.0057 in.) borsic/aluminum ply material, a reduction from ten to seven plies per shell-half was achieved. With a similar maximum consolidated thickness of 1.45 mm (0.057 in.) versus 1.42 mm (0.056 in.) no die modification was deemed necessary. The larger diameter boron/ aluminum material ordinarily would necessitate resizing the individual plies in order to maintain a similar cross-section profile as previously designed and produced, however, through use of an aluminum pressure distribution (mush) layer, this modification was avoided. Figure 34 shows the camber (convex) side ply templates used to properly size and orient the boron/aluminum material. Use of the Hamilton Standard computer controlled ply cutting equipment was deemed not warranted owing to the small lot size of the part requirements. Figure 35 shows the seven unconsolidated camber shell plies along with the 6A1-4V titanium outer erosion protection skin. The unconsolidated assembly of the plies and the titanium skin, were welded together using AMS5512 0.5 mm (0.002 in.) strip stock material inboard and outboard of the actual final trimmed shell area. In addition, individual plies were tack welded together again in regions trimmed off prior to bonding with the spar. The ply orientations selected for the demonstration pressings, given in Figure 22 simulated the QCSEE blade specification in order to allow utilization of existing ply templates. A total of six sets of shell assemblies were made with two sets made from AA1100 and four sets from AA6061 aluminum matrix alloys.

The shell shaping and consolidation bonding operation was performed utilizing the dies shown in Figure 25. A passive internal tooling mandrel machined to the face and camber shell interior contours was used to provide the proper die interior shape. A schematic of the shell consolidation tooling is shown in Figure 36 which also illustrates the necessity of consolidation of each shell-half in a separate press cycle. The bonding dies which are comprised of active upper and lower halves utilize electrical resistance heating elements each of which contained two separately controllable heating zones. Temperature surveys were run on the dies with the internal mandrel and temperature instrumented dummy stainless steel camber and face ply assemblies installed. The surveys determined the uniformity of the four heat controlled zones and established the required temperature setting necessary for each zone in order to provide the proper shell bonding temperature. In addition, with the selection of the "quick-vac" vacuum bonding process, which features an insertion of the shell ply layup package into a preheated die and subsequent rapid evacuation for vacuum atmosphere bonding, it was necessary to establish the recovery time from heater shutoff for package insertion to reattainment of bonding temperature.

Based on the above temperature surveys, a time, temperature, pressure, vacuum, and process cycle was established as follows: The four temperature controllers were set at temperatures within the range of 533 ± 15°C (992.5 ± 27.5°F), die temperatures were monitored until the die temperature stabilized in a vacuum of 1 x 10^{-1} torrs or less. The vacuum and the power were shut off and the chamber door opened. The dies were opened and the shell layup package placed between the mandrel and either the camber or face side die half. The dies were closed until contact pressure was achieved. The retort door was closed and the vacuum pumps turned on, and after a vacuum of 2 x 10^{-1} torrs was reached, (1 minute elapsed time), the heating element power was turned on. A stabilized vacuum of 1 x 10^{-1} torrs or less was reached in 2 minutes. Ten minutes from the time the shell layup contacted the hot dies, the press loading was increased to exert a pressure of 20.7 MPa (3 KSI) on the shell layup. Similarly after eleven and twelve minutes, the pressure was increased to 31 MPa and 37.9 MPa (4.5 and 5.5 KSI), respectively. After seven minutes at the maximum load (19 minutes after die closure), heater element power was shut off, the chamber vacuum allowed to reach atmospheric condition, and the diffusion bonded shell removed from the dies. A bond cycle process schematic is given in Figure 37. Figure 38 shows the shell being removed from the die and Figure 39 shows a consolidated set of shells from the boron/aluminum and titanium sides respectively.

3.2.4.2 Sheath Fabrication

The leading edge of the blade is comprised of a three piece sheath made from tapered titanium alloy sheet stock aluminum bonded to produce a near final cross-sectional shape. The 6Al-4V titanium sheet stock is chem milled to provide a chord-wise taper for the two flank pieces and a spanwise taper for the nose piece. The bonding with AA6061 aluminum alloy was selected over a titanium/titanium diffusion joint owing to end product usage as a manufacturing feasibility demonstration. The bond cycle of 565.5°C (1050°F)/10^{-4} torr vacuum/55.2 MPa (8 KSI)/30 minutes was developed for the sheath assembly utilized in the APSI blade program under A/F contract F33657-73-619. Figure 40 shows a schematic of the bonding assembly utilized for sheath joining. Figure 41 gives the final finished detail part shape of the sheath. A total of 4 sheaths were made for use in the manufacture of two simulated airfoil pressings.
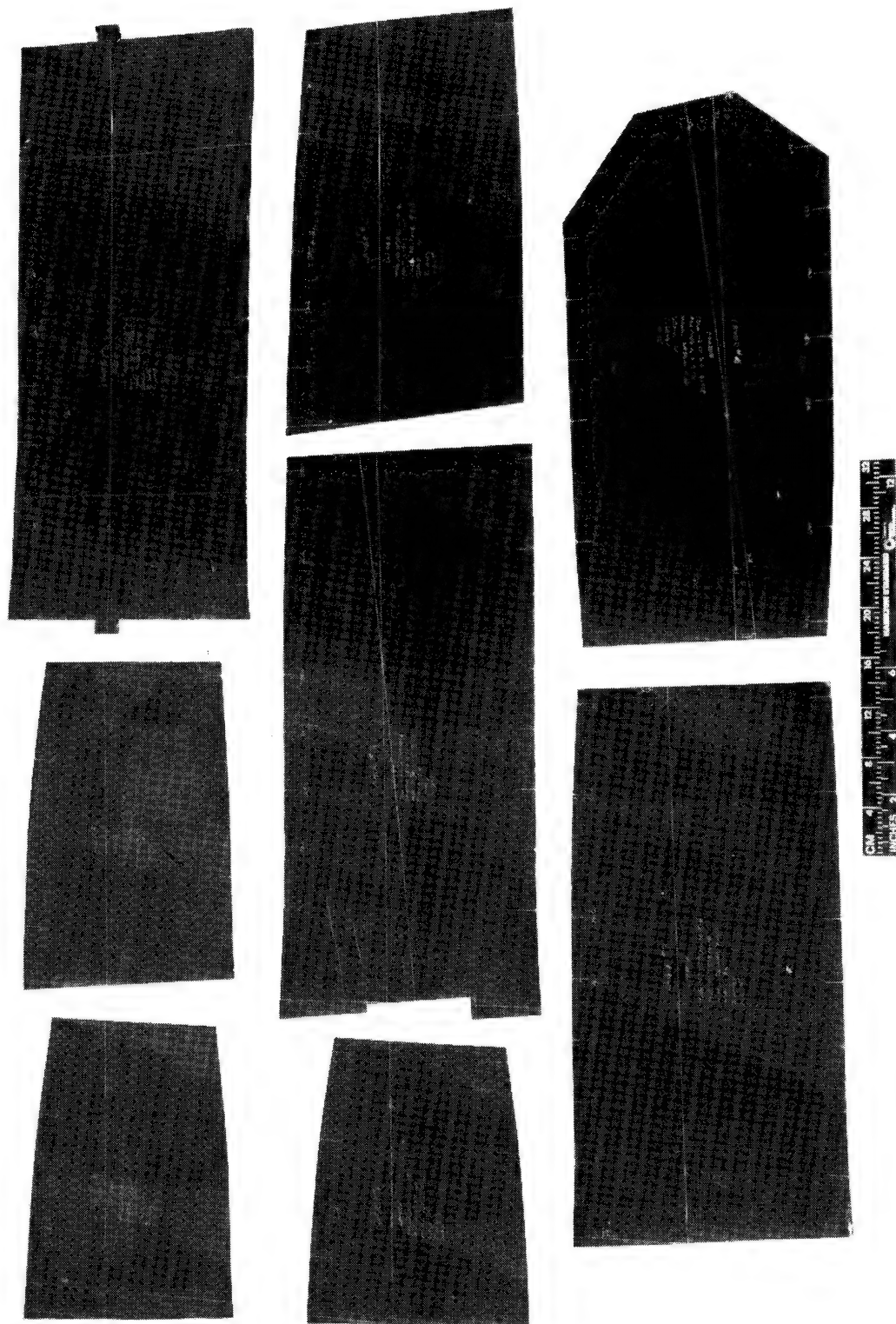
FIGURE 34. TEMPLATES USED TO ORIENT & SIZE BORON/ALUM SHELL PLIES FOR DEMONSTRATION AIRFOIL PRESSINGS

S 51277
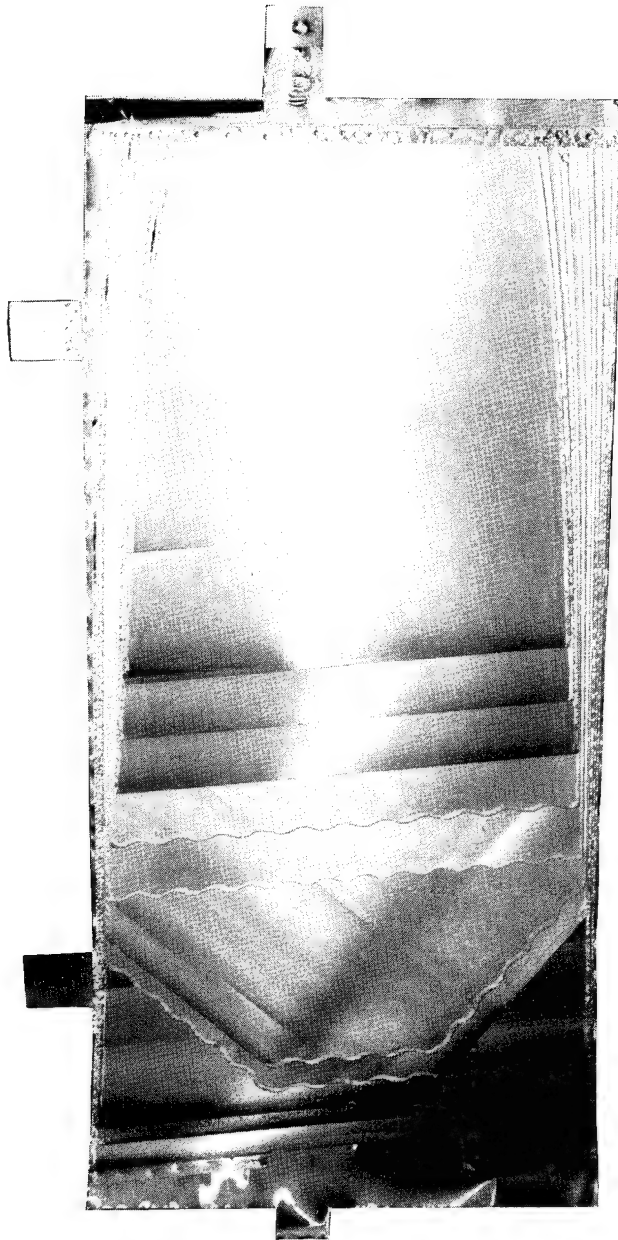
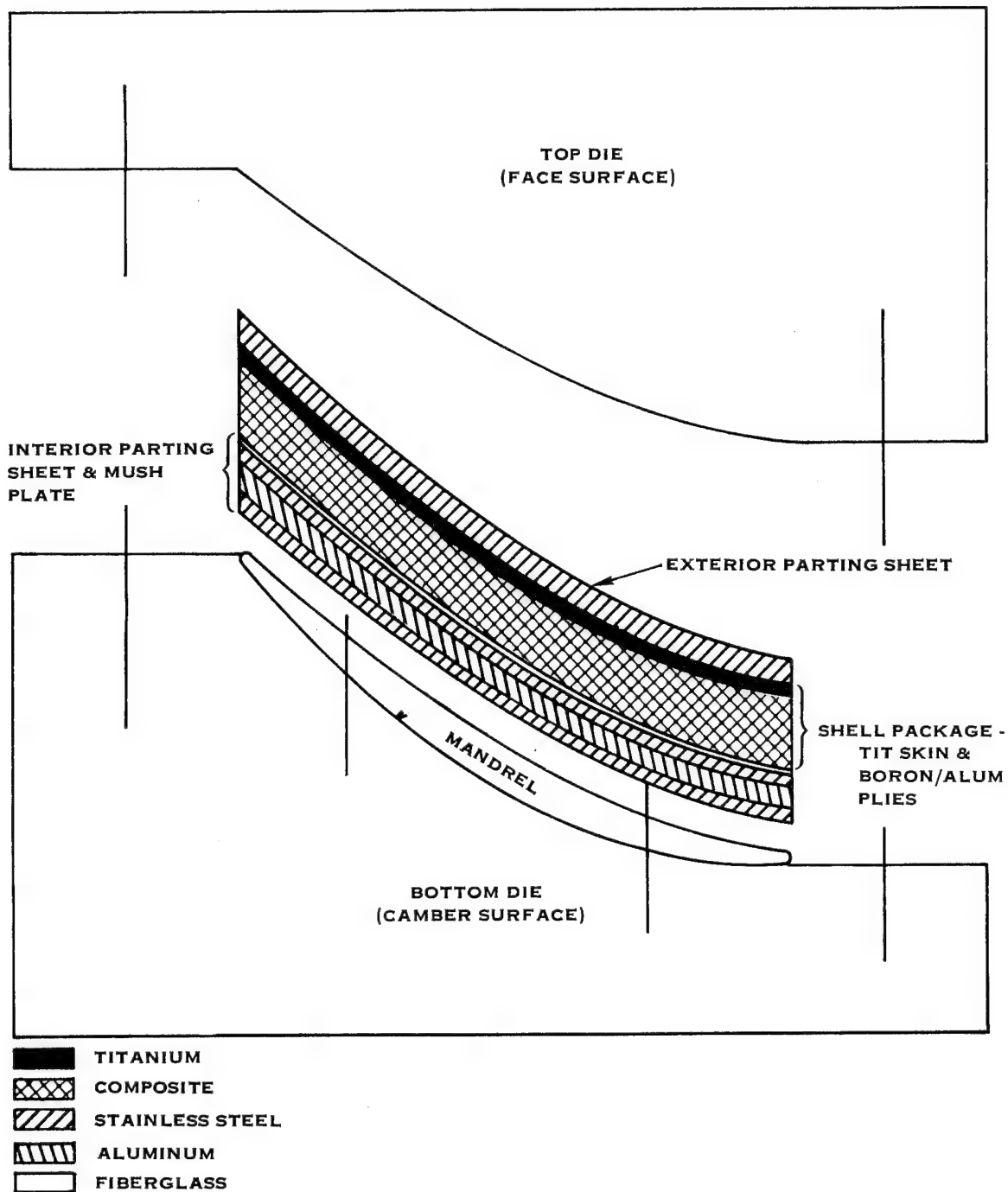83

FIGURE 35.   SHELL PLY STACKUP BEFORE CONSOLIDATION

TOP DIE
(FACE SURFACE)

INTERIOR PARTING
SHEET & MUSH
PLATE

EXTERIOR PARTING SHEET

MANDREL

SHELL PACKAGE -
TIT SKIN &
BORON/ALUM
PLIES

BOTTOM DIE
(CAMBER SURFACE)

TITANIUM
COMPOSITE
STAINLESS STEEL
ALUMINUM
FIBERGLASS

FIGURE 36. SCHEMATIC OF DIE & MANDREL ASSEMBLY USED TO
CONSOLIDATE COMPOSITE SHELL MATERIAL
(TOOLING POSITIONED FOR CAMBER SHELL PRODUCTION)
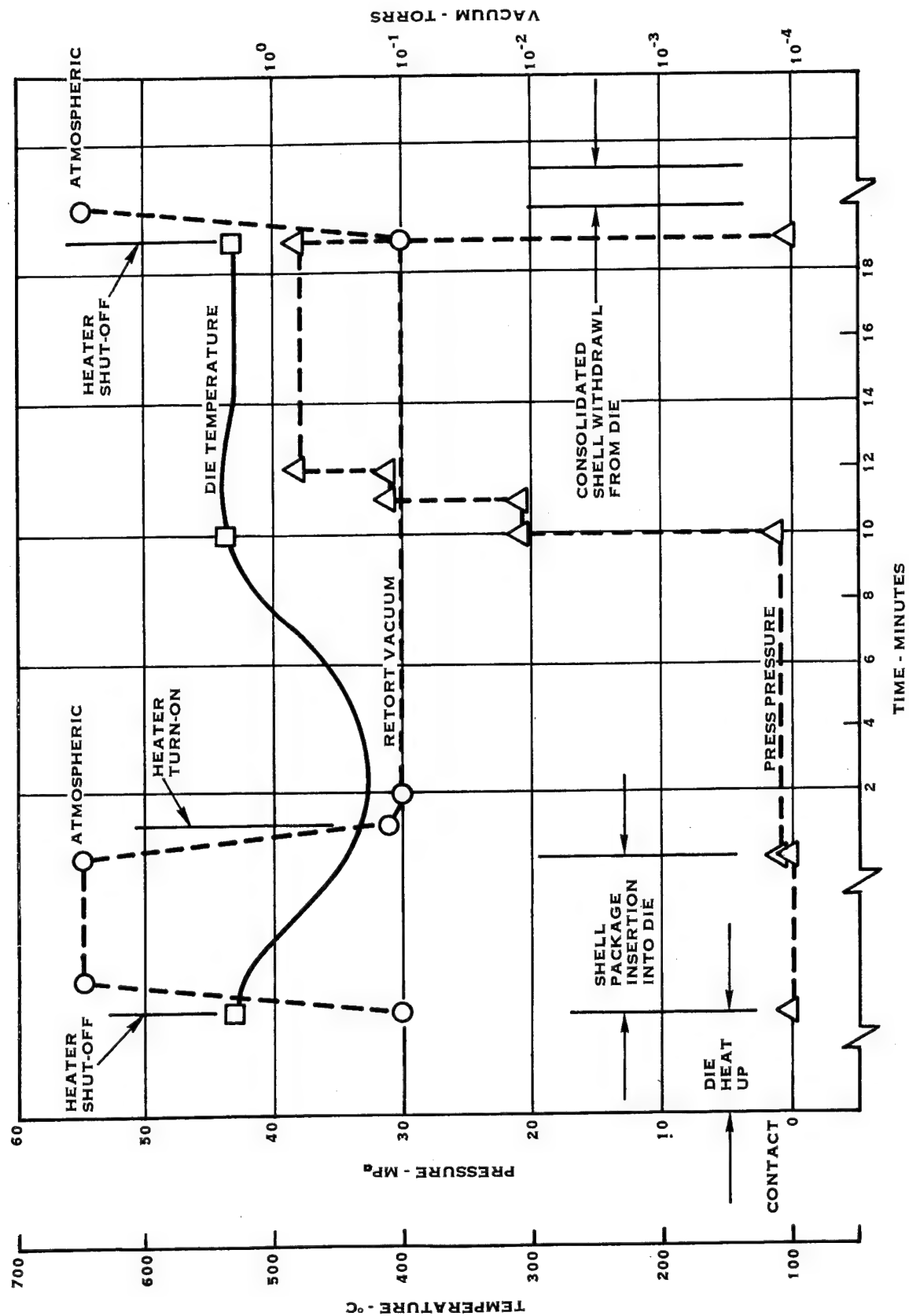
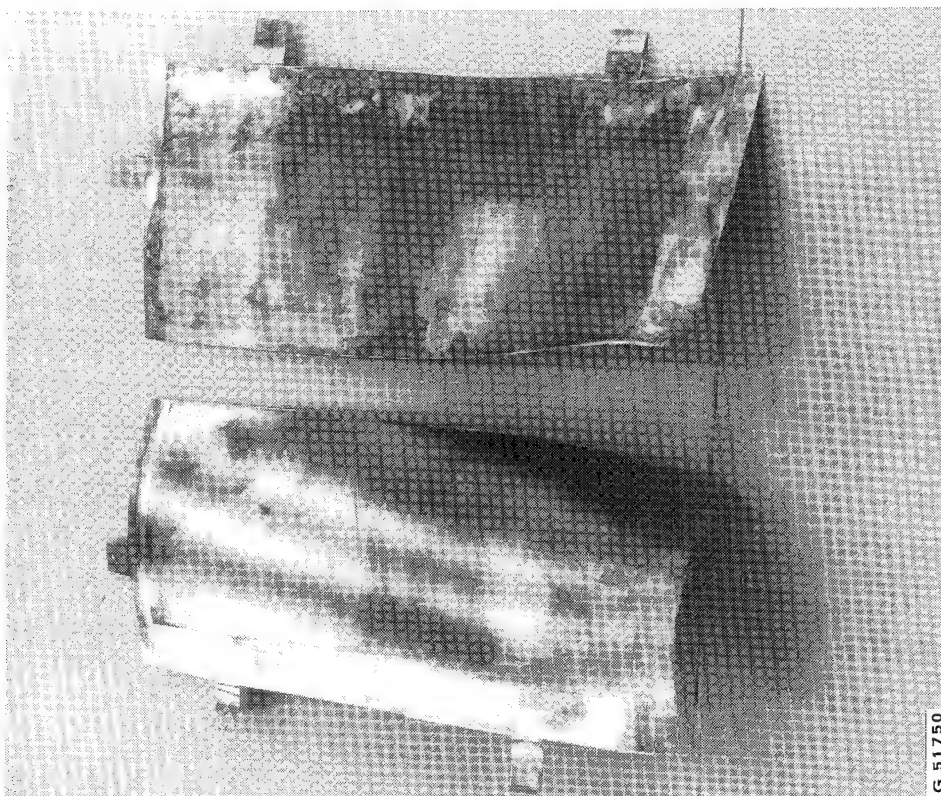FIGURE 37. DIFFUSION BOND CYCLE FOR BLADE SHELL CONSOLIDATION

CONSOLIDATED SHELL ASSY
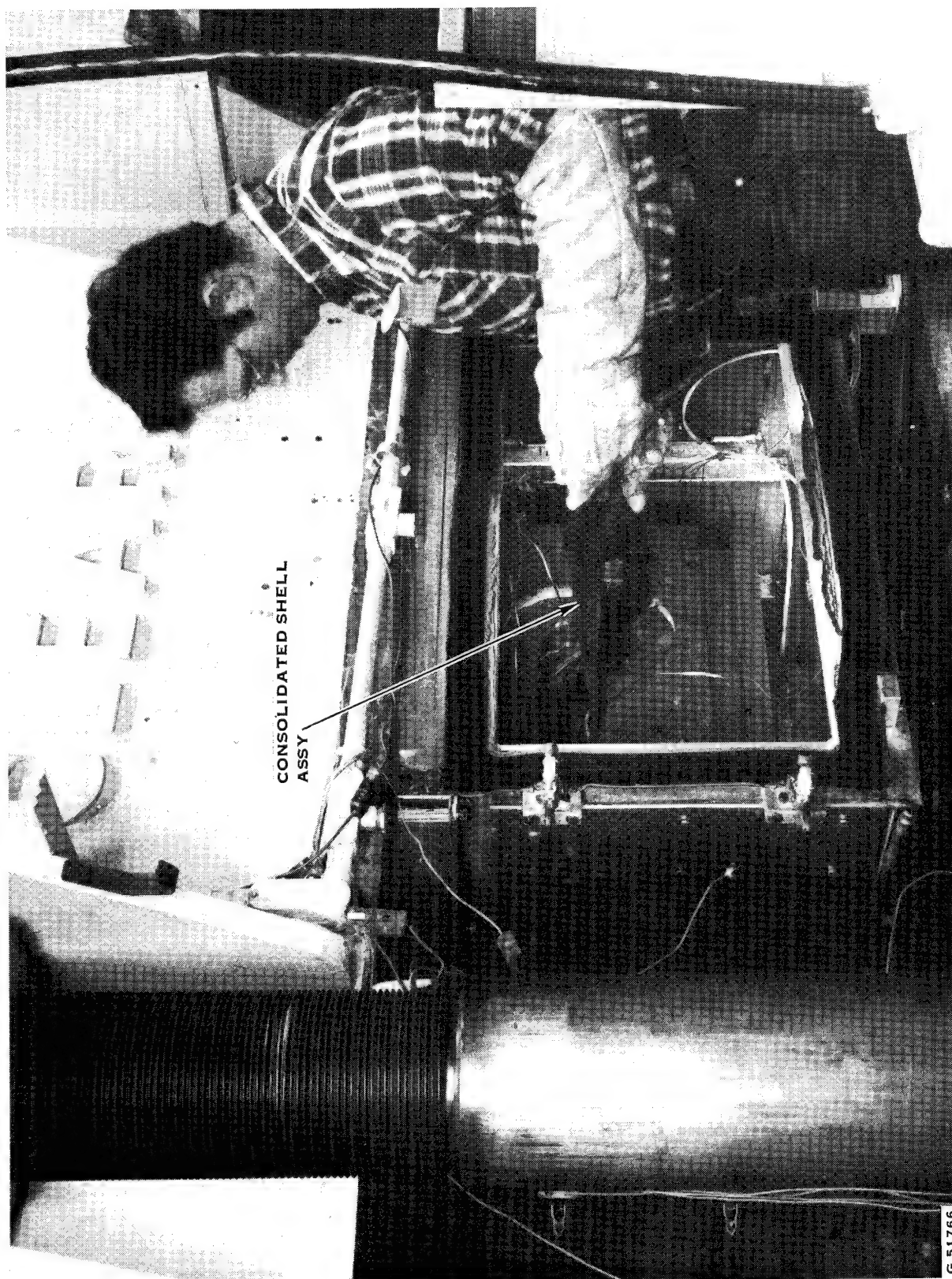
FIGURE 38. SHELL PRESSING BEING REMOVED FROM "QUICK-VAC" BONDING PRESS

G 51766
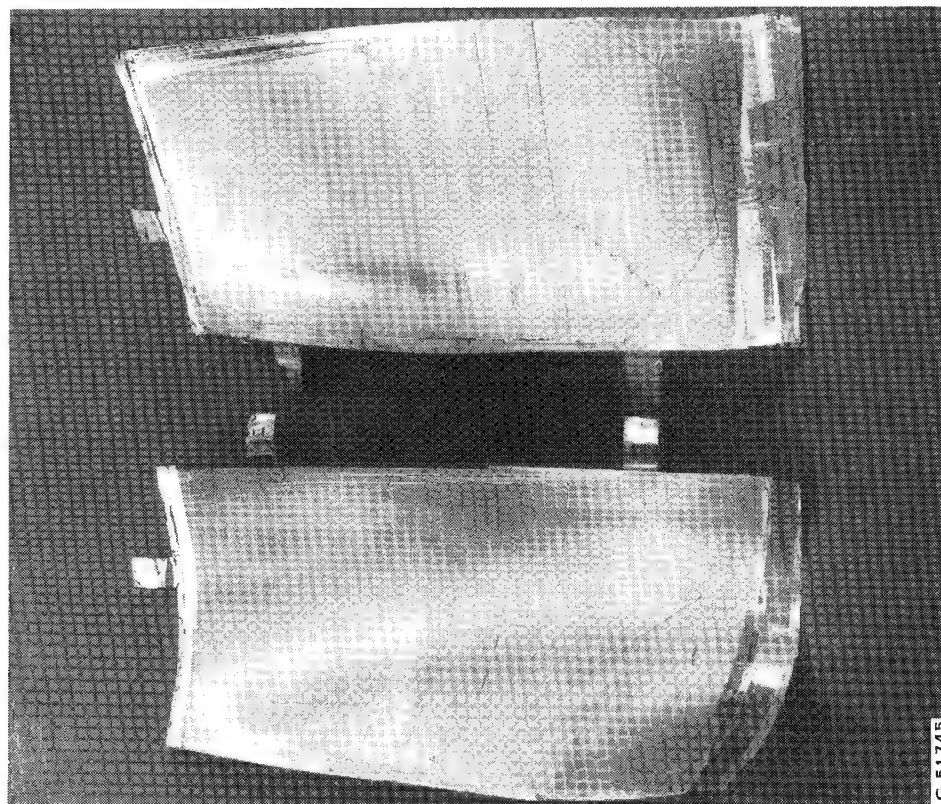
87

INTERNAL SURFACES

EXTERNAL SURFACES

FIGURE 39. CONSOLIDATED SHELL PRESSINGS EXTERNAL & INTERNAL SURFACES AFTER BONDING
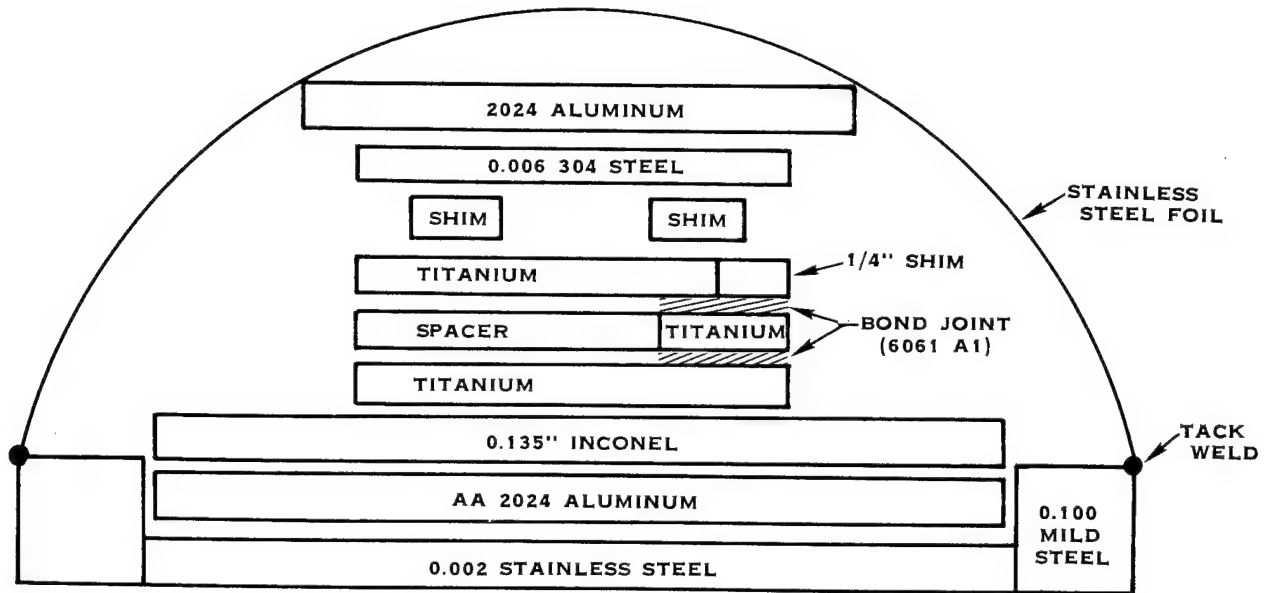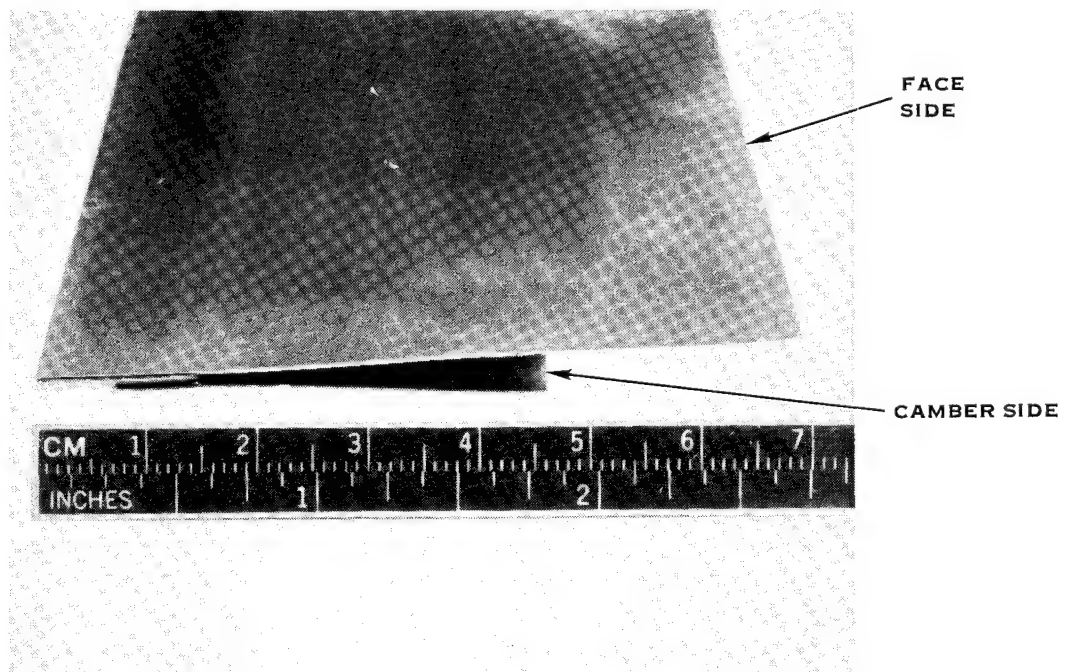
88

FIGURE 40. MATERIAL LAYUP FOR TITANIUM SHEATH BONDING

FIGURE 41. END VIEW OF DIFFUSION BONDED SHEATH ASSEMBLY

89

3.2.5 Simulated Airfoil Pressings - Assembly

The assembly of an airfoil from the six component parts, see Figure 42 (two shells, two titanium honeycomb structural inserts, a titanium spar and a 3-piece bonded titanium sheath) was performed in two steps. The joining of airfoil shells, honeycomb internal reinforcement and structural spar were performed in step one. A selection of the better candidate airfoil subassembly from the two matrix candidate pressings was then made for the subsequent step two sheath to-shell joining operation. The shell forming die tooling was adapted for use in performing both assembly joining operations owing to the processing conditions required to produce aluminum bond joints.

3.2.5.1 Shell to Spar and Honeycomb Metal Joining

The forming of the structural joints between the blade shells and the structural spar and titanium honeycomb internal reinforcement entailed detailed part surface preparation, part fixturing and bond forming in a vacuum atmosphere. As previously discussed die selection was based on experience, cost and process condition criterias. With the two die surfaces displaced from one another so as to provide adequate space for the interior forming mandrel, usage for shell to spar joining necessitated identification of and correction for that spacing. This was accomplished by utilizing a clay material sandwiched between die surfaces and an existing QCSEE adhesively bonded blade. With the necessary minimum shim thickness established the material selected for same include a 0.4mm (0.016 in.) AISI347 stainless steel parting sheet against the blade contact surface, a 0.05mm (0.002 in.) stainless steel parting sheet against the die surface (both used to inhibit joining with both blade and die) sandwiched around a 1.8mm (0.071 in.) AA2024 aluminum pressure distribution layer (mush layer).

The complexity of locating the five individual parts in proper location to one another and maintaining their location during the pressing operation necessitated use of an assembly jig. Shown in Figure 43 is the assembly jig which provided indexing of the spar and honeycomb details in relation to the face and camber shells. The 128 kg/m^3 (8#/ft^3) honeycomb inserts were tackwelded to the spar which in turn was riveted at the outboard end and strap welded at the inboard end to the shell assembly. The shell halves were riveted to one another at the blade tip which in combination with the aforementioned riveting and strap welding was judged adequate to maintain detail part placement during the pressing operation. The stainless steel and aluminum parting and pressure distribution shim material was subsequently strap welded to the blade assembly as shown in Figure 44 and in this condition the blade was ready for bonding.

Based on the abbreviated bond shear strength evaluation discussed in Section 3.2.3.2, AA6061 aluminum alloy foil stock was selected for joining both matrix alloy shells to the spar and honeycomb internal detail parts. Foil of 0.09mm (0.0035 in.) thickness was placed between the shell and spar/honeycomb detail parts during the assembly part stackup sequence.

The metal bonding cycle selected to join the five detail parts is similar to the diffusion bonding cycle used for shell consolidation differing principally in the extended time required to bring the titanium spar up to bonding conditions. Shown in Figure 45 is the bond cycle used for the joint formation. The die temperature control zones were monitored until a stabilized temperature of $533 \pm 15°C$ ($992.5 \pm 27.5°F$) was achieved for each zone in a 10^{-1} torr vacuum atmosphere. The resistance heaters were then turned off and the chamber vented to atmospheric conditions. The retort door was then opened, the die halves separated and the blade assembly package inserted. As described in Section 3.2.2.1 and shown in Figure 22, a locating fixture properly secures the blade package to the die surfaces by indexing the spar shank in the proper assembled position. The installation of the blade package into the die is shown in Figure 46. The die surfaces were then closed until contact pressure was established and the retort door was then shut. The chamber evacuation was initiated with a 2×10^{-1} torr vacuum established within one minute at which point the die heater elements were activated. Within two minutes the necessary vacuum atmosphere of 1×10^{-1} torrs was achieved. With the substantial spar mass effecting reestablishment of bonding temperature it was elected to monitor the spar temperature for timing of bond pressure application. Thermocouples were placed on the spar tip and shank regions with the outboard end thermocouple keying die pressure application. After 35 minutes stabilized temperatures of $524°C$ ($975°F$) on the outboard end and $482°C$ ($900°F$) on the shank end were achieved. At forty-one, forty-two and forty-three minutes the press pressure was incrementally raised in steps to 20.7 MPa (3 KSI), 31 MPa (4.5 KSI) and 34.5 MPa (5 KSI), respectively. The maximum load was then held for ten minutes to form the bond joint. At the end of ten minutes the die heater elements and retort vacuum pumps are turned off, the retort opened and the airfoil pressings removed. Figure 47 shows the post bonded AA6061 alluminum matrix airfoil pressings. Immediately evident in this figure is the local deformation extending from the perimeter of the spar to the leading and trailing edges of the airfoil in a chordwise direction. The cause of the excessive compaction fore and aft of the spar was the use of the aluminum pressure distribution pad which, as shown in Figure 48, flowed under bonding conditions to airfoil regions of low compaction resistance.

For the AA1100 matrix shell airfoil pressings the same bond joint alloy (AA6061) and bond cycle was utilized. A modification to the pressure distribution pad providing spanwise slots in plane with the spar perimeter, shown in Figure 49, was made in an effort to minimize the region of greatest airfoil deformation which was the transition region between spar leading and trailing edge radius and the titanium honeycomb inserts. In spite of these efforts the processed airfoil pressing again exhibited the same local depressions. With removal of the pressure pad it was evident that the locating tabs failed to restrain the pad from movement during pressing. This motion which slid the relief slots out of alignment with spar perimeter thus negated the attempt to minimize local deformation.

91

The evidence from these airfoil pressing is the inadvisability of using full width and ductile pressure distribution pads when forming the shell to spar joint. The 34.5 MPa (5 KSI) press pressure deemed necessary to produce satisfactorily reliable quality diffusion bond joints was greater than the honeycomb compressive strength. The honeycomb compressive strength along with the shell flexural stiffness must be able to resist the press pressure within their elastic property limits in order to prevent permanent local deformation. The 31.4 MPa (4.6 KSI) room temperature compressive strength titanium honeycomb (352 kg/m^3 density) reported in Section 3.2.3.3 would appear to be very marginal as simply a direct replacement utilizing the identical process. One candidate material not examined which has high temperature high compression strength capabilities suited to the process condition is Inconel 625 honeycomb featuring a .1mm (0.004 in.) foil in a 3.18mm (0.125 in.) hexagonal cell size which has an approximate 672 kg/m^3 (42 lbs/ft^3) density.

3.2.5.2 Sheath to Shell Metal Joining

The metal bond joint formed between the leading edge sheath and the metal matrix and titanium shell halves is considered a key element in producing blades which meet acceptable foreign object damage (FOD) resistance. In fact, this bond joint is considered more critical then the shell to spar joint owing to the high local impact stress superimposed on the sheath's static stress and joint shear stress during the impact event. Owing to both schedule and financial restraints it was elected, with contracting officer approval, to install the leading edge sheath on one of the two airfoil pressings. The selection of the AA6061 matrix pressing over the AA1100 matrix pressing was arbitrarily made.

The sheath joint formation process consisted of detail part surface preparation, blade assembly with sheath detail and diffusion bond joint formation. Shell sizing consisted of local thinning and trimming operations to meet the sheath inside envelope. During shell consolidation shim material had been used to form the necessary leading edge depression for later installation into a sheath. The bond joint formation process followed the procedure described in Section 3.2.5.1 for shell to spar joining; however, with the cycle times used in shell consolidation, Section 3.2.4.1 utilized. As in forming the spar joint the temperature of the region being joined was monitored with press pressured applied. At a stabilized 533 ± 15°C (992.5 ± 27.5°C) sheath temperature the timing of the bonding condition cycle was started. After ten minutes on condition, the vacuum pumps and heater elements were turned off, retort allowed to return to atmospheric condition, chamber and press opened and airfoil pressing removed from the dies. The airfoil pressings were subsequently cleaned and trimmed to size in preparation for final inspection.
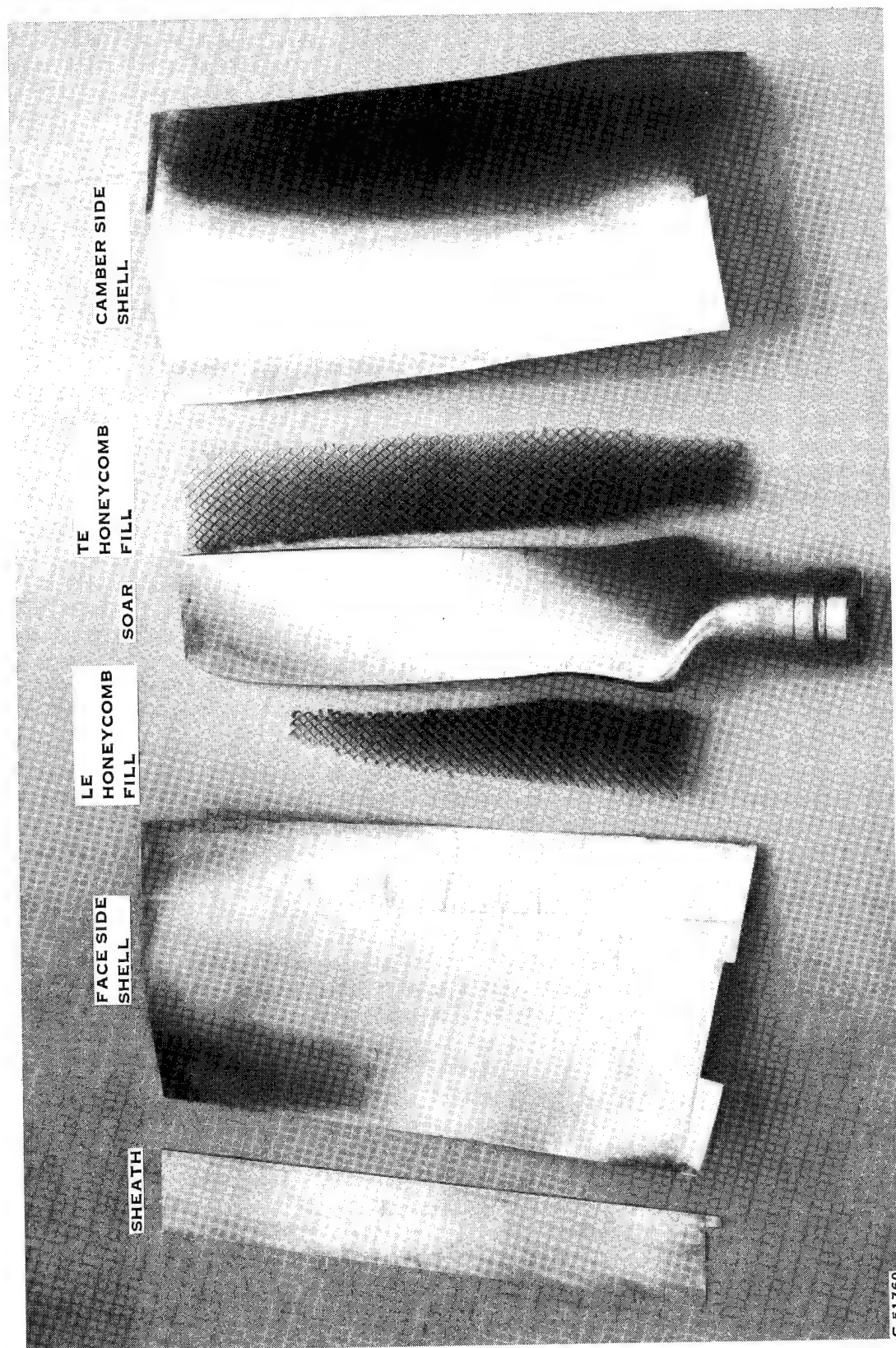
FIGURE 42. DETAIL PARTS OF DEMONSTRATION AIRFOIL PRESSING PRIOR TO ASSEMBLY

SPAR

TITANIUM
HONEYCOMB

G 51751

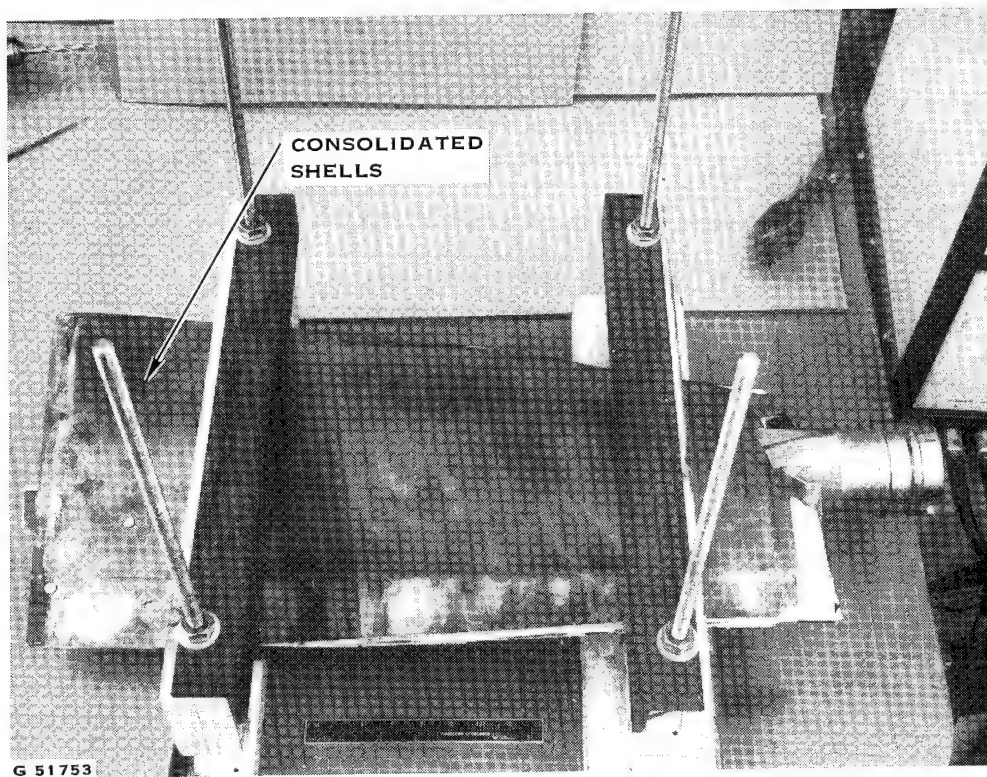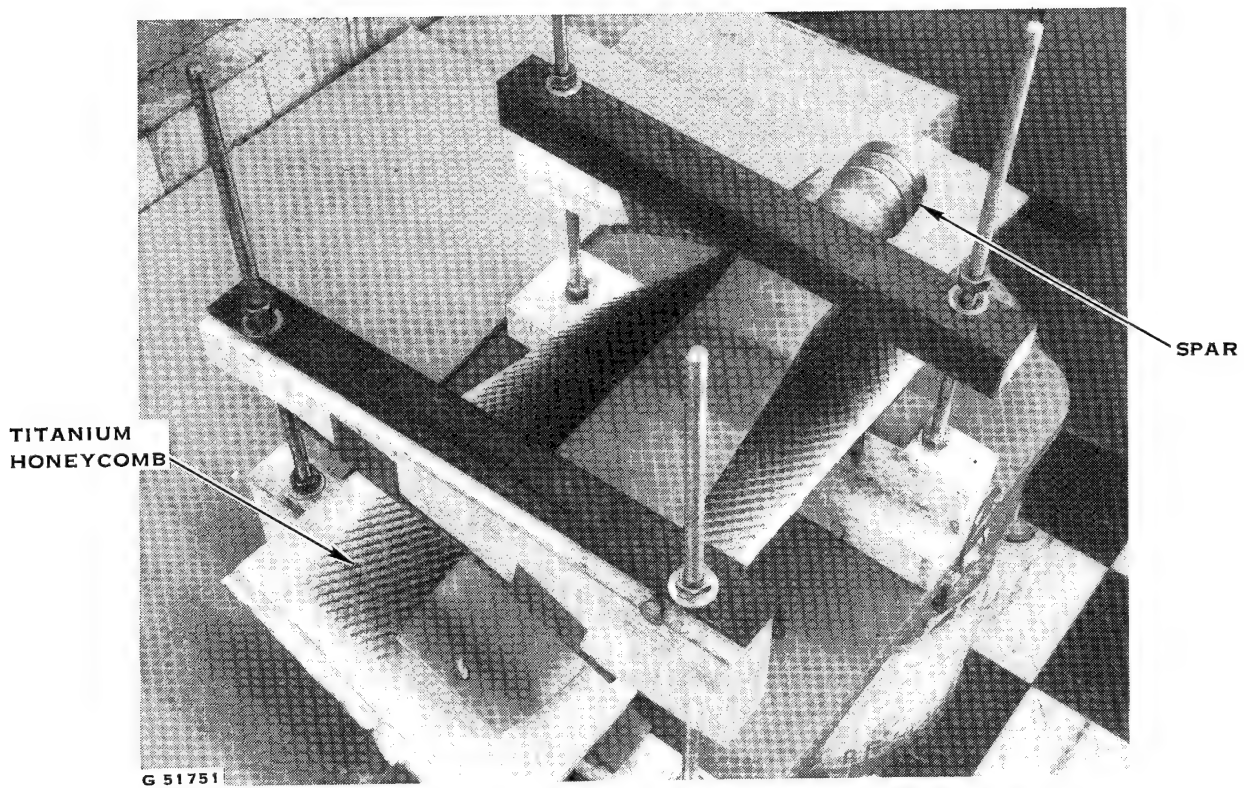CONSOLIDATED
SHELLS

G 51753

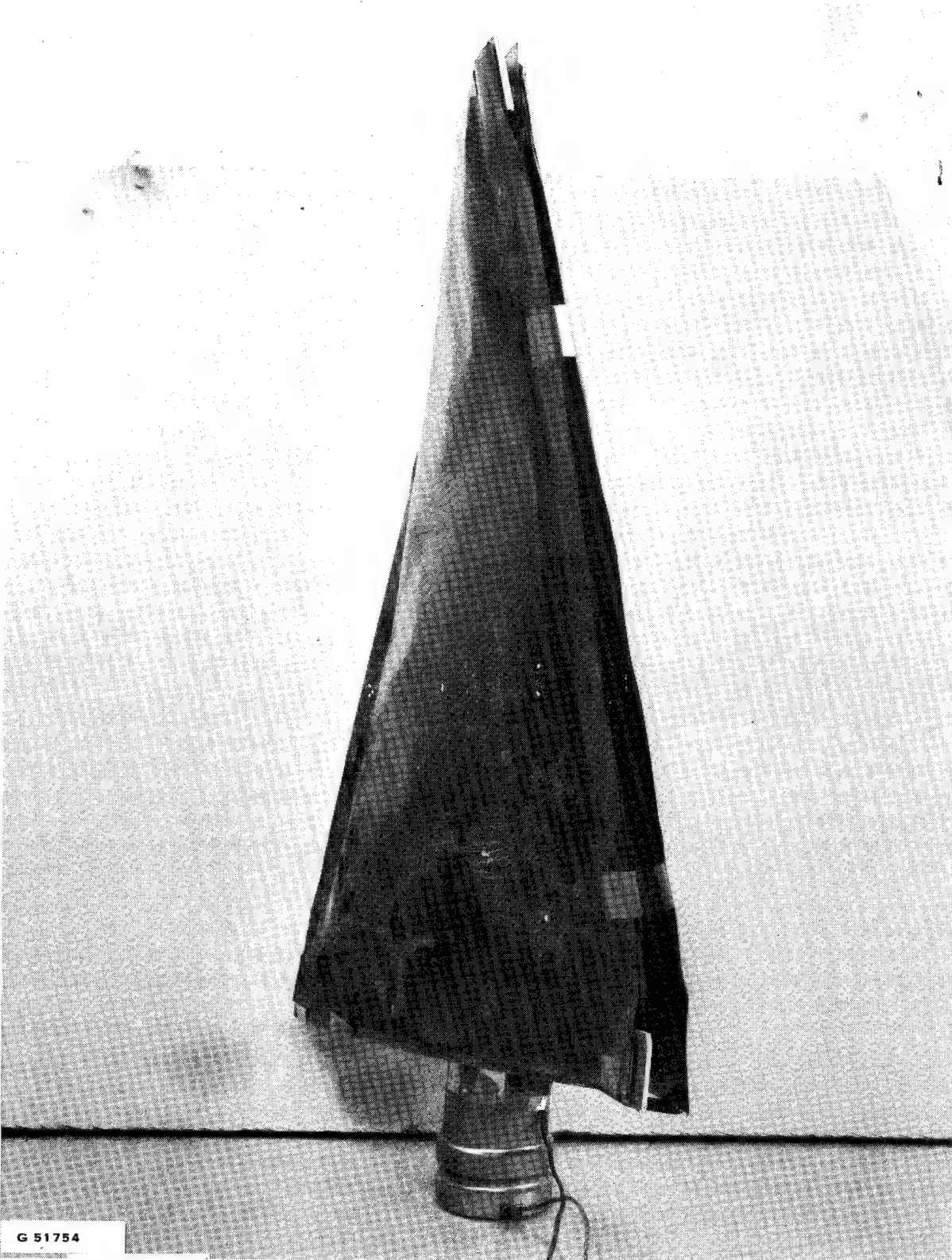FIGURE 43. ASSEMBLE JIG USED FOR DETAIL PART ASSEMBLY PRIOR TO METAL JOINING

FIGURE 44.   ASSEMBLY OF DEMONSTRATION PRESSING DETAIL PARTS
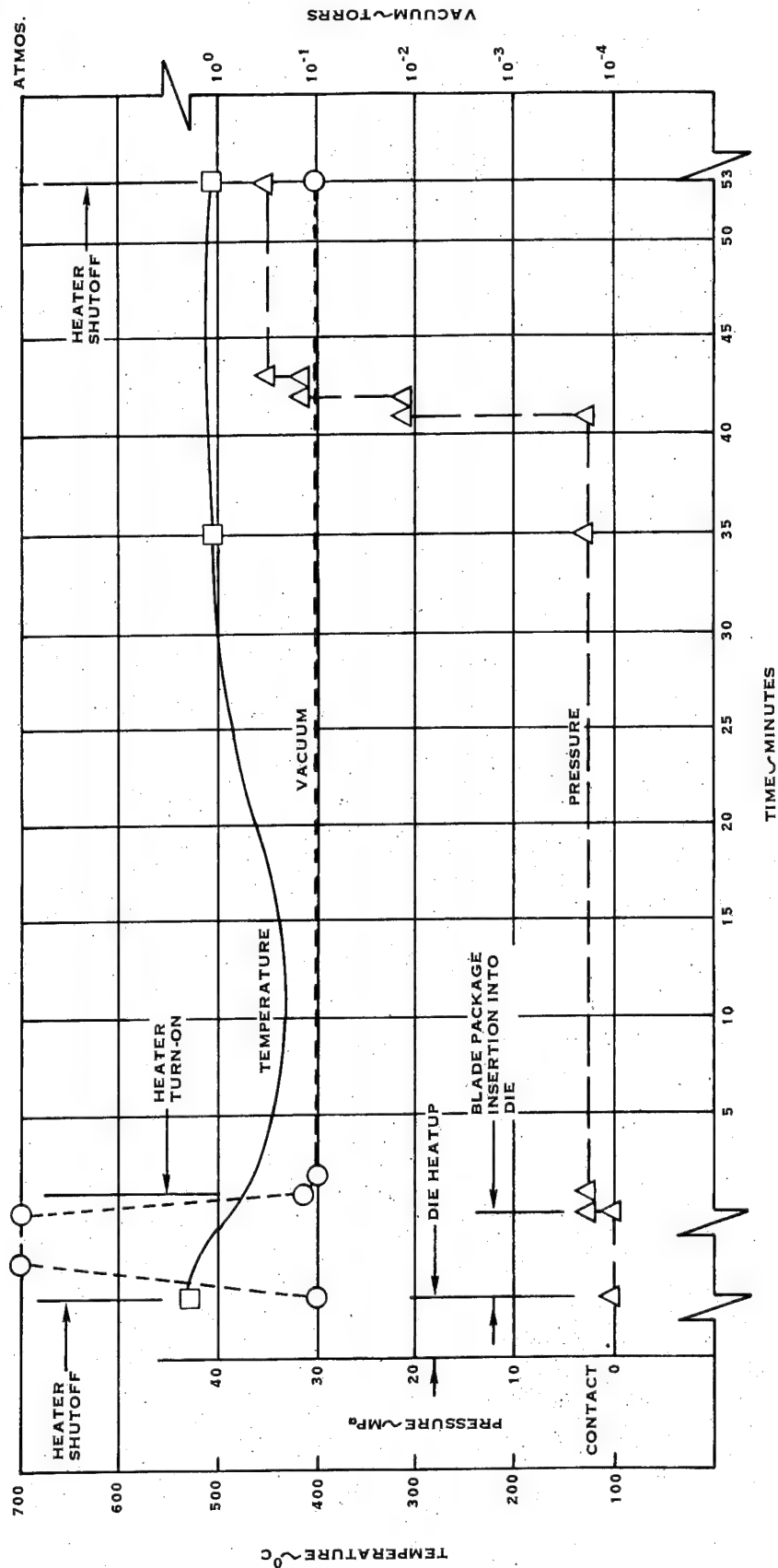PRIOR TO METAL BOND FORMATION

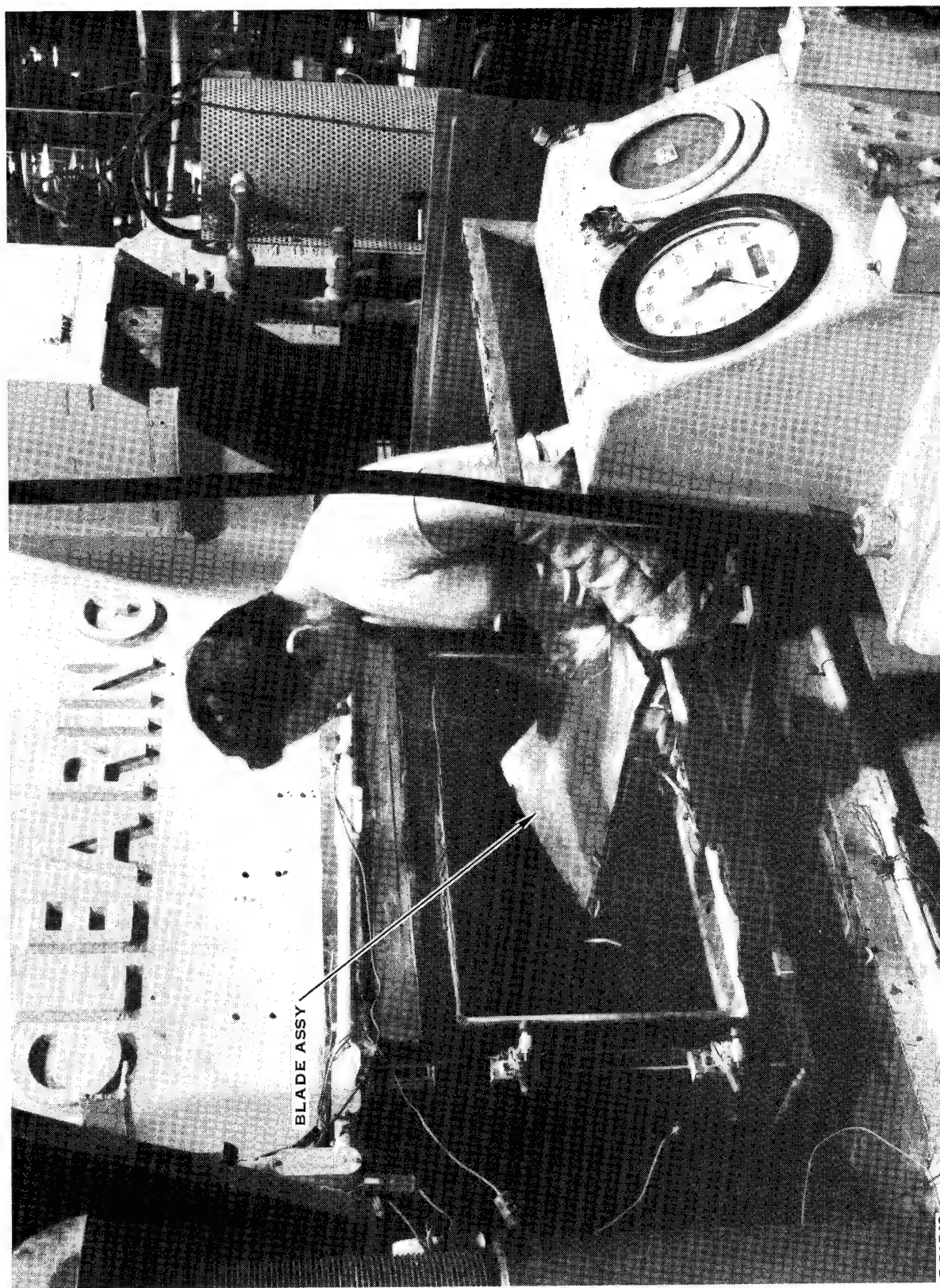FIGURE 45. DIFFUSION BOND CYCLE FOR SHELL TO SPAR & HONEYCOMB JOINT FORMATION
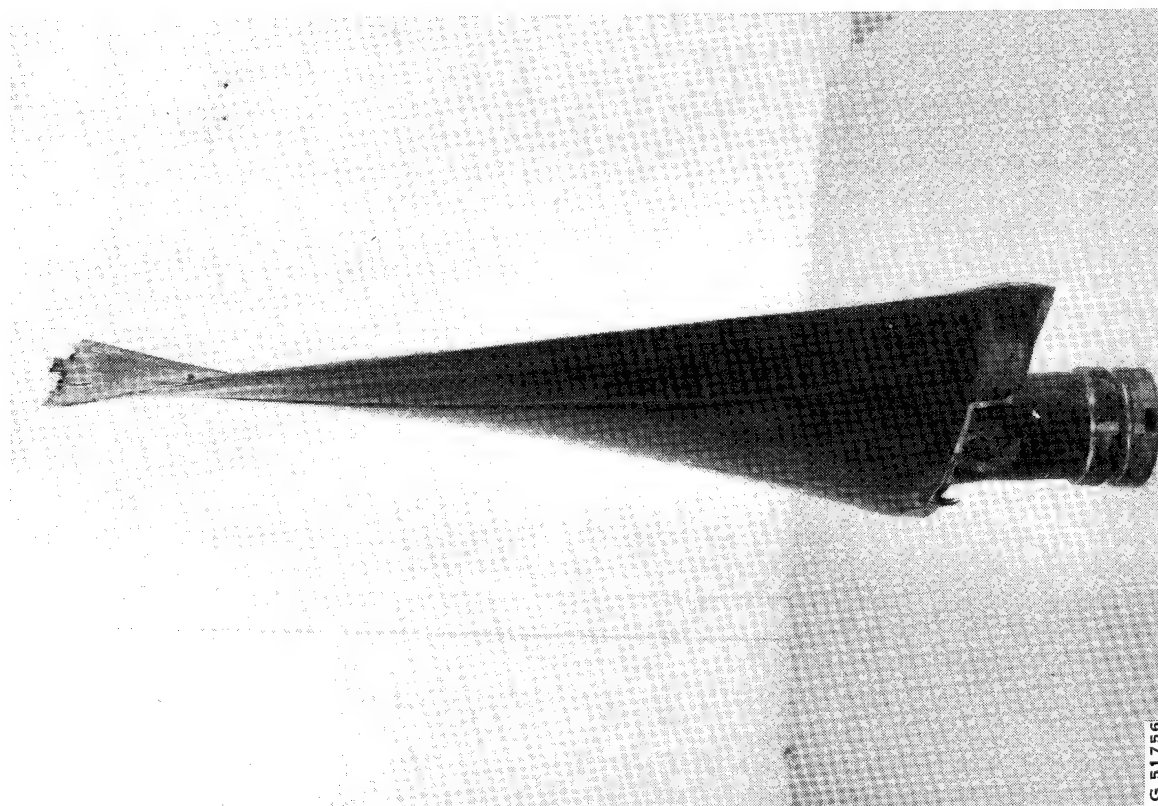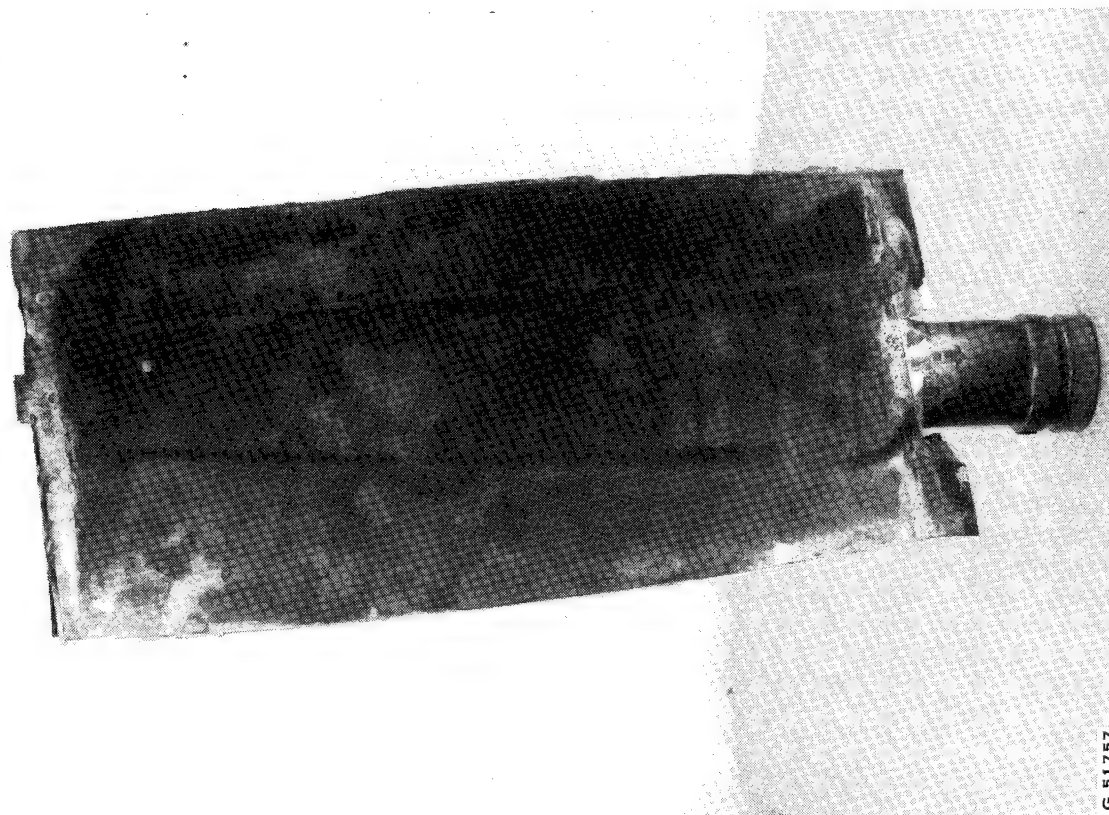
96

FIGURE 46. INSTALLATION OF DEMONSTRATION AIRFOIL PRESSINGS INTO BONDING DIES FOR METAL JOINT FORMATION

97

CAMBER SIDE VIEW

G 51757

LE VIEW

G 51756

FIGURE 47. POST BOND JOINT FORMATION OF DEMONSTRATION AIRFOIL PRESSINGS

98

G 51747

FIGURE 49. RADIAL SLOTS CUT IN PRESSURE DISTRIBUTION PAD ASSEMBLY IN AN ATTEMPT TO ELIMINATE HONEYCOMB CRUSH

FLOW OF PRESSURE DISTRIBUTION PAD

G 51746
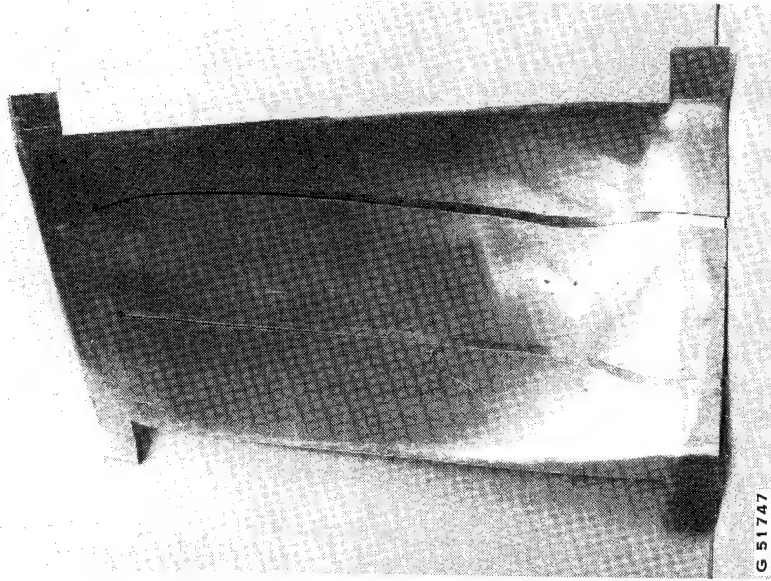
FIGURE 48. ALUMINUM PRESSURE DISTRIBUTION PAD SHOWING METAL FLOW UNDER BOND JOINT FORMATION

99

3.2.5.3 Final Product Inspection

Final product inspection consisted of a visual inspection of the two pressings along with tap testing of the shell to spar and the sheath to shell bond joints. The visual inspection found no delamination indications. The exterior surface was locally deformed outboard of the spar as previously discussed. Also evident visually and dimensionally were steps formed in the shell at the ply dropoff regions in plane with the spar. These exterior impressions, which were not evident at shell consolidation, were imparted in the outer skin with the joining of the shells to the spar. It was later judged that local aluminum enrichment would substantially eliminate the problem.

A tap test was conducted on both simulated airfoil pressings with the regions of suspected incomplete bonding highlighted in grease pencil. Both sides of both airfoil pressings are shown in Figure 50 for the AA6061 and AA1100 matrix shell blades respectively. As shown in Figure 50, the sheath to shell joint appeared to be sound. No NDI methods for determination of bond joint quality were employed owing to schedule and financial restraints.

One further test performed on the AA6061 matrix airfoil pressing was a bench resonant frequency measurement and a comparison of same with the frequency range of QCSEE adhesively bonded pressings. As noted earlier beside the bond joint change to AA6061 aluminum alloy, changes in the number and thickness of composite plies, the leading edge material from Inconel 625 to 6Al-4V titanium and the honeycomb material from aluminum to titanium all would have some effect on resonant frequency. Therefore, the data is offered without comment as to its accuracy in the determination of airfoil structural soundness.

	QCSEE Adhesively Bonded Airfoil Pressings	QCSEE Metal Bonded Airfoil Pressings
1st Bending	106.6 Hz	107.7 Hz
2nd Bending	217.9	199.1
1st Torsion	392.2	396.9

100

FIGURE 50. TAP TEST INSPECTION INDICATIONS OF SUSPECT METAL BOND JOINTS OF TWO DEMONSTRATION AIRFOIL PRESSINGS

3.2.6 Process Development Summary

The goal of the process development task to develop key processing parameters leading to two simulated airfoil pressings was accomplished. The principal finding of the material testing was the selection of AA6061 over AA1100 alloy system as the bond joint material for both candidate composite shell matrix materials. Other material process work identified limitations in the titanium honeycomb compressive strength, determined bond strength in a peel failure mode of honeycomb and verified the typical strength/stiffness properties of 0.2 mm boron/aluminum materials. The extensive development work on air and quik-vac (vacuum) bonding processes with boron/aluminum materials, performed under Air Force Contract AFML-TR-77-13, provided the remaining new technology needed.

The subsequent two airfoil pressings were made utilizing existing QCSEE FOD blade tooling. Limitations in that tooling led to unavoidable permanent depressions formed in the blade shell exterior outboard of the spar surface. Future blade manufacture will recognize the necessity to maintain a continuous rigid die surface when metal joining airfoil pressings featuring large hollow interior sectors. The quality assurance examination of the subject pressings identified several areas of suspected poor bond joint formation between shells and spar. The critical joint between the sheath and the shells appeared to be sound.

4.0 CONCLUSIONS

Design studies on a 3.0 aspect ratio spar and shell construction fan blade indicated a potential weight savings for a first stage fan rotor of 39% when a hollow titanium spar is employed. This savings from the bill of material solid titanium blade would translate into improvements in large transport aircraft payload and range. An alternate design which featured substantial blade internal volume filled with titanium honeycomb inserts achieved a 14% potential weight savings over the B/M rotor system. This second configuration requires a smaller development effort and entails less risk to translate a design into a successful product.

The feasibility of metal joining large subsonic spar and shell fan blades was demonstrated. Although much process evaluation and product testing remains a technical approach of providing the higher temperature and strength capability of metal joining is at hand. Initial aluminum alloy screening performed within the context of this program and also evaluated in other composite programs indicate a distinct preference for AA6061 aluminum alloy for use as a joint material. The simulated airfoil pressings established the necessity of rigid die surfaces when joining materials of different compressive rigidities.

The two aluminum alloy matrix choices both were successfully formed into blade shells. Testing was not performed within this program which would lead to a choice of alloy system.

5.0 <u>RECOMMENDATIONS</u>

- With the hollow titanium spar design concept offering the greatest rotor stage weight savings, it is recommended that a program be established to define the material properties required and to demonstrate feasibility of plastic forming hollow titanium spars.

- With the apparent structural advantages of metal joining, it is recommended that a program be established using tooling specifically designed for metal bonding to produce and test an advanced airfoil shape with this joining method. The recommended program would address process parameters, NDI methods and structural durability of a product so as to firmly establish the design concept as an alternate design for future aircraft applications.

6.0 REFERENCES

1. NASA CR-135001, "Fiber Composite Fan Blade Impact Improvement," February 1976, Hamilton Standard Division of United Technologies Corporation, Contract NAS3-17837.

2. AFML-TR-77-13, "Development of Air Bonded FOD Resistant Metal Matrix Fan Blades," March 1977, Hamilton Standard Division of United Technologies Corporation, Contract F33615-75-C-5285.

3. NASA CR-135184, "Boron/Aluminum Fan Blades for SCAR Engines," June 1977, General Electric Company, Contract NAS3-18910.